



저작자표시-비영리-변경금지 2.0 대한민국

이용자는 아래의 조건을 따르는 경우에 한하여 자유롭게

- 이 저작물을 복제, 배포, 전송, 전시, 공연 및 방송할 수 있습니다.

다음과 같은 조건을 따라야 합니다:



저작자표시. 귀하는 원저작자를 표시하여야 합니다.



비영리. 귀하는 이 저작물을 영리 목적으로 이용할 수 없습니다.



변경금지. 귀하는 이 저작물을 개작, 변형 또는 가공할 수 없습니다.

- 귀하는, 이 저작물의 재이용이나 배포의 경우, 이 저작물에 적용된 이용허락조건을 명확하게 나타내어야 합니다.
- 저작권자로부터 별도의 허가를 받으면 이러한 조건들은 적용되지 않습니다.

저작권법에 따른 이용자의 권리는 위의 내용에 의하여 영향을 받지 않습니다.

이것은 [이용허락규약\(Legal Code\)](#)을 이해하기 쉽게 요약한 것입니다.

[Disclaimer](#)

공학박사학위논문

기포 유도 난류응력 모델 개발 및 원형
실린더 주위를 흐르는 균일한
기포스웜에서 실험적 검증

**Modeling and experimental validation of the bubble-
induced Reynolds stress in the homogeneous
bubble-swarm past a circular cylinder**

2021년 8월

서울대학교 대학원
기계항공공학부
이 주 범

기포 유도 난류응력 모델 개발 및 원형
실린더 주위를 흐르는 균일한
기포스웜에서 실험적 검증

**Modeling and experimental validation of the bubble-
induced Reynolds stress in the homogeneous
bubble-swarm past a circular cylinder**

지도교수 박형민

이 논문을 공학박사 학위논문으로 제출함

2021년 4월

서울대학교 대학원
기계항공공학부
이주범

이주범의 공학박사 학위논문을 인준함

2021년 6월

위원장: 송성진
부위원장: 박형민
위원: 김호영
위원: 황원태
위원: 유동현

Modeling and experimental validation of the bubble-induced Reynolds stress in the homogeneous bubble-swarm past a circular cylinder

Jubeom Lee

Department of Mechanical and Aerospace Engineering
Seoul National University

Abstract

In response to the community's desire to develop a full bubble-induced turbulence (BIT) model, new explicit algebraic models have been developed in the framework of the two-phase mixing-length theory in an unbounded homogeneous bubble-swarm past a circular cylinder in quiescent liquid and bounded laminar and turbulent bubbly flows for wide ranges of volume void fractions ($\mathcal{O}(10^{-2}-10^{-1})$) and bulk liquid Reynolds number ($Re_D < \mathcal{O}(10^5)$). The proposed models could be expressed as a function of the mean liquid flow removing any references to the fluctuating part of the liquid velocity to overcome another closure problem encountered in the gas-liquid flow in the Euler-Euler Reynolds-averaged Navier-Stokes equation. Here, we attempt to additionally consider turbulence modification (e.g., enhancement or suppression) of the bubble-induced turbulence when it is surrounded by external turbulence *via* a realistic bubbly mixing-length under the relevant environment, and a scaling law for the mean liquid velocity as a function of gas-phase statistics is proposed, all of which have been discussed and validated independently. When the developed submodels are used together, it yields an explicit algebraic model for the bubble-induced streamwise liquid fluctuation (which is equivalent to the square-root of the streamwise normal stress) and turbulent stress, respectively. The detailed procedures to derive the proposed models and the theoretical reasoning for them are also provided, trends of which are consistent with the previous observations (e.g., PDFs of the liquid fluctuations and linear evolution of turbulence level with the volume void fraction). To

independently check the performance of the present models, we have configured a homogeneous bubble-swarm and let it flow over a circular cylinder at downstream to artificially induce turbulence modulation in the bubble-induced turbulence while varying the volume void fraction in a small-to-moderate range and cylinder diameter (D). The Reynolds number of rising bubbles is approximately 10^3 . We focused on how the preferred concentration of bubbles past a cylinder is established and how its wake is induced by using a high-speed two-phase particle image velocimetry technique. Depending on the local void distribution in the wake behind the cylinder, two typical bubbles' distributions are classified, which leads to two different regimes with dissimilar behaviors in gas-phase statistics. Furthermore, we have estimated the relevant hydrodynamics forces acting on phases' boundaries to identify these differences. Along with the local void distribution, the bubble-induced liquid flow forms an interesting wake structure behind the cylinder. For example, a wake-defect-like streamwise velocity profile and skew-symmetric turbulent stress are induced; however, the distortion by the circular cylinder is restored quite fast (within $5D$ along the streamwise direction). Increasing the cylinder size, however, delays the recovery of upstream flow statistics and reduces the turbulence level in the wake. Based on the observed physics, the proposed models, which is an extension of the classical eddy-diffusivity hypothesis, but additionally considers the effects by bubble-induced flow and multiple bubbles, are in a reasonably good agreement with the experimental data measured at downstream of the circular cylinder. Especially, the absolute magnitudes and the spatial variations of the bubble-induced turbulence are reasonably predicted at both inside and outside of the cylinder, and we have also discussed the evolutions of each prefactor along downstream, and reasoning for them is also provided. We have expanded the validation tests to bubbly internal flows (e.g., wall-bounded upward laminar and turbulent bubbly flows) by gathering all the available pieces of prior experimental data in the literature. We have confirmed that the absolute magnitudes and the tendencies of the bubble-induced turbulence when it is surrounded by incidence turbulence are reasonably predicted at both the core- and near wall-region of pipes (channels) by the proposed models, and we have also discussed some abnormal discrepancies and their origination. We try not to hide

our limitations in potential applicability, but rather objectively evaluate the strengths and weaknesses. Lastly, a short guideline for a large-scale Reynolds-averaged Navier-Stokes simulation in a two-fluid Euler-Euler framework is suggested and our next plan for constructing a full-set explicit Reynolds stress tensor is introduced.

Keyword : bubbly flow, circular cylinder, closure problem, bubble-induced turbulence, turbulence modeling, experimental validation

Student Number : 2014-22500

To my family for their love and support

Table of Contents

Abstract	i
Contents	v
List of Tables	vii
List of Figures	viii
Nomenclature	xvi
Chapter	
1. Introduction	
1.1 Closure problem in two-phase flow ·····	1
1.2 Past approaches ·····	2
1.2.1 Two-phase eddy-viscosity hypothesis ·····	2
1.2.2 A transport equation for Reynolds stresses ·····	5
1.2.3 An alternative way ·····	7
1.3 Main purposes ·····	10
2. An explicit algebraic model for the bubble-induced turbulence	
2.1 Derivation of the two-phase mixing-length ·····	12
2.1.1 A gravity-driven bubble-swarm ·····	12
2.1.2 Bubbly internal flows ·····	15
2.2 A scaling law for the mean liquid velocity ·····	19
2.2.1 An unbounded quiescent liquid ·····	19
2.2.2 A wall-bounded dynamic liquid ·····	21
2.3 Derivation of the explicit algebraic Reynolds stress models ·····	24
2.3.1 A gravity-driven bubbly external flow ·····	24
2.3.2 Laminar and turbulent bubbly internal flows ·····	33

3. Experimental validation: a homogeneous bubble-swarm past a circular cylinder	
3.1 Experimental setup and procedures	45
3.1.1 Flow facilities and robustness	45
3.1.2 Two-phase particle-image velocimetry (PIV)	46
3.1.3 Phase discrimination	48
3.1.4 Uncertainties in the measurements	51
3.1.5 Characterization of the considered gas-phase	52
3.2 Gas-phase statistics in the cylinder wake	54
3.3 Bubble-induced liquid flow around a circular cylinder	61
3.3.1 Characterization of the upstream flow	61
3.3.2 Bubble-induce flow in the cylinder wake	63
3.3.3 BIT in the cylinder wake	69
3.4 Interfacial momentum transfer at the phases' interfaces	73
3.5 Validations and discussions	77
4. Application of the developed model to laminar and turbulent bubbly pipe (channel) flows	
4.1 Turbulent nature of the BIT	122
4.2 A short comment on the nonlinear interaction by external turbulence	124
4.3 Prefactors optimization	125
4.4 Validations and discussions	128
5. Suggestion to the two-fluid Euler-Euler RANS simulation and following works	136
6. Concluding remarks	138
Bibliography	141
Abstract in Korean	148

List of Tables

- Table 2.1 Inlet conditions for the considered upward laminar and turbulent bubbly pipe flows. Here, we have exclusively selected experimental studies that provide time-averaged spatially-varying turbulence statistics. The superscript “*” denotes the estimated volume void fractions by integrating the local void fraction across the entire cross-section. 39
- Table 3.1 Characteristics of the considered gas-phase. Here, the “ ∞ ” denotes a variable measured at the upstream location. 82

List of Figures

- Figure 2.1 Schematic diagram of side-by-side cylindrical bubbles in an inviscid flow. The distance between the centroids of the bubbles is l_m , and two points P_1 and P_2 are located on the same streamline ($\psi = \psi_1$); \bar{v}_b is the rise velocity of bubbles in a quiescent liquid, and η is the distance from the control plane; Liquid drift-length ($y_2 - y_1$) is proportional to the two-phase mixing-length. 40
- Figure 2.2 Schematic diagram of laminar and turbulent bubbly flows near the wall: evenly distributed side-by-side cylindrical bubbles rise with \bar{v}_r in an inviscid linear-shear flow. The parameters are the same as specified in figure 2.1. 41
- Figure 2.3 Signatures of the time-averaged two-phase mixing-length (flood) and mean void fraction (line): (a) a homogeneous bubble-swarm past a circular cylinder (D of 20 mm) in quiescent water at $\langle \bar{\alpha} \rangle$ of 0.6%; (b) 1.1%; (c) upward turbulent bubbly pipe flows (Reynolds number (Re_D , where D of 40 mm) is 5300) at $\langle \bar{\alpha} \rangle$ of 1.8%; (d) Re_D is 44000 at $\langle \bar{\alpha} \rangle$ of 1.5%. Here, the denser the line-contour, the more severe the change in $\bar{\alpha}$ 42
- Figure 2.4 Linear relation between the local statistics with global values of (a) void fraction; (b) bubble size; (c) bubble rise velocity; (d) a scaling relation between the streamwise mean liquid velocity and gas-phase statistics; \circ , measured at upstream; ∇ , in the cylinder wake ($|x/D| \leq 0.5$, $y/D = 1$, where D of 20 mm); \square , outside of the wake ($|x/D| > 0.5$). For the purpose of visual comparison, a dashed-line in each figure is drawn to cross the origin. 43
- Figure 2.5 (a) Linear relation between the local statistics with global values of void fraction in bounded bubbly flows; (b) a scaling relation between the mean liquid velocity and gas-phase statistics in the presence of the background liquid flow. The symbol is the same as specified in table 2.1. For the purpose of visual comparison, a solid line in each figure is drawn to cross the origin. 44
- Figure 3.1 Schematic diagram for an experimental setup to generate bubbly flows over a circular cylinder in a stagnant water tank. 83

- Figure 3.2 Experimental setup for the two-phase high-speed particle image velocimetry measurement. 84
- Figure 3.3 Image processing sequence to discriminate gas (h) and liquid (k) phases from a raw image (a) obtained by two-phase particle image velocimetry. 85
- Figure 3.4 Comparison of liquid velocity fields per each post-processing step: (a) a representative raw image measured at upstream for the volume void fraction of 0.006; (b) LoG-filtered image; (c) final image by subtracting median filtered image from the LoG image; (d) calculated liquid velocity field through the PIV with the raw image as an input; (e) with LoG image; (f) with the final image (after weighted spatial linear interpolation); Here the grey-colored bubbles are located on and in front of the half-width of the test-section while orange-colored bubbles are behind the measurement plane. 86
- Figure 3.5 An example of the weighted spatial linear interpolation at a point at the bubble interface (red-box): neighboring vectors that have the same x - and y -coordinate outside the bubble are adopted for the interpolation together in the Gaussian weight kernels. Here the grey-colored bubbles are located on and in front of the half-width of the test section while orange-colored bubbles are behind the measurement plane. 87
- Figure 3.6 Upstream ($y/D = -1.5$) condition of gas phase: (a, b) probability density function (PDF) of equivalent diameter (d_b) and rise velocity ($v_{b\infty}$) of bubbles; (c, d) transverse distribution of local void fraction ($\bar{\alpha}$) and mean bubble rise velocity (\bar{v}_b). ■, $\langle \bar{\alpha} \rangle = 0.003$; ○, 0.006; △, 0.009; ▽, 0.0095; ◇, 0.011; □, 0.02; ●, 0.021. In (a) and (b), solid lines denote the Gaussian curve for $\langle \bar{\alpha} \rangle = 0.003$ and 0.021, shown for a comparison. 88
- Figure 3.7 Typical local void ($\bar{\alpha}$) distributions in the wake ($y/D = 1.5$) behind a circular cylinder normalized by the upstream volume void fraction ($\langle \bar{\alpha} \rangle$): □, in-focused bubbles at $z/D = 0$ plane; △, $z/D = -3$; ◇, $z/D = +3$; ○, all bubbles. Maximum deviation is about 14% at $x/D = -0.75$ 89
- Figure 3.8 Contours of time-averaged in-focus bubble distributions in the cylinder wake (whose diameter is 20 mm, centered at the origin)

normalized by the upstream mean void fraction, i.e., $\langle \bar{\alpha} \rangle$;
 Normalized void fraction is highlighted when $\bar{\alpha}/\langle \bar{\alpha} \rangle = 1$ (thick
 solid-line). 90

Figure 3.9 Contours of time-averaged in-focus bubble distributions in the
 cylinder wake (whose diameter is 30 mm, centered at the origin)
 normalized by the upstream mean void fraction, i.e., $\langle \bar{\alpha} \rangle$;
 Normalized void fraction is highlighted when $\bar{\alpha}/\langle \bar{\alpha} \rangle = 1$ (thick
 solid-line). 91

Figure 3.10 Streamwise distributions of the normalized local void fraction
 measured at the symmetry axis ($x/D = 0$); a solid-line,
 Sugiyama et al (2001); \circ , Joo & Dhir (1994); ∇ , present
 experiment. 92

Figure 3.11 Transverse distribution of local void fraction ($\bar{\alpha}/\langle \bar{\alpha} \rangle$) at (a,d)
 $y/D = 0.65$; (b,e) 1.5; (c,f) 2.5 behind the cylinder of $D = 20$ mm
 $(a-c)$ and 30 mm $(d-f)$: \square , $\langle \bar{\alpha} \rangle = 0.003$; \triangle , 0.009; \diamond , 0.011;
 \circ , 0.021. 93

Figure 3.12 Transverse distribution of equivalent bubble diameter ($\bar{d}_b/\langle \bar{d}_b \rangle$)
 at (a,d) $y/D = 0.65$; (b,e) 1.5; (c,f) 2.5 behind the cylinder of D
 $= 20$ mm $(a-c)$ and 30 mm $(d-f)$: \square , $\langle \bar{\alpha} \rangle = 0.003$; \triangle , 0.009;
 \diamond , 0.011; \circ , 0.021. 94

Figure 3.13 Transverse distribution of bubble aspect ratio ($\bar{\beta} = \bar{d}_h/\bar{d}_v$) at
 (a,d) $y/D = 0.65$; (b,e) 1.5; (c,f) 2.5 behind the cylinder of $D =$
 20 mm $(a-c)$ and 30 mm $(d-f)$: \square , $\langle \bar{\alpha} \rangle = 0.003$; \triangle , 0.009; \diamond ,
 0.011 ; \circ , 0.021. 95

Figure 3.14 Transverse distribution of streamwise mean bubble rise velocity
 $(\bar{v}_b/\langle \bar{v}_b \rangle)$ at (a,d) $y/D = 0.65$; (b,e) 1.5; (c,f) 2.5 behind the
 cylinder of $D = 20$ mm $(a-c)$ and 30 mm $(d-f)$: \square , $\langle \bar{\alpha} \rangle = 0.003$;
 \triangle , 0.009; \diamond , 0.011; \circ , 0.021. 96

Figure 3.15 Transverse distribution of transverse mean bubble rise velocity
 $(\bar{u}_b/\langle \bar{u}_b \rangle)$ at (a,d) $y/D = 0.65$; (b,e) 1.5; (c,f) 2.5 behind the
 cylinder of $D = 20$ mm $(a-c)$ and 30 mm $(d-f)$: \square , $\langle \bar{\alpha} \rangle = 0.003$;

\triangle , 0.009; \diamond , 0.011; \circ , 0.021. 97

Figure 3.16 (a) Scaling relation between mean bubble rise velocity and $\langle \bar{\alpha} \rangle$: \circ , measured at upstream; \triangle , outside of the nearwake ($|xD| > 0.5$) for $D = 20$ mm; \square , $D = 30$ mm. (b) Variations of spatially-averaged (absolute) bubble rise velocity with $\langle \bar{\alpha} \rangle$. \times , present study; ∇ , Zenit et al. (2001); \circ , Risso & Ellingsen (2002); \triangle , Martínez-Mercado et al. (2007); Δ , Riboux et al. (2010); \blacktriangledown , Colombet et al. (2011); \bullet , Colombet et al. (2015) 98

Figure 3.17 (a) Contours of time-averaged in-focus bubble distributions in the hydrophilic cylinder wake (whose diameter is 30 mm, and contact angle is 60°); (b) hydrophobic cylinder wake (30 mm, 140°); (c) time sequence (dt of 1 ms) of instantaneous images showing a bubble trapping into the grooves of the hydrophobic cylinder. In each contour, we highlighted angles at which the maximum mean void fraction is developed. 99

Figure 3.18 (a,b) Gas-phase statistics along the cylinder circumferential direction (D of 30 mm); (c,d) in the cylinder wake ($y/D = 1$); (a,c) mean bubble size; (b,d) mean void fraction: \circ , hydrophilic cylinder; \bullet , hydrophobic cylinder. Here 0° coincides with the front stagnation point. 100

Figure 3.19 (a,b) Instantaneous and (c,d) time-averaged liquid velocity fields behind a homogeneous bubble-swarm at upstream ($\langle \bar{\alpha} \rangle = 0.011$) measured at (a,c) the core region ($|xD| < 2.0$); (b,d) near the sidewall ($13 < |xD| < 17$). It is worth noting that the calculated velocity fields are the direct results of the PIV estimation without any post-processing algorithm to suppress the erroneous vectors. 101

Figure 3.20 Upstream ($y/D = -1.5$) bubble-induced liquid flow: (a) mean streamwise velocity (\bar{v}_l); (b) mean transverse velocity (\bar{u}_l); (c) root-mean-square of streamwise velocity fluctuation ($v''_{l,rms}$); \circ , $\langle \bar{\alpha} \rangle = 0.006$; \bullet , 0.011. 102

Figure 3.21 Probability density functions (PDFs) of liquid-phase velocity in (a) streamwise and (b) transverse components, measured at the

- upstream of the circular cylinder. 103
- Figure 3.22 Instantaneous two-phase flow fields with velocity vectors and contour of normalized spanwise vorticities ($\omega_z^* = \omega_z D / \langle \bar{v}_{\infty} \rangle$) at upstream: (a) $\langle \bar{\alpha} \rangle = 0.006$; (b) 0.011. Bubbles that are located on and in front of the $z/D = 0$ plane are shown. 104
- Figure 3.23 Instantaneous two-phase flow around a circular cylinder ($D = 20$ mm): (a) $\langle \bar{\alpha} \rangle = 0.006$; (b) 0.011. Bubbles that are located on and in front of the $z/D = 0$ plane are shown. 105
- Figure 3.24 Instantaneous two-phase flow around a circular cylinder ($D = 30$ mm): (a) $\langle \bar{\alpha} \rangle = 0.006$; (b) 0.011. Bubbles that are located on and in front of the $z/D = 0$ plane are shown. 106
- Figure 3.25 Temporal evolution ($\Delta t = 1$ ms) of the instantaneous separating liquid shear-layer in two-phase flows. 107
- Figure 3.26 Contours of normalized local void fraction, $\bar{\alpha} / \langle \bar{\alpha} \rangle$ (flood) and normalized spanwise vorticity, $\bar{\omega}_z^*$ (line) in the wake behind the cylinder of (a,b) $D = 20$ mm and (c,d) 30 mm: (a,c) $\langle \bar{\alpha} \rangle = 0.006$; (b,d), 0.011. Here, the line contour levels are set in the increments of 0.1, and dashed lines denote negative value. 108
- Figure 3.27 Transverse distributions of the mean streamwise velocity (\bar{v}_l) in liquid phase in the wake behind a cylinder: (a) $D = 20$ mm; (b) 30 mm; (open-symbol) $\langle \bar{\alpha} \rangle = 0.006$, (closed) 0.011; \bigcirc , $y/D = 0.65$; \triangle , 1.0; ∇ , 1.5; \square , 2.0; \diamond , 2.5; \star , 3.0. 109
- Figure 3.28 Transverse distributions of the mean transverse velocity (\bar{u}_l) in liquid phase in the wake behind a cylinder: (a) $D = 20$ mm; (b) 30 mm; (open-symbol) $\langle \bar{\alpha} \rangle = 0.006$, (closed) 0.011; \bigcirc , $y/D = 0.65$; \triangle , 1.0; ∇ , 1.5; \square , 2.0; \diamond , 2.5; \star , 3.0. 110
- Figure 3.29 Streamwise variations of the normalized bubble-induced mean liquid velocity (\bullet) and a local void fraction (\square) in the wake behind the cylinder ($Re_D = 2,400$ where D of 20 mm) with $\langle \bar{\alpha} \rangle = 0.006$. A solid-line denotes the mean liquid velocity in the single-phase flow ($Re_D = 3,900$) (Parnaudeau et al. 2008), here

L_r denotes the recirculation bubble size. 111

Figure 3.30 Probability density functions (PDFs) of the liquid-phase velocity in (a,c) streamwise and (b,d) transverse directions, (a,b) measured in the wake behind the circular cylinder ($|xD| \leq 0.5$ and $0.5 \leq y/D \leq 3.0$) and (c,d) outside of the wake ($|xD| > 0.5$). 112

Figure 3.31 Scaling relation between bubble-induced liquid velocity fluctuation and $\langle \bar{\alpha} \rangle$: (a) streamwise velocity fluctuation; (b) transverse velocity fluctuation: \circ , fluctuation measured at upstream; \triangle , outside of the nearwake ($|xD| > 0.5$) behind the cylinder with D of 20 mm; \square , 30 mm. 113

Figure 3.32 Transverse distributions of the root-mean-square of streamwise velocity fluctuation ($v''_{i,rms}$) in liquid phase in the wake behind a cylinder: (a) $D = 20$ mm; (b) 30 mm; (open-symbol) $\langle \bar{\alpha} \rangle = 0.006$, (closed) 0.011; \circ , $y/D = 0.65$; \triangle , 1.0; ∇ , 1.5; \square , 2.0; \diamond , 2.5; \star , 3.0. 114

Figure 3.33 Transverse distributions of the root-mean-square of transverse velocity fluctuation ($u''_{i,rms}$) in liquid phase in the wake behind a cylinder: (a) $D = 20$ mm; (b) 30 mm; (open-symbol) $\langle \bar{\alpha} \rangle = 0.006$, (closed) 0.011; \circ , $y/D = 0.65$; \triangle , 1.0; ∇ , 1.5; \square , 2.0; \diamond , 2.5; \star , 3.0. 115

Figure 3.34 Transverse distributions of the turbulent stress ($-\overline{v''_i u''_i}$) in liquid phase in the wake behind a cylinder: (a) $D = 20$ mm; (b) 30 mm; (open-symbol) $\langle \bar{\alpha} \rangle = 0.006$, (closed) 0.011; \circ , $y/D = 0.65$; \triangle , 1.0; ∇ , 1.5; \square , 2.0; \diamond , 2.5; \star , 3.0. 116

Figure 3.35 Distributions of the lateral force acting on bubbles for $\langle \bar{\alpha} \rangle = 0.0095$ measured at upstream along $x/D = 0$ normalized by the maximum total force measured at downstream (-0.44D, 0.89D): \circ , drag; \diamond , lift; \triangle , turbulent dispersion force. 117

Figure 3.36 (a,c) Contour of the normalized transverse gradient of local void fraction ($\partial \bar{\alpha} / \partial x \cdot D / \langle \bar{\alpha} \rangle$). (b,d) Distributions of the ratio of lateral force to the summation of the magnitude of each force

(F') acting on bubbles for $\langle \bar{\alpha} \rangle = 0.0095$: (a,b) $D = 20$ mm; (c,d) 30 mm. \circ , drag; \bullet , lift; \triangle , turbulent dispersion force, \square , pressure-gradient and a dashed-line denotes a summation force. 118

Figure 3.37 Comparison between the modeled (\triangle) and measured (\circ) distribution of the streamwise velocity fluctuations in liquid phase behind the cylinders of (a,b) $D = 20$ mm and (c,d) 30 mm: (a,c) for $\langle \bar{\alpha} \rangle = 0.006$; (b,d) 0.011. Here we decomposed the contributions by the pure bubble-induced turbulence (\square) and by the redistributed bubbles by the cylinder (∇) in equation 2.24. 119

Figure 3.38 Comparison between the modeled (\triangle) and measured (\circ) distribution of the bubble-induced turbulent stress in liquid phase behind the cylinders of (a,b) $D = 20$ mm and (c,d) 30 mm: (a,c) for $\langle \bar{\alpha} \rangle = 0.006$; (b,d) 0.011. Here we decomposed the contributions by the inviscid flow (\square) and by the redistributed bubbles by the cylinder (∇) in equation 2.29. 120

Figure 3.39 (a,b) Evolution of resultant prefactors of the bubble-induced Reynolds stress model (c,d) those of the streamwise liquid fluctuation model along downstream. \circ , D of 20 mm for $\langle \bar{\alpha} \rangle = 0.006$; \triangle , 20 mm, 0.011; \bullet , 30 mm, 0.006; \blacktriangle , 30 mm, 0.011. 121

Figure 4.1 (a,b) Probability density functions (PDFs) of liquid velocity fluctuations in the wake behind a circular cylinder ($|x/d| \leq 0.5$, $0.5 \leq y/d \leq 3.0$) (Lee & Park 2020); (c,d) those in the core- ($|x/D| < 0.1$) and near wall-region ($0.38 < x/D < 0.4$) of turbulent bubbly pipe flows for $Re_D = 44,000$ (Lee et al. 2021), here a Gaussian-curve is drawn for comparison in streamwise direction: (a,c) streamwise-; (b,d) transverse-fluctuation in liquid-phase. 132

Figure 4.2 (a) Linear evolutions of tuning parameters in the predicted bubble-induced streamwise liquid fluctuation (v_l'') with increasing $\langle \bar{\alpha} \rangle$; (b) those in turbulent stress ($-\overline{v_l'' u_l''}$); \circ , c_{1n} ; ∇ , c_{2n} ; \square , c_{3n} ; \triangle , c_{1r} ; \diamond , c_{2r} 133

Figure 4.3 Comparison between the predicted (closed-) and measured (opened-symbol) bubble-induced streamwise liquid fluctuation.

We exclusively selected the maximum volume void fraction case for each bulk Reynolds number (Re_D), except the works by Shawkat et al. (2008). The symbol is the same as specified in table 2.1 and \blacktriangledown denotes the prediction result in which the prefactors are optimized by the least-square method as an example. 134

Figure 4.4 Comparison between the predicted (closed-) and measured (opened-symbol) bubble-induced turbulent (shear) stress. The description for each symbol is the same as in figure 4.3. Inset represents the data from Liu and Bankoff (1993) sharing the same axes titles and units. 135

Nomenclature

Roman symbols

B	Basset-history force [N/m ³]
C_{ij}	convection in Reynolds stress
c	mean shear-rate
$c(\cdot)$	tuning prefactor
D	diameter of a pipe (channel)
D_{ij}	diffusion in Reynolds stress
d	diameter of a circular cylinder
d_{max}	major-axis of a bubble
d_{min}	minor-axis of a bubble
Eo	Eötvös number, $Eo = g(\rho_l - \rho_g)d_b^2\sigma^{-1}$
F	hydrodynamic force per unit volume [N/m ³]
f	function
j	dummy variable
k	turbulent kinetic energy
L	integral length-scale, or length of a circular cylinder
l_b	bubbly mixing-length
l_m	mean distance between bubbles
l_r	recirculation-length
M	interfacial momentum transfer, or magnification error
Mo	Morton number, $Mo = g\mu_l^4(\rho_l - \rho_g)(\rho_l^2\sigma^3)^{-1}$
P	pressure-gradient induced force [N/m ³]
P_{ij}	production in Reynolds stress

Re	Reynolds number, $Re = \rho d_b v_b \mu_i^{-1}$
Ro	shape factor
S_k	source in the turbulent kinetic energy budget
$S_{R,ij}$	interfacial transport in Reynolds stress
S_ε	source in the dissipation rate budget
s	displacement
TD	turbulent dispersion force [N/m^3]
T	summation force
t	time
u	velocity in x -direction
V	volume of a bubble
V_0	terminal velocity of a bubble in quiescent liquid
VM	virtual-mass force [N/m^3]
v	velocity in y -direction
W	wall-lubrication force [N/m^3]
We	Weber number, $We = \rho d_b v_b^2 \sigma^{-1}$
w	velocity in z -direction
x	the Cartesian coordinate x , transverse-direction
y	the Cartesian coordinate y , parallel to streamwise-direction in chapter 3
y^+	dimensionless y -axis, $y^+ = \rho y u_t \mu_i^{-1}$
z	the Cartesian coordinate z , parallel to streamwise-direction in chapter 4

Greek Symbols

α local void fraction

β	bubble aspect-ratio, $\beta = d_{\max}/d_{\min}$
δ	total percentage error
δ_{ij}	Kronecker delta
ε	dissipation rate
η	dimensionless vertical distance from origin, $\eta = y/d_b$
κ	blockage-ratio, $\kappa = d_b/l_m$
μ	dynamic viscosity
ν	kinematic viscosity
ν_t	eddy- (turbulent-) viscosity
ρ	density
σ	surface tension
τ	Reynolds stress tensor
φ_{ij}	pressure-strain in Reynolds stress
ψ	stream function
ω	characteristics frequency, $\omega = \varepsilon/k$
ω_z	spanwise vorticity
∞	variable measured at upstream
∇	spatial-gradient

Superscripts

*	normalization
()'	fluctuation by an innate background liquid flow
()''	fluctuation by bubbles

$\bar{(\)}$ time-averaged quantity

$\vec{(\)}$ vector

Phi hydrophilicity

Pho hydrophobicity

Subscripts

D bulk

d cylinder diameter

g gas-phase

l liquid-phase

p particle

rms root-mean-square

$\langle \ \rangle$ spatial-averaged quantity

sep separation

Abbreviations

BIT bubble-induced turbulence

DoF depth of field

DPSS diode-pumped solid-state

EARSM explicit algebraic Reynolds stress model

EE Euler-Euler framework

FoV field of view

LIF Laser-induced fluorescence

LoG	Laplacian of Gaussian
PDF	probability density function
PIV	particle-image velocimetry
PTV	particle tracking velocimetry
TKE	turbulent kinetic energy
SIT	shear-induced turbulence
RANS	Reynolds-averaged Navier-Stokes equation

Chapter 1.

Introduction

1.1 Closure problem in two-phase flow

Implementing a large-scale laminar and turbulent bubbly flow simulation requires solving the Euler-Euler (EE) Reynolds-averaged Navier-Stokes (RANS) equation, which assumes that each phase is continuous. As the liquid velocity was decomposed into the average- and the perturbation-part in the conventional single-phase flow, i.e., $u_l = \bar{u}_l + u'_l$, the classical Reynolds decomposition can be extended to the gas-liquid two-phase flow to additionally consider perturbation by bubbles, and can be expressed as $u_l = \bar{u}_l + u'_l + u''_l$ (This idea was first conceived by Sato & Sekoguchi 1975). Here, the double-prime denotes the contribution by pure bubbles, which is independent of the background liquid flow. At this time, the most challenging thing to adopt this decomposition into the two-fluid EE-RANS approach is to solve the new closure problem encountered in the gas-liquid flow as:

$$\begin{aligned} \rho_g \alpha \frac{D}{Dt} \bar{u}_{gi} &= -\alpha \frac{\partial \bar{p}}{\partial x_i} + \alpha \frac{\partial}{\partial x_j} \left(\mu_g \frac{\partial \bar{u}_{gi}}{\partial x_j} - \rho_g \overline{u'_{gi} u'_{gj}} - \rho_g \overline{u''_{gi} u''_{gj}} \right) + (1-\alpha) M_{gi}, \\ \rho_l (1-\alpha) \frac{D}{Dt} \bar{u}_{li} &= -(1-\alpha) \frac{\partial \bar{p}}{\partial x_i} + (1-\alpha) \frac{\partial}{\partial x_j} \left(\mu_l \frac{\partial \bar{u}_{li}}{\partial x_j} - \rho_l \overline{u'_{li} u'_{lj}} - \rho_l \overline{u''_{li} u''_{lj}} \right) \\ &\quad + \alpha M_{li}, \end{aligned} \quad (1.1)$$

where j is a dummy variable, i.e., $j = 1, 2, 3$. Here, \bar{u} , ρ , and α are mean phase velocity, density, and local void fraction, respectively. p is the pressure shared by both phases, and M_i is interfacial transport per unit volume of the gas phase. The sub-scripts 'g' and 'l' denote the gas- and liquid-phase. Here, each fluctuation is innately independent of each other, therefore, the cross-correlation between them is considered to be negligible (e.g., $\overline{u'_j u''_j} = 0$) (Sato & Sekoguchi 1975; Troshko & Hassan 2001; Risso 2018; du Cluzeau et al. 2019; Lee & Park 2020; Ma et al. 2020). Therefore it is seen from the two-fluid momentum balance equation that the

additional unresolved bubble-induced stress tensor is generated in the both-phase, i.e., $\overline{u_1''u_1''}$, $\overline{u_2''u_2''}$, $\overline{u_3''u_3''}$, $\overline{u_1''u_2''}$, $\overline{u_1''u_3''}$, $\overline{u_2''u_3''}$, which should be modeled completely. However, Since the density ratio (ρ_g/ρ_l) is as small as $\mathcal{O}(10^{-3})$, the magnitude of turbulent stresses for the dispersed-phase can be neglected compared to those in the continuous-phase (Serizawa et al. 1975). For the gas-phase (equation 1.1), the contribution by the viscous shear stress can be also neglected. For these reasons, most of the previous studies are focused on developing models (or approaches) for the classical turbulent stresses in the single-phase and (or) additional stresses in the two-phase flow as a whole (separately) acting on the liquid-phase. Therefore, from now on, the subscript ‘*l*’ is omitted, but unless otherwise, all physical quantities are for the liquid-phase. The simplest but acceptable way (in many previous studies so far) to model M_i is to linearly superpose the possibly associated force terms (Hibiki & Ishii 2007, to name but a few). Furthermore, the relation of $M_g = -M_l$ is applied provided that surface tension effects are negligible (du Cluzeau et al. 2019).

1.2 Past approaches

1.2.1 Two-phase eddy-viscosity hypothesis

Regarding the unresolved bubble-induced Reynolds stress tensor, over the past three decades, there have been considerable efforts to predict the additional stresses due to bubbles, and this has traditionally been performed in three ways. The first approach is to improve the classical single-phase turbulent eddy-viscosity model (EVM) to capture additional turbulence by bubbles (Sato & Sekoguchi 1975; Troshko & Hassan 2001), to name but a few. The general expression of the two-phase eddy viscosity model based on the Boussinesq-hypothesis is:

$$-\overline{u_i''u_j''} = \nu_t'' \left(\frac{\partial \overline{u}_i}{\partial x_j} + \frac{\partial \overline{u}_j}{\partial x_i} \right) - \frac{2}{3} k \delta_{ij}, \quad (1.2)$$

where ν_t'' is modified turbulent viscosity, and Parenthesis is the mean rate of the strain tensor. To improve the two-phase eddy-viscosity ($\nu_t'' = l_b \times \nu$), both the

relevant length- (l_b) and velocity-scale (v) must be identified appropriately, and to achieve this, the classical mixing-length theory (equivalent to zero-equation model) which attempts to describe the momentum transfer by Reynolds stress by means of an eddy viscosity has been adopted. This necessitates the representative mean turnover length (l_b) of eddies in bubble-induced flows and the bubble-induced mean liquid-shear ($\partial \bar{u}_i / \partial x$), thus the representative velocity-scale is asymptotically scaled as $v \cong l_b \cdot |\partial \bar{u}_i / \partial x|$ (Sato & Sekoguchi 1975; Troshko & Hassan 2001). Therefore, this approach itself is physically intuitive and simple to use, but when it comes to complex turbulent bubbly flows (e.g., largely-separating flows with a high bulk Reynolds number (Re_D), or bubbly internal flows with a high volume void fraction ($\langle \bar{\alpha} \rangle$)), the predictive performance is known to be poor (Lee & Park 2020; Ma et al. 2020). Because it is only a rough estimation, the turbulent viscosity at the core-region of the channel is predicted to be zero ($\nu_t'' \cong l_b^2 \cdot |\partial \bar{u}_i / \partial x|$ is negligible due to $\partial \bar{u}_i / \partial x = 0$ at the pipe-center), which is not in actual physics. Moreover, this approach cannot account for turbulence attenuation by bubbles in the presence of the background liquid flow near the solid walls and is unable to apply at both uniform and non-uniform bubbly flows (e.g., bubbly external flows). Another method to estimate the relevant length- (l_b) and velocity-scale (v) in the eddy-viscosity model is the standard k - ε model (and this is one of the two-equation models). This model takes the influence of bubbles into account by including additional source terms (S_k and S_ε) in the turbulent kinetic energy (TKE, k) and dissipation rate (ε) budgets, or another equivalent parameter (e.g., frequency-scale of the smallest eddy as $\omega = \varepsilon/k$) (de Bertodano et al. 1994; Troshko & Hssan 2001; Ziegenhein et al. 2017; Liao et al. 2018). By calculating two more governing equations for k and ε per grid, the two-phase eddy-viscosity is modeled as $\nu_t'' = c_\mu k^2 / \varepsilon$, where $c_\mu = 0.09$ based on the similarity with the counterpart in the single-phase k - ε model (Troshko & Hssan 2001). In the previous studies, an appropriate source term in k and ε equations respectively was redesigned for each system, and representatively, bubble-induced modification to liquid turbulence was accounted for by the work of the drag per volume as

$S_k = c_k \overline{F}_D (\overline{v}_b - \overline{v}_l)$, while in the dissipation rate balance, the cascade of the bubble-induced turbulence into smaller scales is estimated by multiplying the production term (S_k) by a characteristic frequency (ω) which in fact is calculated from the TKE and the bubble diameter, based on the dimensional analysis as $S_\varepsilon = c_\varepsilon S_k k^{1/2} / d_b$ (Riboux et al. 2010; Risso 2018), here both c_k and c_ε are empirical coefficients to be optimized (Ma et al. 2017). This approach, however, is known to be more associated with the turbulence generated purely by the displacement in the liquid-phase due to bubbles (e.g., an inviscid flow and the averaged-wake) rather than by substantial wake instabilities detached from preceding bubbles (Risso 2016, 2018; Ma et al. 2020). In other words, the complicated nonlinear temporal interactions between wakes detached from bubbles' surfaces which are capable of reproducing the k^{-3} subrange alone for wavelengths larger than the mean bubble size does not take into account in this approach, rather it is conceptually determined by the fluid resistance, a type of friction in the close vicinity of bubbles, acting opposite to the relative motion of rising bubbles. Therefore, dominant contributions by an inviscid flow and the spatial fluctuations (which is equivalent to an averaged-wake) are mainly considered in the additional source terms in the balance equations in TKE and dissipation rate respectively, which lacks realism. Furthermore, nonlinear behaviors of the bubble-agitated turbulence surrounded by the external turbulence (e.g., grid-turbulence and shear-induced turbulence) are not reflected concretely in this approach, thus the reason, the two-phase k - ε model can only predict TKE and ε at the core-region of the channel (pipe) at relatively high bulk Reynolds number (Re_D , where D is channel diameter) and volume void fraction. Moreover, this method not only breaks the linear evolution of $c_\mu = v_t'' / (k^2 / \varepsilon)$ ($= 0.09$) away from the wall ($y^+ > 150$) depending on the gas-phase conditions, but also the behavior of c_μ is very different from case by case staying within 0.1-0.3 (< 0.09), showing substantial uncertainties (Ma et al. 2020). More specifically, for bubbly flows with small volume void fractions, the flow retains most of the features from the single-phase flow, implying that c_μ exhibits a similar value as in the single-phase equivalent. However, for higher volume void fractions with smaller bubbles, c_μ increases

towards the channel center, with $c_\mu = 0.03$ at $y^+ = 150$. Above all, prediction performance near the wall-region is questionable heretofore. Consequently, the aforementioned k - ε type model for gas-liquid flows with a linear eddy-viscosity lacks justification, and that adopting the single-phase value for c_μ ($= 0.09$) leads to deficient prediction. For this reason, a general consensus on which model exhibits a reasonable prediction performance for wide ranges of the bulk Reynolds number and volume void fraction has not been made. In summary, the two-phase two-equation model does not take into account the substantial detached wake interactions, which cannot be neglected for the higher volume void fractions, and turbulence enhancement (and suppression) by bubbles cannot be predicted simultaneously both at the core- and near wall-region of the pipe (channel). Although this model does not contain the unclosed prefactor, its single-phase value ($c_\mu = 0.09$) lacks justification and leads to deficient prediction away from the sidewalls for the higher bulk Reynolds number (Re_D , where D is the diameter of the pipe).

1.2.2 A transport equation for Reynolds stresses

In the views of these challenges, aside from the eddy-viscosity model, a second approach to developing Reynolds stress closures based on the EE-framework has been developed (Kataoka et al. 1992; Ma et al. 2020). They proposed differential transport equations for full-set Reynolds-stress components to close the RANS equations, arguing that the convection and diffusion of the Reynolds stress are locally balanced by the production, dissipation, interfacial Reynolds stress transfer, and pressure-strain, all of which have been expressed explicitly (Kataoka, et al. 1992) as:

$$\begin{aligned}
 & \underbrace{(1-\alpha)\frac{D\overline{u'_i u'_j}}{Dt}}_{C_{ij}: \text{convection}} - \underbrace{(1-\alpha)\left(\nu + c_s \nu_t\right)\frac{\partial\overline{u'_i u'_j}}{\partial x_k}}_{D_{ij}: \text{diffusion}} = \underbrace{-(1-\alpha)\left(\overline{u'_i u'_k}\frac{\partial\overline{u}_j}{\partial x_k} + \overline{u'_j u'_k}\frac{\partial\overline{u}_i}{\partial x_k}\right)}_{P_{ij}: \text{production}} \\
 & \underbrace{-(1-\alpha)\frac{2}{3}\delta_{ij}\varepsilon}_{\varepsilon_{ij}: \text{dissipation}} - \underbrace{c_1(1-\alpha)\varepsilon\left(\frac{\overline{u'_i u'_j}}{k} - \frac{2}{3}\delta_{ij}\right)}_{\phi_{ij}: \text{pressurestrain}} - c_2\left(P_{ij} - \frac{1}{3}\delta_{ij}P_{kk}\right) + \underbrace{S_{R,ij}}_{\text{interfacial}}
 \end{aligned} \tag{1.3}$$

here, ν is the liquid molecular kinematic viscosity, and $c_s = 1.63$, $c_l = 1.7$, and $c_2 = 0.6$ are empirical constants. It is worth mentioning that this equation predicts total Reynolds stresses ($\overline{u'u'} + \overline{u''u''}$) instead of separating an individual contribution in the single- ($\overline{u'u'}$) and two-phase flow ($\overline{u''u''}$) This second-moment closure for bubble-induced turbulence (BIT) in the Euler-Euler framework focuses on the core-region of the channel, where the interfacial term and dissipation term are locally in balance, and the classical anisotropy in bubbly flows is well reproduced by the governing equation especially at the core and the resultant stresses (mainly diagonal components) have been validated with the DNS data from sufficiently large-scale configurations (Lu & Tryggvason 2013; Santarelli & Fröhlich 2016). Although most studies lack thorough justification of the discussion on the pure bubble-induced turbulence (BIT), especially the work by Ma et al. (2020) has advantages of better representing bubble-induced anisotropy on the smaller scales in turbulent bubbly flows, e.g., anisotropic in liquid fluctuations, which can be found in previous experiments (Lance & Bataille 1991; Rensen et al. 2005; Roig & de Tournemine 2007; Riboux et al. 2010; Alméras et al. 2017; Risso 2018), as well as own experience (Lee & Park 2020; Lee et al. 2021). Moreover, this second-moment closure is proven to be robust capable of reproducing most of the physical phenomena observed experimentally. However, this method is computationally demanding compared to the zero- (mixing-length theory) and two-equation (k - ϵ) models, and off-diagonal components as a measure of turbulence anisotropy, i.e., shear stresses, which become influential in bubbly external flows (Lee & Park 2020) and turbulent bubbly flows in bent pipes (Kim & Park 2019), are neglected, which we judge is of great importance. Furthermore, the streamwise normal stress is more or less artificially designed to be the most influential among others (transverse and spanwise normal stresses) and the remaining normal stresses are suppressed to forcibly have the same magnitude, always satisfying the ratio of turbulent intensities in each direction as 2:1:1, which is not always the case for bubble-column (Rensen et al. 2005) and bubble-swarm experiments (Roig & de Tournemine 2007; Riboux et al. 2010). Most importantly, the exact balance equation for the Reynolds stress has not been established such that different components in the budget are argued to be dominant under similar bubbly

configurations (turbulent bubbly flows with $\langle \bar{\alpha} \rangle < 3\%$ and $Re_D < 7,500$) (Kataoka et al. 1992; du Cluzeau et al. 2019; Ma et al. 2020). Although this computationally demanding approach can provide both diagonal of off-diagonal components of the Reynolds stress without any tuning parameters (equation 1.3), it is not intuitively understandable with measurable flow variables and is only accurate at the core-region of the pipe where the bubbles are distributed uniformly, which is an obvious limitation of the applicability. Furthermore, to solve (close) the Reynolds stress budget (equation 1.3), external models such as the drag force in the interfacial transfer balance ($s_{Ri,j}$) are needed. Therefore, substantial progress in the second-moment closure for the Reynolds stress seems to be needed to overcome the inability to predict the spatially-varying turbulent statistics in non-uniform bubbly flows.

1.2.3 An alternative way

An intermediate strategy to model BIT between the level of linear eddy-viscosity assumption and the second-moment closures is explicit algebraic Reynolds stress models (or simply EARSM), which is not derived from the new background, but complements the typical shortcomings of the first and second approaches, while at the same time proposing an intuitively understandable, straightforward and cost-effective predictive model based on appropriate assumptions. To the best of our knowledge, heretofore, the EARSMs were developed in a similar form based on the two-phase eddy-viscosity assumption at a small bulk Reynolds number (Sato & Sekoguchi 1975; Hosokawa & Tomiyama 2013; Kim et al. 2016). As a first attempt to model the bubble-induced shear stress ($-\rho_l \overline{u_1'' u_2''}$), Sato & Sekoguchi (1975) proposed the two-phase eddy-viscosity based on an inviscid-mixing length ($\nu_t'' = \bar{\alpha} (0.6 \bar{d}_b \bar{u}_{1b})$) in two-phase flow in addition to that existing in the single-phase flow, and the resultant turbulent (shear) stress is expressed as follows:

$$\tau_{12}^{Total} = -\rho_l \left(\overline{u_1' u_2'} + \overline{u_1'' u_2''} \right) = -\rho_l \left(0.09 \frac{k^2}{\varepsilon} + \alpha \cdot 0.6 \bar{d}_b \bar{u}_{1b} \right) \frac{d\bar{u}_1}{dx_2}, \quad (1.4)$$

here, subscript ‘ l ’ denotes the streamwise direction and the Reynolds stress in the single-phase flow is estimated by the classical k - ε model, however, in this study, the single-phase balance equations for the turbulent kinetic energy (k) and the dissipation rate (ε) are adopted without any modifications in estimating $-\rho_l \overline{u_1' u_2'}$. On the other hand, this turbulent stress model (equation 1.4) exclusively emphasizes contributions by the drifted liquid flow (an inviscid flow) by bubbles while contributions by the spatial- (attached-wake) and temporal-fluctuation (nonlinear detached-wake interactions) by which most of the bubble-induced turbulent kinetic energy is generated are neglected (Risso 2018). Therefore, this model is adequate for a dilute bubbly flow and is only accounts for one-sixth of all the Reynolds stress, thus the remaining closures should be modeled separately. Later, an identical quantity has been explicitly modeled by Hosokawa & Tomiyama (2013) in laminar bubbly pipe flows ($Re_D = 900$ with $\langle \bar{\alpha} \rangle < 1.27\%$) where they additionally consider the effects by inhomogeneity in the local void fraction ($\partial \bar{\alpha} / \partial x$) and relative bubble velocity ($\partial \bar{v}_r / \partial x$) on the bubble-induced turbulent stress while neglecting the imposed external turbulence (e.g., shear-induced turbulence) as:

$$\tau_{12}^{BIT} = -\rho_l \overline{u_1'' u_2''} = -c \rho_l \bar{d}_b \bar{u}_{1r} \bar{\alpha} \left(\frac{d\bar{u}_1}{dx_2} + \frac{d\bar{u}_{1r}}{dx_2} \right) - c \rho_l \bar{d}_b \bar{u}_{1r} \bar{u}_{1g} \frac{d\bar{\alpha}}{dx_2}, \quad (1.5)$$

where subscripts ‘ b ’ and ‘ r ’ denote the gas- and relative gas-phase with respect to the liquid-phase. Interestingly, the first-term in the RHS of the equation 1.5 is coincided with the pure inviscid model (equation 1.4) by Sato & Sekoguchi (1975) thus can be interpreted as a contribution by the drifted liquid flow in the vicinity of a bubble while the second and third terms are originated from turbulent production *via* the destabilization in the mean relative bubble velocity as well as the non-uniform bubble distribution by the wall. Compared to the Sato & Sekoguchi (1975) model, Hosokawa & Tomiyama (2013) (equation 1.5) reports that the spatial gradient of the superficial gas-phase flux ($j_g = \alpha \cdot v_b$) is the main source of producing bubble-induced turbulence in the laminar bubbly pipe flow, however, we have observed that non-negligible turbulent stress is developed where bubbles are uniformly distributed (Kim, Lee & Park 2016; Lee & Park 2020; Lee et al. 2021).

Although the proposed model (equation 1.5) is capable of predicting the bubble-induced turbulence both at the core- and near wall-region of pipes, however predictive performance is insufficient, and some coefficients still need to be empirically tuned for each experimental condition, meaning that they are unpractical. On the other hand, there is a characteristic that the influences of the complex wake interactions are oversimplified, thus prediction performance becomes degraded at the higher volume void fractions ($> 2.17\%$), especially near the solid walls. Furthermore, when modeling the diagonal terms of the bubble-induced normal stresses as a follow-up study, they do not give any clue to readers. The representative studies mentioned above (Sato & Sekoguchi 1975; Tomiyama & Hosokawa 2013) lack through discussions on the fluctuating nature of the complex bubble-induced turbulence (e.g., bubble wakes' interactions) and fail to reflect them in the developed models.

On the other hands, diagonal components of the bubble-induced Reynolds normal stress have also been estimated by an inviscid flow in a dilute dispersion by the integration of the velocity induced by a single bubble over the volume V external to the bubble (Nigmatulin 1979):

$$\overline{u_j'' u_j''} = \frac{\alpha}{\frac{\pi d_b^3}{6}} \int_V u_j'' u_j'' dV = \alpha \cdot 2 \begin{pmatrix} 4/10 & 0 & 0 \\ 0 & 3/10 & 0 \\ 0 & 0 & 3/10 \end{pmatrix} \cdot \frac{1}{2} c_{vm} \bar{v}_r^2, \quad (1.6)$$

where c_{vm} is the virtual-mass coefficient which is 0.5. However, this is simply derived from the inviscid flow passing through a cylindrical bubble when the volume void fraction is rather low, thus the accuracy of the estimation at relatively high $\langle \bar{\alpha} \rangle$ is questionable without considering the bubble wake effect. Moreover, it only provides streamwise and spanwise normal stress terms, thus separate turbulent (shear) stress prediction models are needed. On the other hand, EARSMS derived from the transport equation for Reynolds stress (equation 1.3) are a bit simpler and have the advantages of not including any tuning parameters (Ma et al. 2020) as:

$$\overline{u_i'' u_j''} = \frac{k}{c_l (1 - \alpha) \varepsilon} S_{R,ij} + \frac{2}{3} \delta_{ij} k \left(1 - \frac{1}{c_l} \right) \quad (1.7)$$

where the prefactor c_l equals 1.63, and $S_{R,ij}$ represents interfacial momentum transfer at the phases' boundaries while k and ε denote TKE and dissipation rate in liquid-phase, meaning that, to apply this model, solving an additional balance

equation for the TKE and ε respectively is required per grid, which is demanding and inefficient. Moreover, the interfacial transport term is expressed as:

$$S_{R,ij} = \begin{pmatrix} \underbrace{\min 0.67 \cdot (1 + \exp(370 \text{Re}_p^{-1.2}), 2)}_{b_{11}^*} & 0 & 0 \\ 0 & \underbrace{\frac{1}{2}(2 - b_{11}^*)}_{b_{22}^*} & 0 \\ 0 & 0 & b_{33}^* = b_{22}^* \end{pmatrix} \cdot S_k. \quad (1.8)$$

To close equation 1.8, an additional source term (S_k) for TKE is needed. In equation 1.8, too many restrictions have been made such that Reynolds stresses in each direction do not vary in time, i.e., $D(-\overline{u_i''u_j''}/k)/Dt = 0$, and turbulence production (P_{ij} in equation 1.3) is assumed to be negligible compared to the momentum transfer by bubbles (equation 1.8), and most importantly, this complex model cannot predict the spatial-variation of the turbulent statistics near the wall-region as its basis does, all of which are different from actual physics.

Above all, in EARSMS to date, it fails to provide a universally applicable predictive model for any Reynolds stresses for wider ranges of volume void fraction and bulk liquid Reynolds number.

1.3 Main purposes

Therefore, the main purpose of the present study is to contribute to solving the additional closure problem that is inevitably encountered in bubbly flows by extending the idea of the classical single-phase mixing-length theory for both SIT- (shear-induced turbulence) and BIT-dominated flows. The proposed EARSMS should be intuitively understandable with measurable flow variables, not computationally demanding, and do not include any empirical tuning prefactor, thus they are capable of better representing the spatially-varying turbulence statistics near and away from the solid walls (circular cylinder or pipe walls) for wider ranges of volume void fractions ($\mathcal{O}(10^{-2} \sim 10^{-1})$) and bulk liquid Reynolds number ($Re_D \sim \mathcal{O}(10^5)$). Besides, by comparing the developed models with previous experiments available in the literature, the tendency of bubble-induced

turbulence enhancement (and also suppression) should be predicted simultaneously, and we objectively evaluate the strength and weakness of the proposed models. Lastly, our plan for constructing a full-set explicit Reynolds stress model is presented.

As a good example to validate the developed models, we have configured the homogeneous bubble-swarm in quiescent liquid where all the gas- and liquid-phase statistics are uniform in space and let the bubble-induced mean liquid flow passes around a circular cylinder. Thus, the turbulent nature of the pure bubble-induced turbulence (BIT) is confirmed at upstream and its variations when it is surrounded by the cylinder wake in downstream are discussed concretely to incorporate our observations in the developed models. Furthermore, we expand the independent validation by comparing the prediction results with bubbly internal flows like wall-bounded laminar and turbulent bubbly flows available in the literature.

Chapter 2.

An explicit algebraic model for the bubble-induced turbulence

2.1 Derivation of the two-phase mixing-length

2.1.1 A gravity-driven bubble-swarm

The classical definition of the mixing-length is analogous to the concept of a mean free path in thermodynamics that fluid elements of a finite size conserve their properties for a characteristic length (l_b) before mixing with the surrounding liquid. In bubbly flows, the existence of bubbles increases the rate at which the fluid elements mix with the surrounding fluid, shortening the characteristic length (l_b), which is exclusively confined to the vicinity of bubbles far from their detached wakes. Thus, it has been frequently associated the drifted-length in liquid-phase induced by bubbles, therefore it makes sense to model the mixing-length in bubbly flows by an inviscid flow by which liquid displacement is dominantly induced at bubbles' proximities (Risso 2018). However, it does not necessarily mean that all the BIT come from the inviscid flow, instead, by better representing the realistic mixing-length in bubbly flows, and starting from here, we intend to additionally reflect the turbulent nature of the bubble-induced turbulence. It is worth noting that, in the probability density functions (PDFs) of bubble-induced liquid fluctuations, an inviscid flow produces the largest liquid perturbation than the rest of the contributions (e.g., an averaged-wake and temporal wakes instabilities) (Risso 2016).

Previously, Sato & Sekoguchi (1975) formulated the liquid displacement ($\sim l_b$) in the transverse direction induced by a single cylindrical bubble rising with $\langle \bar{v}_b \rangle$ in stagnant liquid as $l_b \sim \langle \bar{d}_b \rangle$, meaning that the drifted-length in liquid-phase is only determined by the size of a bubble regardless of the bubble number density, which is different in actual physics. To improve this, following this attribute while supplementing the aforementioned limitations, we derive the new two-phase

mixing length from an inviscid flow around side-by-side cylindrical bubbles in a homogeneous bubble-swarm in quiescent liquid where bubbles are more or less displaced uniformly to incorporate the void fraction dependency of a bubble-induced liquid flow (bubble-wake effect) into the two-phase mixing-length model. As shown in figure 2.1, compared to the geometrical configuration by Sato & Sekoguchi (1975), we additionally placed a second cylindrical bubble at a distance of $l_m = \left(\pi/6\langle\bar{\alpha}\rangle^{-1}\right)^{1/3}\langle\bar{d}_b\rangle$ (Riboux et al. 2010; Lee & Park 2020). Here, in a homogeneous bubble-swarm where $\nabla\bar{\alpha} = 0$ it is reasonable to assume that bubbles rising against an inviscid flow at $\langle\bar{v}_b\rangle$ are uniformly distributed at a distance of l_m on average for the case of a global void fraction of $\langle\bar{\alpha}\rangle$ and bubble size of $\langle\bar{d}_b\rangle$. Thus, we pose a configuration of two bubbles displaced by l_m , and justify that locations of the rest of the bubbles are continuous repeats of this geometry (figure 2.1). Although the effect of the leading bubble wake on the trailing bubble cannot be considered, the additional deflection (or reduction) in the drifted-length in liquid-phase by the neighboring bubble can be reflected, as a function of the local void fraction ($\bar{\alpha}$), which is meaningful. In figure 2.1, two points $P_1(-\infty, y_1)$ and $P_2(0, y_2)$ are located on the same streamline (ψ_1) in the close vicinity of a rising bubble (radius of a). The liquid drifts at these points P_1 and P_2 are affected by the main bubble and deflected upward ($\Delta y_{up} > 0$), however, they are also affected by the neighboring bubble at a distance of l_m , simultaneously being pushed downward ($\Delta y_{down} < 0$). Therefore, the net displacement, $\Delta y_{up} - \Delta y_{down}$, determines the effective liquid drift. For the flow considered, the streamline can be analytically expressed by the linear superposition of the stream functions for uniform flow and two doublets, as follows:

$$\psi = \langle\bar{v}_b\rangle \left[y - a^2 \left(\frac{y}{x^2 + y^2} + \frac{y - l_m}{x^2 + (y - l_m)^2} \right) \right], \quad (2.1)$$

where $\langle\bar{v}_b\rangle$ is the mean bubble rise velocity. It is clear that the mixing length (l_b) in this flow is related to the displacement ($y_2 - y_1$) at $\eta = y_1$ over which point P_2 is drifted by the existence of both bubbles, and $y_2 - y_1$ can be analytically

calculated provided that coordinates of two points P_1 and P_2 on the identical streamline ($\psi_{1, P_1} = \psi_{1, P_2}$) are considered in the equation 2.1 as follows:

$$y_2 - y_1 = -a^2 \left(\frac{1}{l_m - y_2} - \frac{1}{y_2} \right). \quad (2.2)$$

Owing to $|y_2/l_m| < 1.0$, which is reasonable for the considered low volume void fraction conditions, we apply Taylor expansion to the first term on the right-hand-side of equation 2.2, and neglect the negligible high-order terms, i.e., $\sim \mathcal{O}((-y_2/l_m)^2)$, and expand:

$$(l_m^2 + a^2)y_2^2 - l_m(l_my_1 - a^2)y_2 - a^2l_m^2 = 0. \quad (2.3)$$

This second-order equation for y_2 is explicit, and if we solve equation 2.3 with respect to y_2 , the mixing length ($l_b \cong y_2 - y_1$) is obtained as follows:

$$l_b \cong \frac{\langle \bar{d}_b \rangle}{2 \left[1 + \left(\frac{\langle \bar{d}_b \rangle}{2l_m} \right)^2 \right]} \left[\sqrt{\left(\eta^* - \frac{\langle \bar{d}_b \rangle}{4l_m} \right)^2 + \left(\frac{\langle \bar{d}_b \rangle}{2l_m} \right)^2} + 1 - \left(1 + 2 \left(\frac{\langle \bar{d}_b \rangle}{2l_m} \right)^2 \right) \eta^* - \frac{\langle \bar{d}_b \rangle}{4l_m} \right], \quad (2.4)$$

here, the normalized vertical distance from the control-plane (figure 2.1) is $\eta^* = y_1/2a$. It is noted that the mixing length is related to the bubble size and the spacing between bubbles. If we define $\kappa = \langle \bar{d}_b \rangle / l_m$, with a physical meaning of kind of blockage ratio, the equation 2.4 is further simplified as:

$$l_b = c' \frac{\langle \bar{d}_b \rangle}{2 \left[1 + (\kappa/2)^2 \right]} \cdot f(\eta^*, \kappa). \quad (2.5)$$

In the non-dimensional term, $f(\eta^*, \kappa)$, the variable κ is a constant for a certain volume void fraction since we assumed the uniform distribution of bubbles, thus can be absorbed to the coefficient c' . The equation 2.5 is further expanded by assuming $\kappa < 1$, which is reasonable unless $\langle \bar{\alpha} \rangle = 1$ as:

$$l_b = c \langle \bar{d}_b \rangle \left(1 - 0.4 \langle \bar{\alpha} \rangle^{2/3} \right) \quad (2.6)$$

Again, this assumption is valid for low-to-intermediate volume void fraction. Compared to the previous model of $l_b = 0.6 \langle \bar{d}_b \rangle$ by Sato & Sekoguchi (1975),

the present one suggests that the two-phase mixing-length in the close vicinity of a bubble is affected by both the bubble size and volume void fraction. The smaller the bubble size, the smaller the l_b while the larger the volume void fraction, the coarser the mean distance between bubbles, resulting in the decreased l_b because the hindering effects by neighboring bubbles increase as the mean distance between bubbles decreases (Riboux et al. 2010). However, this model cannot be applied to another environment with inhomogeneity in local void fractions due to the existence of walls or with an imposed external momentum source in bounded bubbly flows (e.g., liquid-shear).

2.1.2 Bubbly internal flows

For a practical expression for the two-phase mixing-length in bubbly internal flows (e.g., bounded laminar and turbulent bubbly flows), we supplement the developed mixing-length model (equation 2.6) to have a dependency with the background liquid flow as well as the bubble motion with respect to the bulk liquid flow. The basic geometrical alignment of bubbles in a channel (pipe) is identical to the previous one as shown in figure 2.2, we analytically derive the liquid-displacement ($\sim l_b$) by two side-by-side bubbles when they rise with $\langle \bar{v}_r \rangle$ against the background linear-shear ($\partial \bar{v}_r / \partial x$) near the wall-region. To achieve this, we postulate two assumptions. We previously confirmed that, for a fixed volume void fraction, the averaged-distance between bubbles in a homogeneous bubble-swarm in quiescent liquid is $l_m = \left(\pi/6 \langle \bar{\alpha} \rangle^{-1} \right)^{1/3} \langle \bar{d}_b \rangle$ (Riboux et al. 2010; Lee & Park 2020), which is reasonable in that configuration. One might think that distances between bubbles near the wall would be coarser ($< l_m$) due to locally higher void fraction. Here, to overcome this issue, we substitute the temporal-spatial averaged physical quantities (e.g., $\langle \bar{\alpha} \rangle$) with a two-dimensional local distribution (e.g., $\bar{\alpha}$), thus the distance ($l_m = \bar{d}_b \cdot (\pi/6 \bar{\alpha})^{1/3}$) between bubbles in the domain is not all the same, instead it is decreased near a wall for wall-peaking void distributions while is increased at the core-region of pipes ($l_m \sim \bar{\alpha}^{-1/3}$). Secondly, we assumed a

linearized mean liquid velocity gradient near the wall, which is in fact known to obey the logarithmic law (Marié, Moursali & Tran-Cong 1997; Nakoryakov et al. 1981, or a new logarithmic law by Troshko & Hassan 2001). We are fully aware that reflecting the real high-order liquid-velocity distribution in pipes is by no means trivial. Instead, to avoid the complexity in the resultant turbulence model which is inevitably related to potential applicability in EE RANS simulation, we decide to adopt this first-order approximation, i.e., linear-shear. Nevertheless, the additional liquid displacement made by the difference between the linearized-shear and the actual gradient of the mean liquid flow is negligible, thus we judge that it does not matter what form is taken for this issue.

Let us explain the detailed procedure to analytically derive the two-phase mixing-length. In figure 2.2, the two points $P_1(-\infty, y_1)$ and $P_2(0, y_2)$ are located on the same streamline ($\psi = \psi_1$) in the vicinity of a rising cylindrical bubble with a radius of $a = \langle \bar{d}_b \rangle / 2$. Similarly, The drifted-length in liquid-phase at these points P_1 and P_2 is affected by the main bubble and thus deflected upward ($\Delta y_{up} > 0$), while it is also affected by the neighboring bubble at a distance l_m from the origin, being pushed downward simultaneously ($\Delta y_{down} < 0$). Therefore, the net displacement, i.e., $\Delta y_{up} - \Delta y_{down}$, is scaled with the effective two-phase mixing-length (l_b). The streamline can be analytically expressed by the linear superposition of the stream functions for linear-shear flow and two doublets as follows:

$$\psi = \langle \bar{v}_r \rangle y + \frac{c}{2} y^2 - \mu \left(\frac{y}{x^2 + y^2} + \frac{y - l_m}{x^2 + (y - l_m)^2} \right), \quad (2.7)$$

where c is the background shear-rate with respect to the bubble motion which is $\partial \bar{v}_r / \partial x$ and the strength (μ) of two identical doublets that are vertically separated by l_m is

$$\mu = \langle \bar{v}_r \rangle a^2 + \frac{c}{2} a^3. \quad (2.8)$$

It is clear that the mixing length (l_b) in this flow (figure 2.2) is related to the displacement ($y_2 - y_1$) at $\eta = y_1$ over which point P_2 is drifted by the existence of both bubbles rising with the relative bubble velocity, and also by the linearized-shear near the wall-region, and $y_2 - y_1$ can be analytically derived, provided that

coordinates of two points P_1 and P_2 on the identical streamline ($\psi_{l, P_1} = \psi_{l, P_2}$) are considered in the equation 2.7 as follows:

$$\frac{cy_1^2}{2} + \langle \bar{v}_r \rangle y_1 = \frac{cy_2^2}{2} + \langle \bar{v}_r \rangle y_2 - \mu \left(\frac{1}{y_2} + \frac{1}{y_2 - l_m} \right). \quad (2.9)$$

Rearranging this equation 2.9 yields a fourth-order equation with respect to y_2 :

$$\begin{aligned} \frac{c}{2} y_2^4 + \left(\langle \bar{v}_r \rangle - \frac{cl_m}{2} \right) y_2^3 + \left(-\langle \bar{v}_r \rangle l_m - \frac{c}{2} y_1^2 - \langle \bar{v}_r \rangle y_1 \right) y_2^2 \\ + \left(\frac{cl_m}{2} y_1^2 + \langle \bar{v}_r \rangle l_m y_1 - 2\mu \right) y_2 + \mu l_m = 0. \end{aligned} \quad (2.10)$$

This explicit fourth-order equation for y_2 is analogous to equation 2.3, and if we solve the equation 2.10 with respect to y_2 , the mixing length ($l_b \cong y_2 - y_1$) is obtained as follows:

$$l_b = c' \left(\langle \bar{d}_b \rangle \langle \bar{\alpha} \rangle^{-1/3} - 2 \langle \bar{v}_r \rangle \cdot (\partial \bar{v}_r / \partial x)^{-1} \right) \cdot f(\eta^*, \kappa), \quad (2.11)$$

here dimensionless function f is expressed with two variables: $\eta^* (= y_1 / \langle \bar{d}_b \rangle)$, the dimensionless distance from the centroid of the main bubble and $\kappa = \langle \bar{d}_b \rangle / l_m$, which is a kind of blockage ratio by bubbles, both of which are scalars. Thus, the function f is an arbitrary constant, consequently, having the same attribute with Sato & Sekoguchi (1975), this can be absorbed into the empirical coefficient (c') while we adopt the correlation for l_m by Riboux et al. (2010) in the equation 2.10. Consequently, the resultant two-phase mixing-length in bounded laminar and turbulent bubbly flows can be explicitly expressed as:

$$l_b = c \left(\bar{d}_b \bar{\alpha}^{-1/3} - 2 \bar{v}_r \cdot (\partial \bar{v}_r / \partial x)^{-1} \right), \quad (2.12)$$

here, as mentioned before, we substitute the temporal-spatial averaged physical quantities (e.g., $\langle \bar{\alpha} \rangle$) with a two-dimensional local distribution (e.g., $\bar{\alpha}$). The practical mixing-length model (l_b) is now comprehensively affected by not only the bubble size and local void fraction, but also the rising velocity of a bubble relative to the bulk liquid flow (\bar{v}_r) and mean shear-rate ($\partial \bar{v}_r / \partial x$). When a bubble rises slowly in a region with a steep liquid-shear, the liquid displacement by the bubble

is expected to be increased, which corresponds to our physical intuition and a previous study (Adoua et al. 2009). Indeed, due to the side-by-side bubbles' arrangement, the effect of the wake of the leading bubble on the trailing bubble still cannot be considered in l_b itself. Nevertheless, it is meaningful that we try to explicitly express the modified mixing-length (l_b) in bubbly flows in the presence of the background liquid flow, which is capable of simultaneously predicting l_b at both the core- and near wall-region of pipes with multiple bubbles, depending on flow geometries and conditions.

To confirm the developed models for the two-phase mixing-length in a homogeneous bubble-swarm in quiescent liquid (equation 2.6) and bounded laminar and turbulent bubbly flows under an imposed pressure gradient (equation 2.12), we have visualized the signature of the time-averaged two-phase mixing-length (\bar{l}_b) for two representative cases in figure 2.3. In a homogeneous bubble-swarm past a circular cylinder in quiescent water (Lee & Park 2020), the traces of the time-averaged mixing-length exhibiting somewhat elongated streaks are pronounced along the region with the mildest gradients of the mean relative velocity ($\partial\bar{v}_r/\partial x$) and the local void fraction ($\partial\bar{\alpha}/\partial x$) (a solid-arrow in figures 2.3a-b). For the higher volume void fraction case ($\langle\bar{\alpha}\rangle = 1.1\%$ in figure 2.3b) where incident bubbles are accumulated in the wake behind the cylinder ($|x/D| \leq 0.5$), an intense bubble-bubble interaction there (e.g., coalescence) makes the bubbles grow larger, resulting in distinctive \bar{l}_b signatures, which is also the case along with the separating liquid shear layers for $\langle\bar{\alpha}\rangle = 0.6\%$ (dashed-box in figure 2.3a). For turbulent bubbly pipe flows (Lee et al. 2021), the traces of the time-averaged mixing-length are rather discrete, spreading over the entire domain. Especially near the wall-region with a steep $\partial\bar{v}_r/\partial x$ and $\partial\bar{\alpha}/\partial x$, the signatures are sparsely distributed while they are more pronounced away from the wall ($|x/D| \leq 0.3$) (figure 2.3c). When the bulk liquid Reynolds number is drastically increased ($Re_D = 44,000$ in figure 2.3d), most of the traces of \bar{l}_b are disappeared immediately at both the core- and near wall-region of the pipe because an intense

wall-generated shear-induced turbulence additionally facilitates the mixing of fluid elements with surrounding liquid in addition to bubbles, i.e., BIT, which makes the signatures of the time-averaged two-phase mixing-length disappear rapidly. Interestingly, near the wall-region where a steep liquid-shear exists, significant bubble-bubble interactions (e.g., coalescence or break-up) occur, which could contribute to enhancing the level of the \bar{l}_b signatures (equation 2.12), but it is not in measured physics. This is because intense bubble' interactions near the wall actually act in a direction of breaking the bubbles.

As noted, the concept of the two-phase mixing-length (equations 2.6 and 2.12) is classically confined to the proximity of a bubble (Sato & Sekoguchi 1975; Lee & Park 2020) at which an inviscid flow is dominant (Risso 2016). With this inviscid expression alone, the bubble-induced Reynolds stresses (e.g., $\overline{u_1''u_1''}$, $\overline{u_2''u_2''}$, $\overline{u_3''u_3''}$, $\overline{u_1''u_2''}$, $\overline{u_1''u_3''}$, $\overline{u_2''u_3''}$) cannot be predicted completely in bounded (or unbounded) bubbly flows. In the following, we devise additional considerations that can physically reflect the dynamics of the bubble wakes.

2.2 A scaling law for the mean liquid velocity

2.2.1 An unbounded quiescent liquid

To analytically model the bubble-induced turbulence based on the two-phase mixing-length theory, it necessitates the representative mean turnover length (l_b) of eddies in bubble-induced flows (equations 2.6 and 2.12) and the bubble-induced mean liquid-shear ($\partial\bar{v}_l/\partial x$), thus the representative velocity-scale is asymptotically scaled as $v \cong l_b \cdot |\partial\bar{u}_i/\partial x|$ (Sato & Sekoguchi 1975; Troshko & Hassan 2001). Therefore, to consider the bubble-wake effect (turbulent contribution) together, we start with the scaling relation, which determines that the bubble-induced streamwise mean liquid velocity (\bar{v}_l) of a single bubble rising in quiescent water is proportional to the terminal velocity (V_o) (Batchelor 1967; Ellingsen & Risso 2001). On the other hand, the empirical relation between mean bubble rise velocity ($\langle\bar{v}_b\rangle$) and a global void fraction ($\langle\bar{\alpha}\rangle$) has been suggested for

a gravity-driven homogeneous bubble swarm (Risso & Ellingsen 2002; Riboux et al. 2010; Risso 2018) as:

$$\langle \bar{v}_b \rangle \sim V_0 \langle \bar{\alpha} \rangle^{-0.1}. \quad (2.13)$$

This correlation holds for $0.002 \leq \langle \bar{\alpha} \rangle \leq 0.12$, and it is approximately reported that the hindrance effect makes the mean bubble velocity to be a decreasing function of the volume void fraction, provided that the effect of the mean liquid velocity and the corresponding shear-induced turbulence is negligible. On the other hand, this robust approximation (equation 2.13) was already noticed for a narrow range of the volume void fractions ($0.005 \leq \langle \bar{\alpha} \rangle \leq 0.01$) and a single bubble diameter (d_b of 2.5 mm) by Risso & Ellingsen (2002) and then reported by Martínez-Mercado et al. (2007) for broad ranges of bubble Reynolds numbers ($50 < Re_b < 500$) and volume void fractions ($0.01 \leq \langle \bar{\alpha} \rangle \leq 0.1$). Most recently, this relation is also confirmed by Kim et al. (2016) and Lee & Park (2020). Thus, collecting these relations, we can deduce the following relation:

$$\bar{v}_l \sim V_0 \sim \langle \bar{v}_b \rangle \langle \bar{\alpha} \rangle^{0.1} \sim \bar{v}_b \cdot \bar{\alpha}^{0.1}, \quad (2.14)$$

here, since we are interested in the spatial variation of the statistics, which is important for the present problem, we further substitute temporal-spatial averaged physical quantities in equation 2.14 with local distributions. This does not violate the proposed scaling law based on the linear evolution between $\langle \bar{\alpha} \rangle$ and $\bar{\alpha}$ in a buoyancy-driven homogeneous bubble-swarm experiment, as shown in figure 2.4(a). A more detailed explanation of these experiments would be provided later. Thus, for now, we just look at the overall trend. This argument also holds for the mean bubble diameter (figure 2.4b) and mean bubble rise velocity (figure 2.4c) even inside the weak cylinder wake. Therefore, the last relation in equation 2.14 has no bias in this context.

We also checked whether the resultant scaling law of $\bar{v}_l \sim \bar{v}_b \cdot \bar{\alpha}^{0.1}$ is valid for the present study. As shown in figure 2.4(d), this relation is roughly satisfied at the upstream and the outside the cylinder wake ($|x/D| > 0.5$). It is noted that this scaling relation shows a relatively larger deviation (about 13% on average) from the

measurement inside the cylinder wake ($|x/D| \leq 0.5$). Thus, we judge that it is not completely wrong to expand this correlation to the cylinder wake. Consequently, the developed scaling law (equation 2.14) tells us that the faster the bubble rises, or the more bubbles there are in the domain, the faster the mean liquid velocity is induced, which corresponds to our physical intuition. Therefore, the bubble-induced mean liquid-shear ($\partial \bar{v}_l / \partial x$) in quiescent liquid is further derived by mathematically differentiating the last correlation in equation 2.14 as follows:

$$\frac{\partial \bar{v}_l}{\partial x} \sim \bar{\alpha}^{0.1} \frac{\partial \bar{v}_b}{\partial x} + 0.1 \bar{v}_b \bar{\alpha}^{-0.9} \frac{\partial \bar{\alpha}}{\partial x}. \quad (2.15)$$

This shows that the streamwise mean liquid velocity gradient can be related to the gradients of mean bubble rise velocity and local void fraction, in which gravity-driven bubbles are the only momentum and turbulence source in the present configuration. Therefore, a locally steep gradient of the local void fraction ($\partial \bar{\alpha} / \partial x$), i.e., an inhomogeneity in bubbles' distribution, inevitably induces gradients of the mean absolute and relative bubble velocities because the local liquid motion initially at rest is only induced by rising bubbles. As we mentioned before, the proposed relations for the gravity-driven bubble-induced mean liquid velocity are only valid for the static liquid condition. If there are external momentum sources (e.g., an imposed pressure gradient), then different theoretical reasoning is needed for the expansion of the proposed relations (equations 2.14 and 2.15).

2.2.2 A wall-bounded dynamic liquid

To account for the complex bubble wake effects (e.g., turbulent and non-turbulent parts of BIT), we additionally developed an identical scaling relation for the mean liquid velocity (\bar{v}_l) as bubbles rise against the bulk liquid flow, and also discussed the turbulent nature of the BIT in turbulent pipe flows especially near the wall. Previously, the mean rise velocity of bubbles in the presence of the background liquid flow, i.e., $j_l > 0$, has been experimentally proved to be correlated with $\langle \bar{v}_r \rangle = V_0 \left(1 - \langle \bar{\alpha} \rangle^{0.49} \right)$ (Garnier et al. 2002; Roig & de Tournemine 2007;

Riboux et al. 2010). Here, V_0 denotes the terminal velocity of a single bubble in quiescent water. This scaling law is not just a rough approximation, but a sophisticated model that fully reflects the complex physics of BIT (Risso 2016). If we decompose $\langle \bar{v}_r \rangle$ into $\langle \bar{v}_b \rangle - \langle \bar{v}_l \rangle$, we expect to acquire some insights in analytically modeling $\langle \bar{v}_l \rangle$. The validity that the terminal velocity (V_0) of an isolated bubble is the relevant velocity-scale for mean relative bubble rise velocity for the considered ranges of the volume void fraction (< 0.1) and Re_D ($\sim \mathcal{O}(10^4 - 10^5)$) is already discussed in Riboux et al. (2010). Therefore, having the same attribute, we deduce $V_0 \sim \bar{v}_l$ because the larger the bubble, the faster it rises, encompassing surrounding liquid into the wake. The mean liquid velocity is then scaled as a function of pure gas-phase statistics:

$$\bar{v}_l \sim V_0 \sim \langle \bar{v}_r \rangle \left(1 - \langle \bar{\alpha} \rangle^{0.49} \right)^{-1}. \quad (2.16)$$

Because we are interested in the spatial (local) variation of turbulent statistics both at the core- and near wall-region of pipes, we substitute $\langle \bar{\alpha} \rangle$ (a temporal-spatial averaged-value) with the local void fraction $\bar{\alpha}$. To justify this, we exclusively selected prior experimental studies that provide the spatially-varying gas-phase quantities (e.g., $\bar{\alpha}$, \bar{v}_r and occasionally \bar{d}_b) as well as turbulence statistics (e.g., root-mean-square of bubble-induced liquid fluctuations, turbulent stresses, and also equivalent parameters in the single-phase flow with an identical Re_D), available in the literature as shown in table 2.1. Here, the detailed explanations of the references would be provided later, thus, for now, we just look at the overall trend.

Substituting the volume void fraction into the local quantity does not violate the existing relation based on the linear correlation between $\langle \bar{\alpha} \rangle$ and $\bar{\alpha}$, exhibiting an identical slope (figure 2.5a) (Lee & Park 2020) as $\bar{v}_l \sim \bar{v}_r \left(1 - \bar{\alpha}^{0.49} \right)^{-1}$. If we expand the last correlation with the Taylor series ($\bar{\alpha}^{0.49} < 1$) and ignore negligible high-order terms ($\mathcal{O}(\bar{\alpha}^{0.49})^2$), which does not alter the order of accuracy, then making this substitution finally results in a scaling law for mean liquid velocity as a function of gas-phase statistics as follows:

$$\bar{v}_l \sim \bar{v}_r \left(1 + \bar{\alpha}^{0.49}\right). \quad (2.17)$$

The mean liquid velocity is accelerated where more bubbles are populated, and the faster bubbles rise relative to the bulk liquid flow, the faster the existing liquid velocity accelerates. More specifically, it is found that as the local void fraction in a system with bulk liquid flow increases, the interaction between bubbles (e.g., coalescence at the wall) occurs more actively (Roig & de Tournemine 2007; Riboux et al. 2010; Kim et al. 2016; Alm eras et al. 2017; Risso 2018; Lee & Park 2020). Thus, enlarged bubbles are more accelerated due to the enhanced buoyancy ($\sim \langle \bar{d}_b \rangle^3$) under an imposed (external) pressure-gradient in the main flow direction.

This phenomenon is quite common near the wall with a wall-peaking void distribution, which is also consistent with own experience (Lee et al. 2021). To independently check the robustness of the proposed scaling law (equation 2.17) for wider ranges of $\langle \bar{\alpha} \rangle \sim \mathcal{O}(10^{-2}-10^{-1})$ and $Re_D \sim \mathcal{O}(10^5)$, to the best of our knowledge, we found all the previous experiments that provide information on the spatially-varying \bar{v}_r , \bar{v}_l and $\bar{\alpha}$, (table 2.1), and applied them to our model as shown in figure 2.5(b). Because the gas-phase statistics in the preceding data are basically similar ($Re_r \sim \mathcal{O}(10^3)$ and $We \sim \mathcal{O}(1)$), all of which exhibit deformable ellipsoidal shapes with path instabilities (Clift et al.1978), they follow the scaling law fairly well at both the core- and near wall-region in laminar and turbulent bubbly flows, and it is worth noting that the slope is close to unity. In particular, For laminar-to-transient bubbly flows (approximately $Re_D \leq 5,300$), the data stay below the identical-line while those from turbulent flows are generally above due to an intense imposed pressure-gradient in liquid-phase, comprehensively showing an average accuracy of 70%, which is by no means trivial. Nevertheless, we justify that we intend not to predict the absolute magnitude of \bar{v}_l , but to asymptotically scale \bar{v}_r as a function of gas-phase statistics, in this context, the proposed correlation (equation 2.17) reasonably follows experiments. Confined to the works by Shawkat et al. (2008), however, the measured data themselves have a steep slope (> 1). We suspect that this is not because the physical scale of bubbles agitating the surrounding liquid is significantly smaller than the channel diameter

$\langle \bar{d}_b \rangle / D \sim \mathcal{O}(10^{-2})$), but rather is originated from underestimations in \bar{v}_r (e.g., $\langle \bar{v}_r \rangle = 0.35$ m/s for $Re_D = 154,000$), which lacks realism. Thus, to account for this behavior precisely, further theoretical justification is needed as future work.

Therefore, the mean liquid-shear ($\partial \bar{v}_l / \partial x$) in dynamic liquid is further derived by mathematically differentiating the last correlation in equation 2.17 as follows:

$$\frac{\partial \bar{v}_l}{\partial x} \sim \left(1 + \bar{\alpha}^{0.49}\right) \frac{\partial \bar{v}_r}{\partial x} + \bar{v}_r \bar{\alpha}^{-0.51} \frac{\partial \bar{\alpha}}{\partial x}. \quad (2.18)$$

This shows that the streamwise mean liquid velocity gradient can be related to the gradients of mean relative bubble rise velocity and local void fraction in an environment where a bulk liquid flow exists innately. Therefore, a locally steep gradient of the local void fraction ($\partial \bar{\alpha} / \partial x$), i.e., an inhomogeneity in bubbles' distribution (e.g., a wall- (core-) peaking $\bar{\alpha}$), inevitably induces gradients of the mean relative velocity as well as the mean liquid velocity because a fully-developed stable background liquid flow is destabilized by the existence of non-uniformly distributed bubbles. As we mentioned before, the proposed relations for the mean liquid velocity under an imposed pressure gradient are only valid for the dynamic liquid condition.

2.3 Derivation of the explicit algebraic Reynolds stress models

2.3.1 A gravity-driven bubbly external flow

To date, the history of liquid turbulence by bubbles has been quite consistent, and basic characteristics that constitute the pure bubble-induced turbulence (agitation) have been identified rigorously (Risso & Ellingsen 2002; Riboux et al. 2010; Risso 2016, 2018). Furthermore, theoretical reasoning for them is quite solid and relevant. In previous studies and own experience, even with a small volume void fraction, a substantial liquid agitation is induced and this phenomenon occurs in common in various configurations (Roig & de Tournemine 2007; Alm eras et al. 2017; Lee & Park 2020), to name but a few. Especially, due to its fluctuating nature,

the bubble-induced turbulence has been compared with the single-phase equivalent (Liu & Bankoff 1993; Sato & Sekoguchi 1975; Shawkat et al. 2008; Hosokawa & Tomiyama 2013; Kim et al. 2016; du Cluzeau et al. 2019; Lee et al. 2021). The measured (total) turbulence in a bubbly flow is decomposed into the shear-induced (or wall-generated) turbulence in the absence of bubbles (SIT) and disturbances by bubbles (BIT). As mentioned, the nonlinear interaction between them does exist (du Cluzeau et al. 2019) especially for a higher Re_D , however characterizing the complex mechanism behind the interaction between SIT and BIT is by no means trivial, and isolating this is even more difficult until now in the community. Nevertheless, predicting the total turbulence by linearly superposing each contribution (SIT and BIT with the same Re_D) without quantifying mutual interactions still satisfactorily reproduces the measured experiments, thus we have no choice but to follow this attribute. On the other hand, the BIT is further decomposed into non-turbulent (an inviscid flow and an averaged-wake) and turbulent (nonlinear temporal instabilities between detached wakes) contribution (Risso & Ellingsen 2002; Risso 2016).

In the framework of the two-phase mixing-length theory, we simultaneously model the explicit bubble-induced Reynolds normal stress in streamwise direction ($\rho_l \overline{v_1'' v_1''}$) and shear stresses ($-\rho_l \overline{v_1'' u_1''}$), which is equivalent to ($-\rho_l \overline{u_1'' v_1''}$), which amounts to one-third of all the closures. Although some studies separately model the diagonal or off-diagonal components of the bubble-induced Reynolds stress tensor in the community (Sato & Sekoguchi 1975; Nigmatulin 1979; Tomiyama & Hosokawa 2013; Ma et al. 2020), this is the first attempt to model them together using the same principle. As we mentioned in the introduction, our new approach to model the streamwise liquid fluctuation is to decompose the contributions from the typical (well-known) turbulent nature of the bubble-induced agitation and from the additional disturbance by turbulence modulation by the existence of bluff bodies in bubbly external flows or sidewalls in bubbly internal flows. The first source has been well established in many studies such that the streamwise (and also transverse) liquid fluctuation in a homogeneous bubble swarm is scaled to the volume void fraction as:

$$v_i'' \sim V_0 \langle \bar{\alpha} \rangle^{0.4}, \quad (2.19)$$

where V_0 is the terminal rise velocity of a single bubble (Risso & Ellingsen 2002; Martínez-Mercado et al. 2007; Roig & de Tournemine 2007; Riboux et al. 2010; Kim et al. 2016; Risso 2018). Provided the bubble Reynolds number (Re_b) is large enough, the wake of a single bubble becomes unstable and the bubble performs path oscillations. This explains why the agitation of the bubbles still exists as the volume void fraction tends towards zero. On the other hand, the typical characteristics of the probability density function (PDF) of the bubble-induced liquid fluctuations which would be shown later preserve the same shape as the volume void fraction is increased. This independence already noticed for a narrow range of the volume void fractions ($0.005 \leq \langle \bar{\alpha} \rangle \leq 0.01$) and a single bubble diameter (d_b of 2.5 mm) by Risso & Ellingsen (2002) and then reported by Martínez-Mercado et al. (2007) for broad ranges of bubble Reynolds numbers ($50 < Re_b < 500$) and volume void fractions ($0.01 \leq \langle \bar{\alpha} \rangle \leq 0.1$). This nature, to the best of our knowledge, was confirmed to be valid for the volume void fraction up to at least 0.14.

Now we came back to the present study, if we define the additional turbulence modulation by the existence of the external turbulence sources (e.g., a circular cylinder) as $\Delta v_i''$, then the resultant (experimentally measured) turbulence can be expressed as follows:

$$v_i'' \sim V_0 \langle \bar{\alpha} \rangle^{0.4} + \Delta v_i'', \quad (2.20)$$

here, when a mean liquid flow induced by a gravity- (buoyancy-) driven homogeneous bubble-swarm in quiescent liquid is destabilized by a circular cylinder, the fluctuating nature of the pure bubble-induced turbulence would be modulated by the cylinder wake ($\Delta v_i''$). To model flow disturbances by the cylinder, $\Delta v_i''$, we keep the same approach in the original manuscript, being advanced from previous approaches (Sato & Sekoguchi 1975; Troshko & Hassan 2001; Hosokawa & Tomiyama 2013; Kim et al. 2016) based on the improved mixing-length theory (equation 2.6). That is, $\Delta v_i'' = l_b \cdot |\bar{S}_{ij}|$, where l_b and \bar{S}_{ij} are the mixing length and

mean shear-rate tensor where j is dummy variable (equation 2.6), respectively. Thus, in two-dimensional flows where the streamwise (y) variations of flow statistics are negligible, i.e., $\partial(\cdot)/\partial y = 0$, $\Delta v_l''$ reduces to $\Delta v_l'' \cong l_b \cdot |\partial \bar{v}_l / \partial x|$, here $\partial \bar{v}_l / \partial x$ is the transverse variation of the bubble-induced mean liquid velocity (equation 2.15) while, in three-dimensional flows, it becomes $\Delta v_l'' \cong l_b \cdot |\partial \bar{v}_l / \partial x + \partial \bar{v}_l / \partial z|$ where z is the spanwise direction. Here, the existence of the circular cylinder in the homogeneous bubble-swarm leads to local inhomogeneity in $\partial \bar{v}_l / \partial x$. Collecting the proposed analytical models leads to an explicit expression for the bubble-induced streamwise liquid fluctuation at a distance η^* from the control-plane (figure 2.1):

$$v_l''|_{\eta^*} = c_1 \bar{v}_b \bar{\alpha}^{0.1} \langle \bar{\alpha} \rangle^{0.4} + c_2 \bar{d}_b (1 - 0.4 \bar{\alpha}^{2/3}) f \cdot \left| \bar{\alpha}^{0.1} \frac{\partial \bar{v}_b}{\partial x} + 0.1 \bar{v}_b \bar{\alpha}^{-0.9} \frac{\partial \bar{\alpha}}{\partial x} \right|, \quad (2.21)$$

here we use the relation for the terminal rise velocity of a single bubble, that is $\bar{v}_b \sim V_0 \bar{\alpha}^{-0.1}$. Assuming that the liquid displacements caused by individual bubbles are independent of each other, the contributions of each bubble can be superposed (integrated) along the region of the periodic spatial-domain as:

$$\overline{v_l'' v_l''} = \frac{1}{T} \int_0^T \int_0^{l_m / \langle \bar{d}_b \rangle} v_l''|_{\eta^*} \cdot v_l''|_{\eta^*} d\eta^* dt. \quad (2.22)$$

When neighboring bubbles pass temporarily at a distance η^* from the control plane (figure 2.1), they instantaneously agitate the liquid flow at $\eta^* = 0$. Likewise, bubbles can be located anywhere within $0 \leq \eta^* \leq l_m / \langle \bar{d}_b \rangle$, they collectively affect the liquid fluctuation at the target plane ($\eta^* = 0$). Here, it is worth noting that we target to model the root-mean-square of the bubble-induced streamwise liquid fluctuations which is $v_{l,rms}'' = \sqrt{\overline{v_l'' v_l''}}$, because it is more relevant and convenient to compare with the previous studies. In other words, to the best of our literature survey, most of the prior experiments only provide the spatially-varying $v_{l,rms}''$ instead of $\overline{v_l'' v_l''}$. Thus, the result is given as follows:

$$\begin{aligned}
v_{l,rms}'' &= \int_0^{l_m/\langle \bar{d}_b \rangle} c_1 d\eta^* \cdot \bar{v}_b \bar{\alpha}^{0.1} \langle \bar{\alpha} \rangle^{0.4} \\
&+ \int_0^{l_m/\langle \bar{d}_b \rangle} c_2 f d\eta^* \cdot \bar{d}_b (1 - 0.4 \bar{\alpha}^{2/3}) \left| \bar{\alpha}^{0.1} \frac{\partial \bar{v}_b}{\partial x} + 0.1 \bar{v}_b \bar{\alpha}^{-0.9} \frac{\partial \bar{\alpha}}{\partial x} \right|. \quad (2.23)
\end{aligned}$$

Since the integrals can be treated as another prefactor, these can be absorbed to the existing prefactors (c_1 and c_2), thus the root-mean-square of the streamwise liquid fluctuation can be shortened as follows:

$$v_{l,rms}'' = c_{1n} \bar{v}_b \bar{\alpha}^{0.1} \langle \bar{\alpha} \rangle^{0.4} + c_{2n} \bar{d}_b (1 - 0.4 \bar{\alpha}^{2/3}) \left[\bar{\alpha}^{0.1} \left| \frac{\partial \bar{v}_b}{\partial x} \right| + 0.1 \bar{v}_b \bar{\alpha}^{-0.9} \left| \frac{\partial \bar{\alpha}}{\partial x} \right| \right]. \quad (2.24)$$

The prefactors (c_{1n} and c_{2n}) are to be determined empirically. We will validate the proposed model later. In equation 2.24, the first term refers to the contribution from a homogeneous bubble-swarm (upstream) and the second one comes from the bubbles re-distributed by a cylinder (downstream).

Now we move on to the modeling of the bubble-induced turbulent stress based on the same principle in equation 2.24. To calculate the turbulent stress, together with our model for v_l'' (equation 2.21), we adopt the transverse liquid fluctuation model (u_l'') from the inviscid drift velocity suggested by Milne-Thomson (1996):

$$u_l''|_{\eta^*} \sim \begin{cases} \langle \bar{v}_b \rangle & (|\eta^*| < 1.0). \\ \langle \bar{v}_b \rangle / \eta^{*2} & (|\eta^*| \geq 1.0). \end{cases} \quad (2.25)$$

Now let us explain our choice for this inviscid model. The existence of bubbles increases the rate at which the fluid elements mix with the surrounding fluid, shortening the characteristic length (l_b), which is exclusively confined to the vicinity of bubbles, far from their detached wakes (Sato & Sekoguchi 1975). In bubble proximities where a non-turbulent part of BIT (an inviscid flow and averaged-wake) is predominant, Risso (2016) clearly stated that the contribution of the averaged-wake concerning the transverse fluctuations (u_l'') is negligible for $\langle \bar{\alpha} \rangle$ in the range from 0.3% to 8%. That is to say, the central part of the PDF of u_l'' , which corresponds to low-to-moderate velocity fluctuations, is totally determined by the temporal wakes' interactions, while the parts at both ends of the PDF (larger fluctuations) are dominated by an inviscid flow (see the figure 5 in Risso 2016). In other words, the contributions of the averaged-wake in the variance

of u_i'' is zero, however, it is not the case for the bubble-induced streamwise liquid fluctuation (v_i''). On the other hand, the inviscid contribution is quite localized in the close vicinity of bubbles, and accounts for the most significant liquid fluctuations which are proportional to the $\langle \bar{v}_b \rangle$ as long as $\langle \bar{\alpha} \rangle$ remains small, and also gives birth to second exponential decay in the PDF of u_i'' . For that reason, we adopt an inviscid model for u_i'' . But this does not mean that everything comes from the inviscid flow, thus we reflect the complex wakes' interactions via \bar{v}_i (equation 2.14). Now we back to the turbulent stress modeling procedure, and all the submodels need to close $-\overline{v_i'' u_i''}$ are ready (equations 2.6, 2.14, and 2.15, and a reference from Milne-Thomson (1996)), and altogether, it is expressed as follows:

$$-v_i'' u_i'' \sim \left(V_0 \langle \bar{\alpha} \rangle^{0.4} + \Delta v'' \right) \cdot u_i'', \quad (2.26)$$

here, we judge that the cross-correlation between the terminal velocity of a single bubble (V_0) and u_i'' is negligible and has nothing related to the turbulent stress. Our main concern then reduces to formulate $\Delta v'' \cdot u_i''$, which equals to $(l_b \cdot |\partial \bar{v}_i / \partial x|) \cdot u_i''$. In particular, due to the anti-symmetric properties of the turbulent stress, we need all the information about the magnitude and direction of the $\partial \bar{v}_i / \partial x$ instead of $|\partial \bar{v}_i / \partial x|$. Then, analogous to the bubble-induced streamwise Reynolds stress, the Reynold shear stress can be analytically expressed as:

$$-\overline{v_i'' u_i''} = \frac{1}{T} \int_0^T \int_0^{l_m / \langle \bar{d}_b \rangle} -v_i''|_{\eta^*} u_i''|_{\eta^*} \alpha(\eta^*) d\eta^* dt. \quad (2.27)$$

The upper-bar denotes the time-averaged quantity. When neighboring bubbles pass temporarily at a distance η^* from the control plane (figure 2.1), they instantaneously agitate the liquid flow at $\eta^* = 0$. Likewise, bubbles can be located anywhere within $0 \leq \eta^* \leq l_m / \langle \bar{d}_b \rangle$, they collectively affect the liquid fluctuation at the target plane ($\eta^* = 0$). Conversely, the absence of neighboring bubbles at η^* ($\alpha(\eta^*) = 0$) does not alter the liquid flow at the control plane. Substituting the proposed submodels into equation 2.27 leads to the following equations:

$$\begin{aligned}
-\overline{v_l'' u_l''} &\cong \bar{\alpha} V_0 \langle \bar{\alpha} \rangle^{0.4} \langle \bar{v}_b \rangle \left[\int_0^{l_m / \langle \bar{d}_b \rangle} \frac{1}{\eta^{*2}} d\eta^* + 2 \right] \\
&+ \bar{\alpha} (1 - 0.4 \bar{\alpha}^{2/3}) \bar{d}_b \langle \bar{v}_b \rangle \left(\bar{\alpha}^{0.1} \frac{\partial \bar{v}_b}{\partial x} + 0.1 \bar{v}_b \bar{\alpha}^{-0.9} \frac{\partial \bar{\alpha}}{\partial x} \right) \\
&\times \left[\int_0^1 f d\eta^* + \int_1^{l_m / \langle \bar{d}_b \rangle} \frac{f}{\eta^{*2}} d\eta^* \right]
\end{aligned} \tag{2.28}$$

The integral terms in parentheses can be treated as an empirical constant and this equation can further be expanded with the definition of relative velocity,

$$\bar{v}_r = \bar{v}_b - \bar{v}_l:$$

$$-\overline{v_l'' u_l''} = (1 - 0.4 \bar{\alpha}^{2/3}) \left[c_{1r} \langle \bar{d}_b \rangle \langle \bar{v}_b \rangle \bar{\alpha}^{1.1} \frac{\partial \bar{v}_l}{\partial x} + c_{2r} \left(\bar{d}_b \bar{v}_b \bar{\alpha}^{1.1} \frac{\partial \bar{v}_b}{\partial x} + 0.1 \bar{d}_b \bar{v}_b^2 \bar{\alpha}^{0.1} \frac{\partial \bar{\alpha}}{\partial x} \right) \right] \tag{2.29}$$

During this procedure, we neglect the $c_{0r} \bar{\alpha} \langle \bar{v}_b \rangle V_0 \bar{\alpha}^{0.4}$ term because we find that the coefficient c_{0r} becomes always zero. Indeed, the neglected term only is symmetric and the remaining terms (equation 2.29) are asymmetric. Thus it is reasonable to ignore it. On the other hand, we replace the $\langle \bar{d}_b \rangle$, $\langle \bar{v}_b \rangle$ and $\langle \bar{\alpha} \rangle$ with \bar{d}_b , \bar{v}_b and $\bar{\alpha}$, respectively (figure 2.4) to predict the spatially-varying turbulence quantities more precisely. The first term on the right-hand side is similar to Sato's model (the contribution of the mean liquid velocity gradient but the mixing length is corrected to have $\bar{\alpha}$ -dependency), and the effect of the bubbles' wakes is expressed by the gradients of the relative bubble velocity and a void fraction (the second and third terms). Previously, Hosokawa & Tomiyama (2013) and Ma et al. (2020) also suggested that additional flow variables other than the mean liquid velocity gradient are necessary to reliably predict the bubble-induced turbulence in more complex flows. This is important because the role of a complicated bubble wake plays a major role in characterizing the bubble-induced turbulence, as the bubble Reynolds number and void fraction increase. The prefactors (c_{1r} and c_{2r}) are to be determined empirically. We will validate the proposed model later.

Heretofore, we have developed for the first time the bubble-induced root-

mean-square of the streamwise liquid fluctuation (equivalent to the square root of the streamwise Reynolds normal stress) (equation 2.24) and turbulent stress (equation 2.29) which account for one-third of the Reynolds stress tensor based on the same principle. These models are adequate to the unbounded homogeneous bubble-swarm where the distances between bubbles are uniform in the absence of the background liquid flow. Therefore, the proposed models cannot be applied to the bubbly internal flows (e.g., laminar and turbulent bubbly pipe (channel) flows), thus we repeat to model the identical quantities from the same principle based on the different submodels which are already explicitly modeled before.

Next, we have investigated how the bubble-induced Reynolds stress models (equations 2.24 and 2.29) would change in three-dimensional flows such as a homogeneous bubble-swarm past a sphere. In the ranges of $150 < Re_D < \mathcal{O}(10^4)$ in the single-phase flow, although an unsteady and non-periodic vortex shedding develops instantaneously, in the time-averaged sense, an axisymmetric mean liquid velocity is reported to be observed (Johnson & Patel 1997; Ozgoren et al. 2011; Cao, Tamura & Kawai 2020), meaning that both the transverse (x) and spanwise (z) variations cannot be neglected. In equation 2.20, we have already discussed how the bubble-induced streamwise liquid fluctuation model would change in three-dimensional flows, which is $v_l'' \sim V_0 \langle \bar{\alpha} \rangle^{0.4} + l_b \cdot |\partial \bar{v}_l / \partial x + \partial \bar{v}_l / \partial z|$. Therefore, the turbulent production by the spanwise (z) gradient of the mean liquid velocity also affects the streamwise liquid fluctuations, which is consistent with our physical intuition. On the other hand, our models for the two-phase mixing-length (equation 2.6) and a scaling-law for the mean liquid velocity (equation 2.14) does not vary because they are basically derived in a homogeneous bubble-swarm, but we have to additionally consider $\partial \bar{v}_l / \partial z$ which can be derived by differentiating the scaling-law for the bubble-induced mean liquid velocity (equation 2.14) with respect to the spanwise (z) direction as $\partial \bar{v}_l / \partial z \cong \bar{\alpha}^{0.1} \cdot \partial \bar{v}_b / \partial z + 0.1 \bar{v}_b \bar{\alpha}^{-0.9} \cdot \partial \bar{\alpha} / \partial z$ where both $\bar{\alpha}$ and \bar{v}_b vary in xz -plane. Finally, having the same attribute in our two-dimensional models (equations 2.24 and 2.29), the final expression of the root-mean-square of the bubble-induced streamwise liquid fluctuation can be derived as

$$v_{l,rms}'' = c_{1n} \bar{v}_b \bar{\alpha}^{-0.1} \langle \bar{\alpha} \rangle^{0.4} + c_{2n} \bar{d}_b (1 - 0.4 \bar{\alpha}^{-2/3}) \left[\bar{\alpha}^{0.1} \left| \frac{\partial \bar{v}_b}{\partial x} + \frac{\partial \bar{v}_b}{\partial z} \right| + 0.1 \bar{v}_b \bar{\alpha}^{-0.9} \left| \frac{\partial \bar{\alpha}}{\partial x} + \frac{\partial \bar{\alpha}}{\partial z} \right| \right], \quad (2.30)$$

here, this model can also be interpreted as the superposition of the pure bubble-induced turbulence (first-term) and contributions by the redistributed bubbles which are now reproduced as the transverse and spanwise gradients of the local void fraction and mean bubble rise velocity (second- and third-term). Compared to the previous model (equation 2.24), $\partial \bar{\alpha} / \partial z$ and $\partial \bar{v}_b / \partial z$ are newly added in the existing form because both models are based on the same principle (equation 2.20), and prefactors (c_{1n} and c_{2n}) are needed to be adjusted to fit the experimental data. On the other hand, the model for the bubble-induced turbulent stress in the wake behind the sphere can be expressed as

$$-\overline{v_i'' u_i''} = (1 - 0.4 \bar{\alpha}^{-2/3}) \left[c_{1r} \langle \bar{d}_b \rangle \langle \bar{v}_b \rangle \bar{\alpha}^{1.1} \left(\frac{\partial \bar{v}_l}{\partial x} + \frac{\partial \bar{v}_l}{\partial z} \right) + c_{2r} \left[\bar{d}_b \bar{v}_b \bar{\alpha}^{1.1} \left(\frac{\partial \bar{v}_b}{\partial x} + \frac{\partial \bar{v}_b}{\partial z} \right) + 0.1 \bar{d}_b \bar{v}_b^2 \bar{\alpha}^{0.1} \left(\frac{\partial \bar{\alpha}}{\partial x} + \frac{\partial \bar{\alpha}}{\partial z} \right) \right] \right]. \quad (2.31)$$

Distortions by the sphere are represented as the transverse gradients of the mean liquid and bubble velocities and local void fraction, which is the same as equation 2.29, and newly added spanwise gradients of the above-mentioned flow parameters. Comparisons with the two-dimensional model (e.g., cylinder) (equation 2.29) and the reasoning for them are similar to our analysis of equation 2.30, but in uniform flows, equation 2.31 would converge to zero. It is worth mentioning that our approach to model the bubble-induced Reynolds stress can be reliably extended to the three-dimensional flows while considering the in-homogeneously distributed bubbles by the cylinder (or sphere) and interactions of their detached wakes. In bubbly flows, if there exist previous studies that provide the distributions of flow statistics in the transverse and spanwise directions, the proposed models (equations 2.32 and 2.33) can be validated, however, we did not notice any relevant studies to the best of our knowledge.

2.3.2 Laminar and turbulent bubbly internal flows

The overall procedures to analytically model the root mean square of the bubble-induced streamwise liquid fluctuation and Reynold shear stress are the same as in the unbounded homogeneous bubble-swam past a circular cylinder (equations 2.24 and 2.29). If we define the additional turbulence modulation by the existence of the external turbulence sources (e.g., a gradient of the mean liquid velocity by sidewalls in pipes) as $\Delta v_i''$, then the resultant (experimentally measured) turbulence can be expressed as $v_i'' \sim V_0 \langle \bar{\alpha} \rangle^{0.4} + \Delta v_i''$, here when a mean liquid flow induced by a gravity- (buoyancy-) driven homogeneous bubble-swarm in quiescent liquid is surrounded by the shear-induced turbulence (or wall-generated turbulence), the fluctuating nature of the pure bubble-induced turbulence would be modulated ($\Delta v_i''$).

To obtain an equation for $\Delta v_i''$ as a function of the mean liquid flow removing any reference to the fluctuating part of the liquid velocity, we developed the two-phase mixing length (l_b) analogous to that in the single-phase flow (equation 2.12), attempting to describe momentum transfer by bubble-induced Reynolds stresses by means of an eddy viscosity as $\nu_i'' \cong l_b^2 \cdot |\partial \bar{v}_i / \partial x|$. Furthermore, we proposed a scaling law for the mean liquid velocity (\bar{v}_i) in laminar and turbulent bubbly pipe flows with wide ranges of $\langle \bar{\alpha} \rangle$ (equation 2.18), thus we relate $\Delta v_i''$ as $l_b \cdot |\partial \bar{v}_i / \partial x|$, meaning that the momentum transfer near the wall ($\partial \bar{v}_i / \partial x$) in turbulent pipe flows is modified by the mixing ($\Delta v_i''$) caused by bubble-induced energetic eddies with a length of l_b . As noted, the theoretical reasoning for this approach is basically in line with the pioneering work by Sato & Sekoguchi (1975) and following works (Nigmatulini 1979; Tomiyama & Hosokawa 2013) where they constructed the model for bubble-induced Reynolds stresses purely weighted on inviscid effects around a single cylindrical bubble, which is simple but deviates much from actual physics. Following this attribute while reinforcing the simulated simplicity, we try our best to reflect our observations.

Collecting the proposed analytical models (equations 2.12 and 2.18) leads to an explicit expression for the bubble-induced streamwise liquid fluctuation at a distance η^* from the control-plane (figure 2.2):

$$v_l''|_{\eta^*} = c_1 V_0 \langle \bar{\alpha} \rangle^{0.4} + c_2 \left[\bar{d}_b \bar{\alpha}^{-1/3} - 2\bar{v}_r \left(\frac{\partial \bar{v}_r}{\partial x} \right)^{-1} \right] f \cdot \left| \left(1 + \bar{\alpha}^{0.49} \right) \frac{\partial \bar{v}_r}{\partial x} + \bar{v}_r \bar{\alpha}^{-0.51} \frac{\partial \bar{\alpha}}{\partial x} \right|. \quad (2.32)$$

Following the same attribute as in equation 2.22, instead of predicting the bubble-induced Reynolds normal stress in the streamwise direction, we target to model the bubble-induced streamwise liquid fluctuation, i.e., $v_{l,rms}'' = \sqrt{v_l'' v_l''}$, because it is more relevant and convenient to compare with the previous studies. In other words, to the best of our literature survey, most of the prior experiments only provide the spatially-varying $v_{l,rms}''$ instead of $\overline{v_l'' v_l''}$. Thus the result is given as follows:

$$\begin{aligned} v_{l,rms}'' &= \int_0^{l_m / \langle \bar{d}_b \rangle} c_1 d\eta^* \cdot V_0 \langle \bar{\alpha} \rangle^{0.4} \\ &+ \int_0^{l_m / \langle \bar{d}_b \rangle} c_2 f d\eta^* \cdot \bar{d}_b \bar{\alpha}^{-1/3} \left| \left(1 + \bar{\alpha}^{0.49} \right) \frac{\partial \bar{v}_r}{\partial x} + \bar{v}_r \bar{\alpha}^{-0.51} \frac{\partial \bar{\alpha}}{\partial x} \right| \\ &+ \int_0^{l_m / \langle \bar{d}_b \rangle} -2c_2 f d\eta^* \cdot \bar{v}_r \left| 1 + \bar{\alpha}^{0.49} + \bar{v}_r \bar{\alpha}^{-0.51} \frac{\partial \bar{\alpha}}{\partial \bar{v}_r} \right|. \end{aligned} \quad (2.33)$$

Since the integrals can be treated as another prefactor, these can be absorbed to the existing prefactors (c_1 and c_2) while we use the relation for the terminal rise velocity of a single bubble in dynamic liquid:

$$V_0 \sim \bar{v}_r \left(1 - \bar{\alpha}^{0.49} \right)^{-1} \sim \bar{v}_r \left(1 + \bar{\alpha}^{0.49} \right), \quad (2.34)$$

where the Taylor series expansion is applied to the last relation in equation 2.24 because $\bar{\alpha}^{0.49} \leq 1$ is always satisfied. On the other hand, we mathematically differentiate the first relation in equation 2.24 to estimate the $\partial \bar{v}_r / \partial \bar{\alpha}$ in equation 2.22 as $\partial \bar{v}_r / \partial \bar{\alpha} = -0.49 V_0 \bar{\alpha}^{-0.51}$, because the terminal velocity (V_0) of a single bubble has nothing to do with $\bar{\alpha}$, i.e., $\partial V_0 / \partial \bar{\alpha} = 0$. Then the last term in the RHS of equation 2.22 is reduced to the $c' \bar{v}_r$. Consequently, the final expression of the bubble-induced streamwise liquid fluctuation is:

$$v_{l,rms}'' = c_{1n} \bar{v}_r + c_{2n} \bar{\alpha}^{0.4} (1 + \bar{\alpha}^{0.49}) \bar{v}_r + c_{3n} \bar{d}_b \bar{\alpha}^{-1/3} \left[(1 + \bar{\alpha}^{0.49}) \left| \frac{\partial \bar{v}_r}{\partial x} \right| + \bar{v}_r \bar{\alpha}^{-0.51} \left| \frac{\partial \bar{\alpha}}{\partial x} \right| \right], \quad (2.35)$$

here, c_{1n} , c_{2n} , and c_{3n} are tuning prefactors to be optimized later. If we look at the proposed model carefully, the first term ($v_{l,rms}'' \cong \bar{v}_r$) in equation 2.24 which is coincided with the Nigmatulin (1979) model can be understood as the contribution by an inviscid flow. Because, in a dilute dispersion, Nigmatulin (1979) modeled the bubble-induced normal stresses by the integration of the liquid velocity induced by an inviscid (and incompressible) flow around a spherical particle without considering the complex wakes' interactions as $\overline{v_l'' v_l''} \cong c_{vm} \bar{v}_r^2$ where the virtual-mass coefficient (c_{vm}) is 0.5 when the volume void fraction is rather low. On the other hand, the second term ($\sim \langle \bar{\alpha} \rangle^{0.4}$) comes from the typical characteristics of the bubble-induced turbulence in a dynamic liquid. Although there exists a bulk liquid flow, the turbulent nature of the bubble-induced turbulence (e.g., PDFs of liquid velocity fluctuations and spectral analysis showing the k^3 subrange for wavelengths larger than $\langle \bar{d}_b \rangle$) is maintained to some extent even though it is surrounded by the external turbulent fluctuations (e.g., SIT), and also according to previous studies (Prakash et al. 2016; Alm eras et al. 2017; du Cluzeau et al. 2019; Lai & Socolofsky 2019). Meanwhile, as we intended, the last term ($\sim l_b \cdot |\partial \bar{v}_l / \partial x|$) comes from turbulence modification by the redistributed bubbles ($\nabla \bar{\alpha} \neq 0$) by the bluff body or sidewalls, which is now reproduced as $\partial \bar{v}_r / \partial x$ and $\partial \bar{\alpha} / \partial x$, but the mixing-length (l_b) is corrected to have void-dependency under an imposed liquid-shear (figure 2.2). For an unbounded homogeneous bubble-swarm ($\nabla \bar{\alpha} = 0$) in quiescent water, the last term has necessarily vanished.

If equation 2.24 is mathematically squared, the diagonal-component of a bubble-induced stress tensor ($\rho_l \overline{v_l'' v_l''}$) in the main flow direction can be modeled explicitly. However, most of the prior experiments we found only provide the data on root-mean-square of v_l'' rather than $\rho_l \overline{v_l'' v_l''}$, thus to validate the equation 2.24, we use the equation as it is. To the best of our knowledge, there are no studies that

explicitly model this quantity except Ma et al. (2020) where they modeled the normal stress (e.g., $\rho_l (\overline{v'_l v'_l} + \overline{v''_l v''_l})$) explicitly in all directions from the balance equation for the Reynolds stress (Ma et al. 2020). Although their approach is innovative, the model cannot be applied near the wall, and if there is inhomogeneity in the local void fraction at the pipe center, the accuracy is somewhat degraded, which is obviously a limitation of applicability.

Next, the way that we develop a prediction model for the turbulent (shear) stress ($-\rho_l \overline{v''_l u''_l}$) is basically similar to that of v''_l . In our original concept (equation 2.20), we linearly multiply the bubble-induced transverse liquid fluctuation as $-v''_l u''_l \cong (V_0 \langle \bar{\alpha} \rangle^{0.4} + \Delta v''_l) \cdot u''_l$, here we again judge that the cross-correlation between the terminal velocity of a single bubble (V_0) and u''_l is negligible and has nothing related to the turbulent stress. Our main concern then reduces to formulate $\Delta v''_l u''_l$ which equals to $l_b (\partial \bar{v}_l / \partial x) \cdot u''_l$. On the other hand, we adopt an inviscid model for u''_l by Milne-Thomson (1996):

$$u''_l|_{\eta^*} \sim \begin{cases} \langle \bar{v}_r \rangle & (|\eta^*| < 1.0). \\ \langle \bar{v}_r \rangle / \eta^{*2} & (|\eta^*| \geq 1.0). \end{cases} \quad (2.36)$$

Compared to equation 2.25, under dynamic liquid conditions, the more important factor is how quickly the bubble rises relative to the background liquid flow ($\langle \bar{v}_r \rangle$) than the absolute velocity of the bubble ($\langle \bar{v}_b \rangle$). The theoretical justification for this choice is already provided in section 2.3.1. Then, the Reynold shear stress in an imposed external pressure gradient can be analytically expressed as:

$$-\overline{v''_l u''_l} = \frac{1}{T} \int_0^T \int_0^{l_m / \langle \bar{d}_b \rangle} -v''_l|_{\eta^*} u''_l|_{\eta^*} \alpha(\eta^*) d\eta^* dt. \quad (2.37)$$

The upper-bar denotes the time-averaged quantity. When neighboring bubbles pass temporarily at a distance η^* from the control plane (figure 2.2), they instantaneously agitate the liquid flow at $\eta^* = 0$. Likewise, bubbles can be located anywhere within $0 \leq \eta^* \leq l_m / \langle \bar{d}_b \rangle$, and they collectively affect the liquid fluctuation at the target plane ($\eta^* = 0$). Conversely, the absence of neighboring

bubbles at η^* ($\alpha(\eta^*) = 0$) does not alter the liquid flow at the control plane. Substituting the proposed submodels into equation 2.36 leads to the following equations:

$$\begin{aligned}
-\overline{v_l'' u_l''} &\cong \overline{\alpha} V_0 \langle \overline{\alpha} \rangle^{0.4} \langle \overline{v_b} \rangle \left[\int_0^{l_m/\langle \overline{d_b} \rangle} \frac{1}{\eta^{*2}} d\eta^* + 2 \right] \\
&+ \overline{\alpha} \left[\overline{d_b} \overline{\alpha}^{-1/3} - 2 \overline{v_r} \left(\frac{\partial \overline{v_r}}{\partial x} \right)^{-1} \right] \langle \overline{v_r} \rangle \left((1 + \overline{\alpha}^{0.49}) \frac{\partial \overline{v_r}}{\partial x} + \overline{v_r} \overline{\alpha}^{-0.51} \frac{\partial \overline{\alpha}}{\partial x} \right) \\
&\times \left[\int_0^1 f d\eta^* + \int_1^{l_m/\langle \overline{d_b} \rangle} \frac{f}{\eta^{*2}} d\eta^* \right].
\end{aligned} \quad (2.38)$$

The integral terms in parentheses can be treated as an empirical constant, and we can rearrange the equation 2.38 as follows:

$$\begin{aligned}
-\overline{v_l'' u_l''} &= \overline{\alpha}^{-1/3} \left[c_{1r} \overline{d_b} \overline{v_r} \overline{\alpha} (1 + \overline{\alpha}^{0.49}) \frac{\partial \overline{v_r}}{\partial x} + c_{2r} \cdot \overline{d_b} \overline{v_r}^2 \overline{\alpha}^{0.49} \frac{\partial \overline{\alpha}}{\partial x} \right] \\
&+ c_{3r} \overline{\alpha} (1 + \overline{\alpha}^{0.49}) \overline{v_r}^2 + c_{4r} \overline{\alpha} (1 - \overline{\alpha}^{0.49}) \overline{v_r}^2,
\end{aligned} \quad (2.39)$$

here, c_{1r} , c_{2r} , c_{3r} , and c_{4r} are empirical prefactors to be optimized, and we replace the $\langle \overline{d_b} \rangle$, $\langle \overline{v_b} \rangle$ and $\langle \overline{\alpha} \rangle$ with $\overline{d_b}$, $\overline{v_b}$ and $\overline{\alpha}$, respectively (figures 2.4 and 2.5) to predict the spatially-varying turbulence quantities more precisely. Compared to the anti-symmetric nature of the bubble-induced turbulent stress, the third- and fourth-term in the RHS of equation 2.39 always exhibit a symmetric profile, which is irrelevant. Therefore, the optimal constants found by the least-square method for c_{3r} and c_{4r} respectively are zero. As a result, the final expression for the bubble-induced turbulent (shear) stress is as follows:

$$-\overline{v_l'' u_l''} = \overline{\alpha}^{-1/3} \left[c_{1r} \overline{d_b} \overline{v_r} \overline{\alpha} (1 + \overline{\alpha}^{0.49}) \frac{\partial \overline{v_r}}{\partial x} + c_{2r} \cdot \overline{d_b} \overline{v_r}^2 \overline{\alpha}^{0.49} \frac{\partial \overline{\alpha}}{\partial x} \right]. \quad (2.40)$$

Compared to our previous model for turbulent (shear) stress in a homogeneous bubble-swarm past a circular cylinder in quiescent water (equation 2.29), we do not break down the $\overline{v_r}$ into $\overline{v_b} - \overline{v_l}$, because $\overline{v_r}$ is more relevant velocity-scale to represent bubble dynamics in the presence of the background liquid flow, which is also held for the bubble-induced streamwise liquid fluctuation (equation 2.35). Turbulence modification by the redistributed bubbles ($\nabla \overline{\alpha} \neq 0$) by sidewalls is reproduced as $\partial \overline{v_r} / \partial x$ and $\partial \overline{\alpha} / \partial x$, and in a homogeneous bubble-swarm

($\nabla \bar{\alpha} = 0$) in quiescent water, this model becomes totally zero, which is consistent with experimental observations (Risso & Ellingsen 2002; Riboux et al. 2010).

Along with prior studies (Hosokawa & Tomiyama 2013; Kim et al. 2016; Ma et al. 2020), we keep arguing that gradients of additional flow variables other than the mean liquid velocity are necessary to faithfully reproduce the actual bubble-induced turbulence, especially in complex geometries because the role of turbulent and non-turbulent parts of the interaction between bubble wakes plays a major in characterizing the bubble-induced turbulence as the bubble Reynolds number (Re_r) and the volume void fraction increase. In this context, we believe that the proposed model (equations 2.35 and 2.40) effectively satisfies our intention.

Author	Symbol	$\langle \bar{\alpha} \rangle$ [%]	Re_D	D [mm]	Re_r	$\langle \bar{d}_b \rangle$ [mm]
Kim et al. (2016)	□	0.05 – 0.64	750	40	600 – 800	2.2 – 3.7
Hosokawa and Tomiyama (2013)	▽	0.18 – 1.27	900	20	655 – 1,009	2.62 – 3.48
Liu and Bankoff (1993)	○	0.2*	14,288	38	160 – 2,545	2.0 – 4.0
Shawkat et al. (2008)	◇	1.2 – 15.4*	136,000	200	992 – 1,339	3.0 – 4.8
Lee et al. (2021)	△	0 – 1.8	5,300	40	750 – 1,150	3.8 – 4.4
	▽	0 – 1.5	44,000	40	714 – 1,575	2.8 – 3.6

Table 2.1. Inlet conditions for the considered upward laminar-to-turbulent bubbly pipe flows. Here, we have exclusively selected experimental studies that provide time-averaged spatially-varying turbulence statistics. The superscript “*” denotes the estimated volume void fractions by integrating the local void fraction across the entire cross-section.

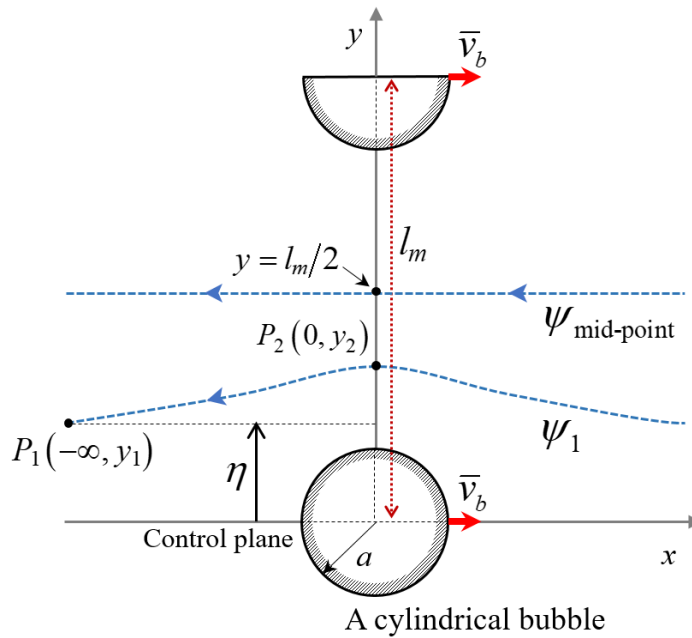


Figure 2.1. Schematic diagram of side-by-side cylindrical bubbles in an inviscid flow. The distance between the centroids of the bubbles is l_m , and two points P_1 and P_2 are located on the same streamline ($\psi = \psi_1$); \bar{v}_b is the rise velocity of bubbles in a quiescent liquid, and η is the distance from the control plane; Liquid drift-length ($y_2 - y_1$) is proportional to the two-phase mixing-length.

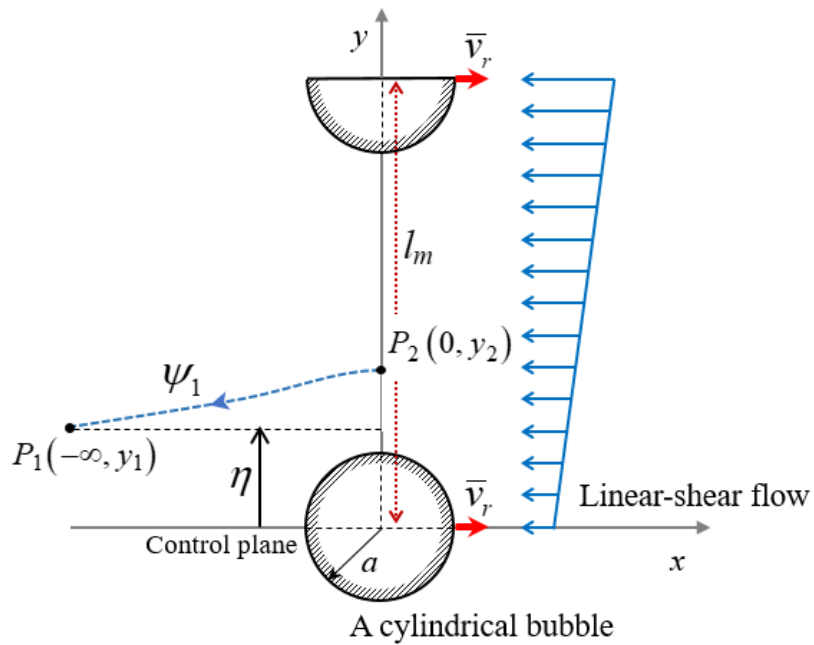


Figure 2.2. Schematic diagram of laminar-to-turbulent bubbly flows near the wall: evenly distributed side-by-side cylindrical bubbles rise with \bar{v}_r in an inviscid linear-shear flow. The parameters are the same as specified in figure 2.1.

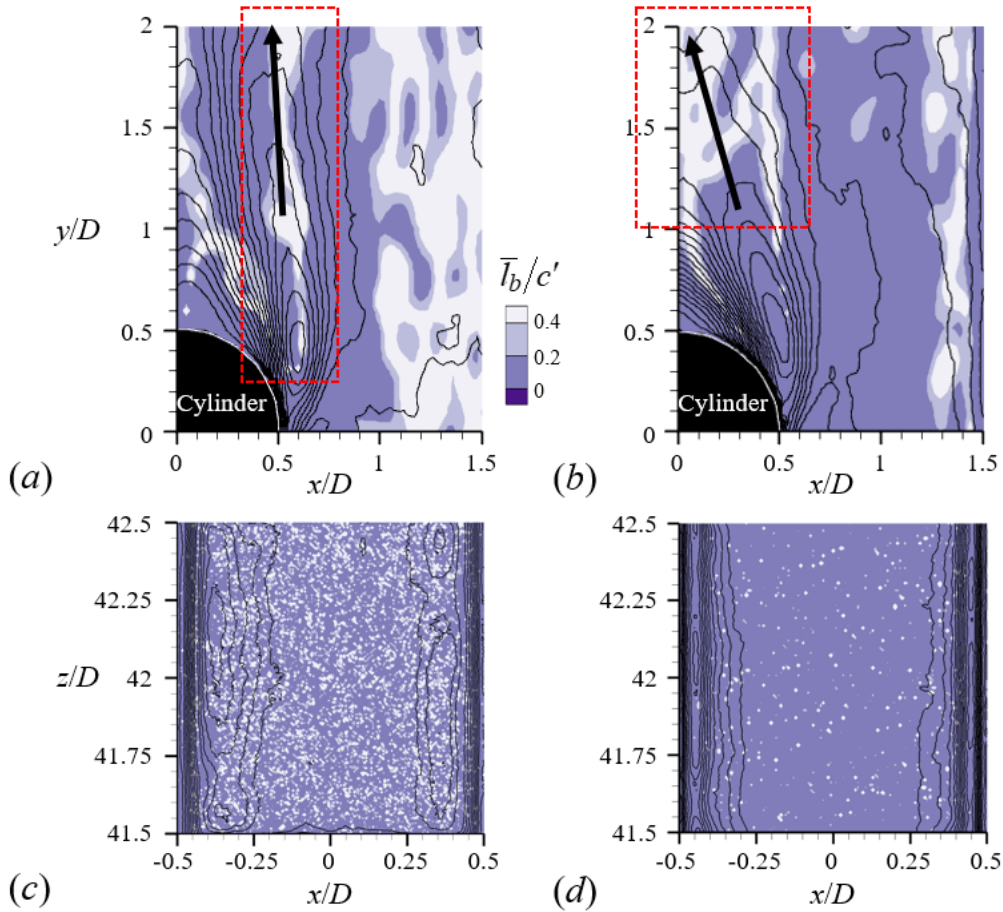


Figure 2.3. Signatures of the time-averaged two-phase mixing-length (flood) and mean void fraction (line): (a) a homogeneous bubble-swarm past a circular cylinder (D of 20 mm) in quiescent water at $\langle \bar{\alpha} \rangle$ of 0.6%; (b) 1.1%; (c) upward turbulent bubbly pipe flows (Reynolds number (Re_D , where D of 40 mm) is 5300) at $\langle \bar{\alpha} \rangle$ of 1.8%; (d) Re_D is 44000 at $\langle \bar{\alpha} \rangle$ of 1.5%. Here, the denser the line-contour, the more severe the change in the local void fraction.

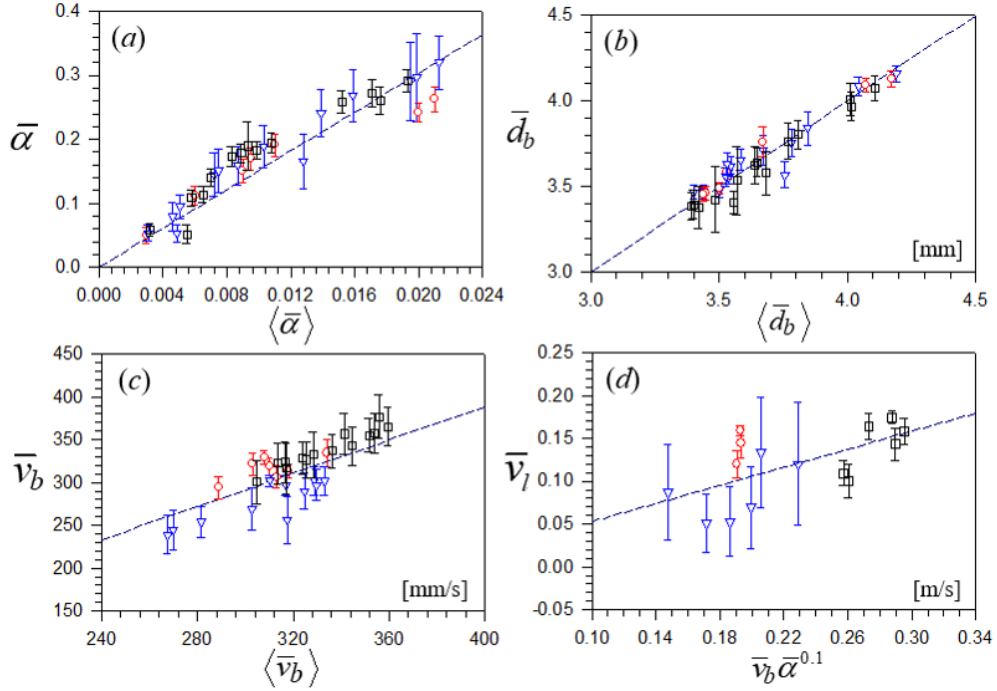


Figure 2.4. Linear relation between the local statistics with global values of (a) void fraction; (b) bubble size; (c) bubble rise velocity; (d) a scaling relation between the streamwise mean liquid velocity and gas-phase statistics; \circ , measured at upstream; ∇ , in the cylinder wake ($|x/D| \leq 0.5$, $y/D = 1$, where D of 20 mm); \square , outside of the wake ($|x/D| > 0.5$). For the purpose of visual comparison, a dashed-line in each figure is drawn to cross the origin.

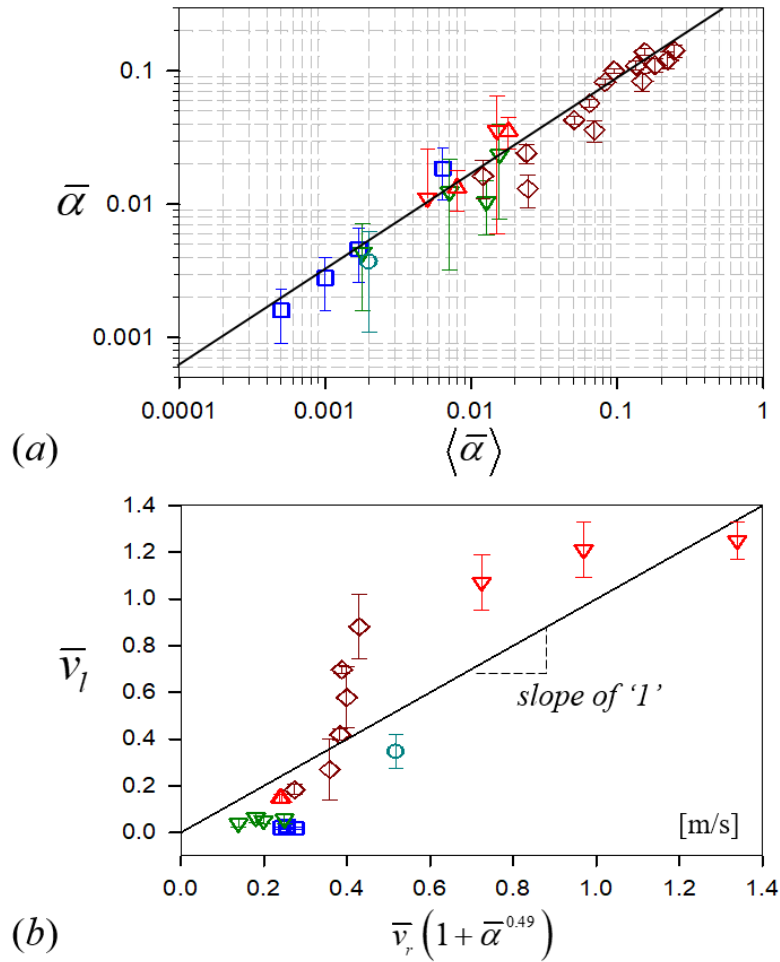


Figure 2.5. (a) Linear relation between the local statistics with global values of void fraction in bounded bubbly flows; (b) a scaling relation between the mean liquid velocity and gas-phase statistics in the presence of the background liquid flow. The symbol is the same as specified in table 2.1. For the purpose of visual comparison, a solid-line in each figure is drawn to cross the origin.

Chapter 3.

Experimental validation: a homogeneous bubble-swarm past a circular cylinder

3.1 Experimental setup and procedures

To validate the developed model for the bubble-induced streamwise liquid fluctuation (equation 2.24) and turbulent stress (equation 2.29), we have configured an unbounded gravity-driven homogeneous bubble-swarm at upstream of the circular cylinder where the turbulent nature of the pure bubble-induced turbulence dominates in the flow. When the bubble-induced mean liquid flow passes around a cylinder, the destabilization of the mean flow (and also an inhomogeneity in bubbles' distributions) induces turbulence modification of the existing BIT to some extent, and in this environment, turbulent stress which is absent at upstream also emerges and its origination would be associated with the deflected transverse distributions of the mean liquid-, relative-velocity in gas-phase and local void fraction. This we judge is a good example to discuss and validate the proposed models.

3.1.1 Flow facilities and robustness

The experimental setup includes an acrylic water tank ($670 \times 240 \times 1100$ mm³) with an acrylic circular cylinder installed, and a bubble generation system (a plenum chamber and sparger array) as shown in figure 3.1. The tank is filled with tap water (at room temperature) to a level 950 mm from the bottom, and the circular cylinder (diameter $D = 20$ mm or 30 mm, length $L = 240$ mm) is located 500 mm from the bottom wall where the bubbles are generated. The location of the circular cylinder was chosen such that the bubble-swarm flow develops sufficiently for the bubble distribution (and bubble-induced liquid velocity) to become uniform, which was confirmed by measurement. The aspect ratio of the circular cylinder is

$L/D = 12.0$ and 8.0 , respectively, which is sufficiently large to guarantee the two-dimensionality of the flow. There is no average liquid flow through the tank and thus the three-dimensional effect as a result of interference by the tank wall is not sufficiently strong to disturb the measurement at the midspan. The corresponding blockage ratio is less than 4.5% and no correction for the blockage effect is applied to the measured data (West & Apelt 1982). The contact angle (θ_c) of a water droplet on the acrylic cylinder surface is measured to be about 60° using a method based on B-spline snakes, meaning that the cylinder has properties close to hydrophilicity. We have investigated the bubble dynamics in the close vicinity of the cylinder by varying the surface properties of the cylinder, e.g., hydrophobicity (chapter 3.2). At the bottom of the tank, 55 spargers with $100\ \mu\text{m}$ pores (SM-02, SANG-A Pneumatic Co., Ltd.) are installed in a square arrangement (11×5 configuration and the distance between adjacent spargers is $55\ \text{mm}$) (figure 3.1) to introduce a homogeneous bubble swarm. The air pressure is varied through two successive regulators in the range $0\text{--}0.4\ \text{MPa}$, to control the flow rate, i.e., the void fraction. As a result, the volume void fraction (measured upstream of the circular cylinder) is varied from 0.3% to 2.1% and the average bubble diameter is $3.7 \pm 0.3\ \text{mm}$. To regulate the inlet bubble condition more precisely, the airflow into each sparger is controlled independently by using a set of in-line regulators and solenoid valves. Thus, the bubble generation ensures the generation of a uniform bubble swarm with a weak large-scale liquid recirculation that moves upward at the core-region of the vessel while downward near the sidewalls.

3.1.2 Two-phase particle-image velocimetry (PIV)

It is important to measure the gas and liquid phases simultaneously to understand their interactions around the bluff body. To achieve this, we consider a two-phase high-speed particle image velocimetry (PIV/LIF) with shadowgraph imaging that consists of a high-speed camera and two illuminations with different wavelengths as schematically shown in figure 3.2 (Lindken & Merzkirch 2002; Bröder & Sommerfeld 2007; Sathe et al. 2010; Kim et al. 2016). As has been proved in previous studies, the advantage of this method is to capture the temporal

variations of the two-phase instantaneous flow fields (i.e., visualization) for both phases and the spatial variations of time-averaged gas- and liquid-phase statistics. To briefly explain the method, a high-speed camera (MotionPro NX5-S2, IDT vision) captures images of both gas- and liquid-phase at 1000 Hz with a resolution of 1680×1088 pixels, illuminated by two light sources. With the present setup, the depth of field (DoF) is calculated as $\text{DoF} = sf^2/[f^2 - Nc(s-f) - sf^2/[f^2 + Nc(s-f)]] = 8.0$ mm, which is approximately twice the average bubble diameter (table 3.1). Here, the distance between the lens and measurement plane is $s = 800$ mm, $N = 1.8$, focal length $f = 67$ mm, and the circle of confusion is $c = 0.017$ mm. For gas-phase, continuous plane LED (red-colored, wavelength of 675 nm) is used to produce shadowgraph images of bubbles while a green laser sheet (wavelength of 532 nm) from a 5W diode-pumped solid-state (DPSS) continuous (CW) laser (RayPower 5000, Dantec Dynamics) illuminates the seeders that follow the liquid flow (figure 3.2). For the seeding particles, we use fluorescent particles (PMMA Rhodamine-B type, size ranging 1-20 μm) that reduce the diffused reflection of laser sheets on the bubble interfaces. At the opposite side of the laser, a mirror with a high reflective index is placed to minimize the blocking due to the shadows of rising bubbles. Using the in-house calibration target, it makes sure that the incident and reflected laser sheets match the same line. To utilize the different wavelengths from two light sources, the high-speed camera is equipped with an orange filter (cut-off wavelength of 570 nm) so that the fluorescence of tracking particles (dominantly 576 nm, in water) is transmitted with the LED light (675 nm) while blocking the CW laser (532 nm) and any associated reflections on the bubble surfaces. Figure 3.3(a) shows a representative raw image that has been obtained from the present setup and it is clear that the bubble shadows, seeding particles, and background have all different gray-scale levels that can be readily distinguished with image processing.

From a raw image (figure 3.3a), basically, two gray-scale intensity fields representing gas- and liquid-phase can be obtained (Bröder & Sommerfeld 2007; Sathe et al. 2010; Kim et al. 2016). The image for the seeding particle is further evaluated to measure the liquid velocity by cross-correlation using the fast-Fourier-transform algorithm (with an interrogation window of 32×32 pixels, 75% overlap).

When the outliers whose magnitudes are larger than three times the standard deviation of spatially-averaged velocities are detected, they are replaced by vectors that are interpolated from the neighboring velocity vectors within 3×3 grids. Thus, in the resulting liquid-phase velocity fields, the spatial resolution is about 0.6 mm ($\sim 0.029D$ or $0.15d_b$). On the other hand, the bubble velocity (trajectory) is determined by calculating the traveled distance of individual bubble centroids using a typical particle tracking velocimetry (PTV) algorithm that matches the closest neighbor bubble in the estimated direction of bubble motion (Bröder & Sommerfeld 2007). In the measurement plane, the centroids of each bubble are calculated from the planar projection areas on the image, and the calculation of its equivalent diameter and shape are discussed later. The actual measurements are carried out at two streamwise (upstream and downstream of the circular cylinder) locations (both on the mid-span plane). The field of view (FoV) has a size of $90 \times 70 \text{ mm}^2$ ($-2.25 \leq x/D \leq 2.25$ and $-4.0 \leq y/D \leq -0.5$, for $D = 20 \text{ mm}$) for upstream and $80 \times 120 \text{ mm}^2$ ($-2.0 \leq x/D \leq 2.0$ and $-1.0 \leq y/D \leq 5.0$) for near wake, with the origin at the center of circular cylinder. For larger $D = 30 \text{ mm}$, measurement locations and pixel resolutions are retained while the spatial resolution is slightly reduced to $0.024D$ ($\sim 0.18d_b$). The location of the upstream measurement is 430 mm ($\sim 108d_b$) above the sparger-array, where the terminal velocity of the rising bubble has been achieved (Clift et al. 1978). For each case, more than 60,000 instantaneous velocity fields were obtained to obtain fully converged time-averaged statistics for gas- and liquid-phases.

3.1.3 Phase discrimination

Digital image processing is carried out based on the fact that the gray-scale levels corresponding to bubble shadow, tracking particles, and background are different. Figure 3.3 shows the typical images corresponding to each step in the considered image post-processing procedure (Kim et al. 2016, Lee & Park 2020). To extract bubbles, a median filter (7×7 pixels, sufficiently larger than the tracer particle) is first applied to the raw image (figure 3.3a), whose response is based on the ordering (ranking) of the pixels contained in the 7×7 neighborhood image and

then replacing the center pixel value with that at the 50th percentile in the ordered set. Thus tracking particles are regarded as noise and are removed (figure 3.3b) from the raw image. The median-filtered image is binarized with a threshold determined by a global thresholding algorithm (Otsu 1979), which automatically finds the optimal global threshold that maximizes the between-class variance from the image histogram. After that, 3-pixel-wide borders along the bubble perimeter are eliminated to compensate for blur and reflections (i.e., over-estimated bubble size) on the bubble surfaces (figure 3.3c) (Lindken & Merzkirch 2002; Sathe et al. 2010).

To accurately measure the gas-phase statistics, it is important to reliably separate the overlapped bubbles into solitary bubbles, and we use a watershed transform algorithm, a region-based segmentation method using distance transformation (Gonzalez et al. 2011). As shown in figure 3.3(b), overlapped bubbles have a kind of internal and external markers; that is, the internal markers are brighter regions (called minima) inside of the bubbles, and the external markers are the midway between internal markers. We use both markers to process the median-filtered image so that the regional minima appear only in the marked locations (Gonzalez et al. 2011). Besides, we apply the shape factor algorithm to prevent non-overlapped bubbles from being divided (Lau et al. 2013). For each bubble in the binarized image (figure 3.3c), the overlapped bubbles are selected out by calculating the shape factor (Ro), defined as the ratio of projected perimeter to the inner areas of a bubble, indicating that the Ro will be larger if more bubbles are overlapped. As a result, non-overlapped bubbles (figure 3.3d) are labeled as solitary bubbles, whereas the remaining overlapped bubbles (figure 3.3e) are further processed with watershed transformation (figure 3.3f). We iteratively applied the series of shape factor and watershed transformation algorithms (with a stiffer threshold) (figure 3.3f). These iterations are repeated 2-3 times and bubble segmentations resulting from the last loop are finally combined with the non-overlapped bubbles to complete the gas-phase information (figure 3.3g). All bubbles in figure 3.3(g) include both in-focused and out-of-focused ones, and thus it is necessary to distinguish them. Using the fact that in-focus bubbles have higher gradients in the gray-scale level at the interface between gas and liquid, a Sobel

filter is finally applied to extract the bubbles captured on the measurement plane by calculating the discrete differences within a 3×3 neighborhood (figure 3.3*h*).

For the liquid-phase, we apply the Laplacian of Gaussian (LoG) filter to the raw image by which both bubbles and tracking particles are emphasized but the background illumination is suppressed (figure 3.3*i*) (Bröder & Sommerfeld 2007; Pang & Wei 2013; Kim et al. 2016). This procedure smoothens the image (thus, reducing noise). By sharpening the image again, regions with a sharp gray-scale contrast are highlighted whereas those with nearly constant gray levels are suppressed to zero. To evaluate bubble-induced liquid velocity with the PIV algorithm, only the seeding particle images are required and the outer boundaries of bubbles must be removed from figure 3.3(*i*). Thus, a median filter is applied to the LoG-filtered image to extract bubble boundaries (figure 3.3*j*). As a result, the final liquid-phase image (e.g. image of tracking particles only) is acquired by subtracting the bubble boundaries image from the LoG-filtered image (figure 3.3*k*).

Through each image-processing step, we confirmed that the footprints of bubble edges do not remain to distort the liquid-phase velocity. More specifically, we have evaluated the upstream liquid-phase velocity fields for the case of $\langle \bar{\alpha} \rangle = 0.006$ case, obtained with (and without) the successive steps introduced above. To quantitatively compare the variations in local liquid velocity (especially in the vicinity of bubbles) per each step, we have visualized the calculated liquid velocity fields and corresponding image inputs as shown in figure 3.4. In the raw image, the trace of rising bubbles (reminiscent of incomplete image process) are evident but the gray-scale intensity of seeding particles is too low to further be processed into the PIV algorithm (figure 3.4*a*). Therefore, many spurious liquid vectors (especially near bubbles) are shown (figure 3.4*d*). This is because the average number of tracking particles per interrogation window is less than 8 in the vicinity of bubbles (Adrian & Westerweel 2001). In addition, the gray-scale intensity of an interrogation grid is also included in the PIV calculation, where abrupt intensity variations near the bubble boundaries contribute to causing spurious vectors. On the other hand, the PIV measurement based on the LoG filtered image does not make much difference: both the number and magnitude of the spurious vectors increased (figure 3.4*e*) because the edges of the bubbles are also significantly

highlighted due to the contrast effect (red arrows) of the applied filter (figure 3.4b). However, it is observed that the spurious vectors tend to be confined inside the bubble regions. We have successfully detected the seeding particles existing over the bubbles (orange color) located behind the $z/D = 0$ plane, thus liquid velocity in this region is more or less uniform and consistent compared to the surrounding vectors. Lastly, the PIV results based on the final image without traces of bubble (figure 3.4c) do not have noticeable error vectors both inside and outside the bubbles (figure 3.4f). In median filtering, the gray value of each pixel (e.g., tracking particles) is replaced (removed) by the middle gray value of its 5×5 neighborhood by arranging the set in increasing (decreasing) order. As a result, traces of rising bubbles (highlighted with red arrows) are successfully eliminated by subtracting the median filtered images from the LoG images (Bröder & Sommerfeld 2007). Furthermore, when we calculate the vorticity in liquid-phase, we use a weighted-linear interpolation by referring to neighboring instantaneous liquid vectors to fill the artificial liquid velocities inside the bubbles located in front of the focal-plane to prevent the abrupt vorticity jump at the phase boundaries (figure 3.5). This is reasonable because the fluid medium is innately continuum. Thus, the closer the vectors are located to the targeted interrogation window, the more weight is given.

3.1.4 Uncertainties in the measurements

For typical particle image velocimetry measurements, the velocity vector (u_p) in space can be obtained through a magnification factor (M), the time difference (Δt) between two consecutive particle images, particle displacement (Δs), as $u_p = M\Delta s/\Delta t$. Therefore, any sources of uncertainties in acquiring those values can affect the total percentage error $\delta(u_p)$, shown in the relation below (Lawson et al. 1999):

$$\delta(u_p) = \sqrt{\delta(M)^2 + \delta(\Delta s)^2 + \delta(\Delta t)^2} \quad (3.1)$$

The uncertainty in magnification factor, $\delta(M)$, is estimated from a raw image of calibration target placed in the laser sheet (thickness ~ 2 mm) prior to each set of PIV measurement, where the errors are calculated to be 1.72-1.83% with M of 71.9 $\mu\text{m}/\text{pixel}$ and 89.3 $\mu\text{m}/\text{pixel}$ for the cylinder diameter $D = 20$ and 30 mm,

respectively. For the time separation, $\delta(\Delta t)$, the high-speed camera operating in its inter-frame time (or exposure time) of 1,000 ns provides an error of 0.1% (the actual time difference between two consecutive images is 1 ms). Lastly, the pixel resolution that universally affects the particle displacement is 0.1 pixel, and thus $\delta(\Delta s)$ is estimated as 1.81% and 2.67% for $D = 20$ mm and 30 mm, respectively. Therefore, the overall uncertainty in the present velocity measurement is calculated to be 2.5-3.2%.

In detecting individual bubbles from a planar projection shadow image (the detailed procedure is explained in section 3.1.3), it is possible that the equivalent bubble size, aspect ratio, and void fraction varies depending on the choice of global threshold during an image binarization (figure 3.3c). We have checked that by varying image thresholds, their values deviate with the range of 3.6%, 2.1%, and 5.0%, respectively. On the other hand, the displacement of a bubble is measured by matching the closest neighbor bubble in the estimated direction of bubble motion and is maintained about one-fourth of the d_b , because the diameters of a considered bubble on the two successive images should not differ more than 5%, as recommended by Bröder & Sommerfeld (2007). Thus, the uncertainty in measuring the bubble velocity is about 15.1 mm/s, which is 3.9% of the mean streamwise bubble velocity, considered in the present study.

3.1.5 Characterization of the considered gas-phase

To consider different conditions of the gas phase, we vary the inlet volume void fraction (defined as the ratio of the total volume occupied by in-focused and out-of-focus bubbles to the volume of the FoV) as $\langle \bar{\alpha} \rangle = 0.003, 0.006, 0.009, 0.0095, 0.011, 0.02, \text{ and } 0.021$ (see Table 3.1 for the details). In this paper, we use the subscripts “ b ” and “ l ” to denote bubble and liquid, respectively, and the subscript “ ∞ ” denotes the variable measured at the upstream. If not specified otherwise, then the velocities are absolute values measured in the laboratory frame and subscript “ r ” is used to denote the relative quantity. The bubble size (d_b) is determined by calculating the volume-equivalent bubble diameter of a spheroid as

$d_b = (d_{\max}^2 d_{\min})^{1/3}$, where d_{\max} and d_{\min} are the lengths of the major and minor axes of the assumed ellipsoidal cross-section, respectively (Bröder & Sommerfeld 2007; Jeong & Park 2015, Lee & Park 2017). Inlet conditions of the gas-phase are summarized in table 3.1. As upstream volume void fraction increases, the mean bubble diameter ($\langle \bar{d}_{b\infty} \rangle$) slightly increases from 3.4 mm to 4.2 mm while its terminal velocity ($\langle \bar{v}_{b\infty} \rangle$) decreases from 334 mm/s to 289 mm/s due to enhanced bubble interactions. The average bubble aspect ratio ($\beta = d_{\max}/d_{\min}$) is the same for all cases. The important dimensionless parameters for the present bubble are Reynolds number, $Re_b = \rho_l \langle \bar{v}_{b\infty} \rangle \langle \bar{d}_{b\infty} \rangle \mu_l^{-1}$, Eötvös number, $EO = g(\rho_l - \rho_g) \langle \bar{d}_{b\infty} \rangle^2 \sigma^{-1}$, Weber number, $We = \rho_l \langle \bar{v}_{b\infty} \rangle^2 \langle \bar{d}_{b\infty} \rangle \sigma^{-1}$, and Morton number, $Mo = g \mu_l^4 (\rho_l - \rho_g) (\rho_l^2 \sigma^3)^{-1}$. As classified by Re_b and EO , the present bubbles have wobbling shapes (Clift et al. 1978) that have been approximated as an oblate ellipsoidal (Jeong & Park 2015, Lee & Park 2017), and will have a path instability, as well (Ellingsen & Risso 2001; Mougín & Magnaudet 2006; Zenit & Magnaudet 2008; Ern et al. 2012). Figure 3.6(a) shows the probability density function (PDF) of equivalent bubble diameter (d_b) in the upstream, averaged from 6×10^4 instantaneous flow fields. As shown, the measured PDFs slightly deviate from the Gaussian distribution for all the volume void fractions considered, skewness of which is scattered in the range 0.17-0.51 without a specific trend. Similarly, the skewness of PDFs of streamwise bubble velocity (figure 3.6b) is non-zero rather it is gradually changed from 0.52 to -0.22, i.e., the distribution shifts to the right as the volume void fraction increases. But it is interesting to note that bubbles are accelerated more rather than velocity fall with increasing $\langle \bar{\alpha} \rangle$, thus bubble coalescence occurs more frequently in the present study. As we have explained above, it is possible to precisely control the air flow through each sparger to introduce a homogeneous bubble swarm, which is confirmed by the fact that the local void fraction (figure 3.6c) and streamwise bubble velocity (figure 3.6d) upstream of the circular cylinder show a uniform distribution along the horizontal direction.

On the other hand, in the air-water two-phase flow where the effect of the surface tension is relatively high, the addition of surfactants (e.g. bubble interface contamination) has a great influence on the hydrodynamics (e.g. the rise velocity and path) of bubbles, known as Marangoni effect (Clift et al. 1978; Magnaudet & Eames 2000; Takagi & Matsumoto 2010). In other words, the immobilized bubble surface by local contaminations would result in drag enhancement, thus we think that the effect of surface contamination can be indirectly examined by the bubble's rise velocity since the surrounding (tap) water is initially at static condition. We compared the measured terminal velocity of the present bubbles with that derived empirically by Clift et al. (1978) and confirmed that the bubbles in the present study are close to the condition of a clean bubble rather than a fully contaminated one. Therefore, no special correction was considered further (but the tap water was replaced for each individual measurement set).

3.2 Gas-phase statistics in the cylinder wake

The typical local void distribution in the wake behind a circular cylinder (measured at $y/D = 1.5$) is shown in figure 3.7, for the case of $D = 20$ mm and $\langle \bar{\alpha} \rangle = 0.006$. Here, the superscript “*” denotes the normalization by the global upstream value, and the time-averaged local void fraction, $\bar{\alpha}(x)$, is defined as the portion of bubble areas that exist on the two-dimensional measurement plane ($z/D = 0$). Figure 3.7 compares the local void distributions obtained by considering all the (in- and out-of-focus) bubbles, and they are almost the same. This comparison was repeated for other spanwise locations of $z/D = 1.5, 3.0,$ and 4.5 (the chamber wall is $6D$ apart from the $z/D = 0$ plane). As shown, the local void distribution exhibits a similar trend along the spanwise direction. Thus, the measurement on the center-plane represents the actual flow, and we discuss the results based thereupon.

Figures 3.8 and 3.9 show the contours of time-averaged void distribution ($\bar{\alpha}^* = \bar{\alpha} / \langle \bar{\alpha} \rangle$) in the wake behind the circular cylinder of $D = 20$ mm and 30 mm, respectively, with $\langle \bar{\alpha} \rangle = 0.003$ - 0.021 . In general, the rising bubbles collide in the front stagnation region of the cylinder, remain there for some time while bouncing

several times, and then eventually slide along and separate from the cylinder surface. Thus, a region with a locally higher void fraction is established along these bubble trajectories. These typical behaviors of incident bubbles are also confirmed by the previous experiment (Joo & Dhir 1994) and simulation (Sugiyama et al. 2001) as shown in figure 3.10. Based on the variations in $\bar{\alpha}$, it is possible to classify two flow regimes: regime I in which two layers of higher $\bar{\alpha}$ develop along with the location of separating shear layers ($|x/D|=0.5-0.7$), and regime II in which the bubbles tend to concentrate behind the cylinder base ($x/D=0$) as the layers of higher $\bar{\alpha}$ are deflected toward the centerline as the flow develops. For $D=20$ mm ($\langle \bar{d}_b \rangle / D = 0.2$), the transition from regime I to II occurs at $\langle \bar{\alpha} \rangle \cong 0.0095$ (figure 3.8). In regime I, a region of lower void fraction ($\bar{\alpha}^* < 1.0$) appears behind the cylinder ($-0.4 \leq x/D \leq 0.4$) and is sustained far downstream, but it is substantially reduced and disappears at $y/D \geq 2.0$ in regime II. At $y/D \geq 2.0$, a region with a higher bubble concentration ($\bar{\alpha}^* \geq 1.0$) appears; however, the void distribution rapidly becomes uniform because of enhanced mixing. These two regimes are clearly distinguishable from the streamwise profile of local void fraction in the cylinder wake: from the base of cylinder ($y/D=0.5$), $\bar{\alpha}^*$ slowly increases and saturates downstream in regime I; however, it increases sharply to the maximum in the near wake and gradually decreases to a saturated value in regime II. The same trend is observed as the diameter of the cylinder increases to $D=30$ mm (figure 3.9). However, the area of higher bubble concentration is reduced and the uniform void distribution is recovered farther downstream. This is because the effective bubble size ($\langle \bar{d}_b \rangle / D = 0.13$) is reduced and the cylinder wake width has increased. Here, the transition between the two regimes occurs at $\langle \bar{\alpha} \rangle = 0.011$. Roughly speaking, the similar void distribution to that in regime II is found in previous studies (Joo & Dhir 1994; Sugiyama et al. 2001), but the details show quite a different trend due to the existence of background flow and a much higher void fraction (up to 25%) in those studies.

In figure 3.11, the transverse distribution of $\bar{\alpha}^*$ is plotted for the selected

cases. As the flow passes around the cylinder, the void fraction profile is deflected such that the maximum (minimum) peaks are behind the cylinder edge (base) (figures 3.11a and 3.11d). Because of enhanced bubble dispersion as a result of flow mixing, the magnitudes of peaks and valleys are saturated as the flow develops. For $D = 20$ mm (at $y/D = 1.5$), a minimum valley ($\bar{\alpha}^* \ll 1.0$) is observed at $x/D = 0$ and two distinctive peaks exist near a separating shear layer ($x/D = \pm 0.5$) for the cases of $\langle \bar{\alpha} \rangle = 0.003, 0.009$ and 0.011 , but a broad peak appears (without a valley) for $\langle \bar{\alpha} \rangle = 0.021$ (figure 3.11b). As the flow develops downstream (at $y/D = 2.5$), bubbles migrate toward the center of the cylinder and the case of $\langle \bar{\alpha} \rangle = 0.011$ also has a broad peak (transition to regime II) (figure 3.11c). As $\langle \bar{\alpha} \rangle$ increases in regime II, the two peaks merge increasingly faster, but this is not observed in regime I, even far downstream of $y/D \sim 10.0$. Beyond this, the bubbles disperse more or less uniformly, i.e., the effect of the circular cylinder disappears. In regime II, the shear-induced lift ($\vec{F}_L = -c_{L0}\rho_l(\vec{v}_b - \vec{v}_l) \times (\nabla \times \vec{v}_l)$) (Drew & Lahey 1987) increases drastically due to the intensified shear in the liquid flow ($y/D < 2.0$) and the added-mass (due to the gradient of x-component of relative bubble velocity) and pressure gradient forces also act in the same direction, resulting in a preferential concentration of bubbles behind the cylinder. In regime I, however, $|\vec{v}_l|$ and its gradient is smaller and thus the drag force ($\vec{F}_D = c_D\rho_l(3/4d_b)|\vec{v}_r|\vec{v}_r$) which is proportional to the square of the relative velocity of the bubble, becomes dominant (more than two times larger than regime I) to counteract the migration of the bubbles toward the center. For D of 30 mm, two local maximum peaks are still observable for $\langle \bar{\alpha} \rangle = 0.021$ at $y/D = 1.5$ (figure 3.11e), and a single broad peak forms farther downstream of $y/D \geq 2.5$ (figure 3.11f). This is because the dispersion of bubbles occurs relatively slowly due to smaller $\langle \bar{d}_b \rangle / D$. Furthermore, the magnitudes of local peaks are larger, as the interfacial forces (such as drag and lift force) increase with enhanced disturbance (i.e., steeper shear) by the cylinder.

The interfacial forces acting on the rising bubbles are strongly affected by their size (d_b) and aspect ratio (β) (Ishii & Zuber 1979; Hibiki & Ishii 2007; Adoua et al. 2009), whose transverse distributions in the cylinder wake are shown in figures 3.12 and 3.13, respectively. As shown in the figures, larger (smaller) bubbles (than the mean bubble size) are found at $x/D = \pm 0.5$ ($x/D = 0$), right behind the cylinder. Because the bubble-induced liquid flow evolves into a steeper velocity gradient (wake defect) behind the cylinder, smaller bubbles are attracted to the lower velocity region (i.e., toward $x/D = 0$) while larger bubbles accumulate behind the cylinder sides ($x/D \sim \pm 0.5$). As the flow develops the uniformity in bubble size distribution recovers rapidly, which is faster for the case of larger $\langle \bar{d}_b \rangle / D$ (smaller D) (figures 3.12c and 3.12f). Interestingly, the bubble size saturates faster than the void fraction. This is because the transverse migration of bubbles (i.e., the shear-induced lift force) is directly affected by the bubble size; however, the void distribution is determined by both the size and frequency of the bubbles.

In addition, the distribution of β can be understood in relation to void distribution (figure 3.13). The present bubble aspect ratio is in the range $\beta = 1.3$ -2.1. Along the transverse direction, the aspect ratio remains to be almost constant at $|x/D| > 0.5$ but decreases sharply toward the cylinder base (figures 3.13a and 3.13d). As the flow develops, the aspect ratio also shows a uniform distribution. Interestingly, unlike the void fraction and bubble size, the convergence of $\bar{\beta}$ occurs faster for the case of larger D (figures 3.13b and 3.13e). This is related to the dependency on β of the shear-induced lift force on a rising bubble. Previously, Adoua et al. (2009) simulated the flow around an oblate spheroidal bubble under different conditions and showed that the sign of the lift force changes with β for $Re = \mathcal{O}(10^2$ - $10^3)$, under a relatively weak shear rate. According to them, the bubble moves toward the higher liquid velocity region when $\beta \leq 2.2$ (lift force increases with increasing β), which is reversed at $\beta \geq 2.2$. For the present cases (the dimensionless shear-rate (≤ 0.2) is small and $Re_b = 1100$), the bubble aspect ratios are below 2.0, thus more deformed (i.e., higher β) bubbles would have a higher possibility to move out of the wake defect region which is, as a result, populated by

bubbles with a lower β . As the diameter of the cylinder increases, the velocity gradient behind the cylinder becomes steeper and is retained longer in the wake. Thus the contribution of the shear-induced lift force is stronger and causes the bubble aspect ratio distribution to converge faster.

Finally, the streamwise (\bar{v}_b) and transverse (\bar{u}_b) velocities of bubbles are compared in figures 3.14 and 3.15, respectively. The streamwise velocity has a minimum valley behind the cylinder, which gradually recovers the upstream value along the streamwise direction (figures 3.14c and 3.14f). The transverse velocity (below 40% of the rise velocity in maximum value) shows a skew-symmetric profile centered at the origin, and the peak values (at $|x/D| = 0.1-0.2$) decrease, and the corresponding locations are shifted away from the centerline with increasing $\langle \bar{\alpha} \rangle$ (figure 3.15). At $-0.5 < x/D < 0.5$, the bubble rise velocity increases but the transverse component decreases as the flow develops, which is associated with lateral movements of the bubbles promoted closer to the cylinder base (figures 3.15a and 3.15d), where the liquid-phase velocity gradient is steeper. The transverse velocity diminishes fast as the bubbles rise away from the cylinder (figures 3.15c and 3.15f). As the cylinder diameter increases, the overall trend of the bubble velocity distribution is not affected but the deviation between different $\langle \bar{\alpha} \rangle$'s is reduced. This is because the hydrodynamic influence of bubbles is reduced by the smaller $\langle \bar{d}_b \rangle / D$, and thus a larger increase in $\langle \bar{\alpha} \rangle$ is required to obtain a distinctive difference in the bubble velocity for a larger cylinder. However, it was shown that the mean bubble rise velocity and relative rise velocity is proportional to $\langle \bar{\alpha} \rangle^{-0.1}$ for a bubble-swarm in quiescent water ($0.005 \leq \langle \bar{\alpha} \rangle \leq 0.1$) (Riboux et al. 2010) and for an upward laminar bubbly pip flow ($0.0005 \leq \langle \bar{\alpha} \rangle \leq 0.0064$) (Kim et al. 2016), respectively. In the present cases, the scaling relation is satisfied to some extent in the upstream and downstream ($|x/D| > 0.5$) regions (figure 3.16a), but the existence of the circular cylinder slightly disturbs the local void fraction dependency at $|x/D| < 0.5$ in the downstream region. On the other hand, we have collected the data of time-averaged bubble rise velocity in a

bubble-swarm, which is similar to our configuration (figure 3.16*b*). For all the studies compared, the bubble Reynolds numbers based on the equivalent diameter are in the ranges of $\mathcal{O}(10^2-10^3)$. As shown, the existing data for the bubble rise velocity are scattered in a range such that it tends to decrease with increasing the volume void fraction, which is in line with the previous observations (Ellingsen & Risso 2001; Risso & Ellingsen 2002; Martínez-Mercado et al. 2007; Roig & de Tournemine 2007; Riboux et al. 2010; Kim et al. 2016; Risso 2018; Lee & Park 2020) and the present data are not different much from them.

Next, we have discussed how the behaviors of bubbles would be changed in the vicinity of the hydrophobic circular cylinder (D of 30 mm). First, we use a commercially available spray of hydrophobic nanoparticles (NeverWet-SE, NeverWet, LLC) with a mean size of ~ 20 nm to coat an acrylic (i.e., no-slip) circular cylinder. The increase in the diameter of the circular cylinder as a result of the coating is far less than $0.01D$, which has a negligible effect on the two-phase flows. To characterize the surfaces of acrylic and hydrophobic-coated circular cylinders that were considered, we measured the contact angle (θ_c) of a water droplet on each surface. When compared to smooth acrylic ($\theta_c = 60^\circ$, or hydrophilicity), the contact angle (θ_c) was measured at about 140° for the hydrophobic cylinder, which confirms its enhanced hydrophilicity (superhydrophobicity). The typical behaviors of bubbles in the hydrophilic (acrylic) cylinder proximity have already been discussed in figures 3.8 and 3.9, and these characteristics are also confirmed in figure 3.17*a*. When bubbles with similar characteristics (table 3.1) are injected against a hydrophobic circular cylinder, an interesting flow structure is developed: a part of bubbles sliding along the cylinder surface is separated early ($\theta_{sep} = 60^\circ$), exhibiting a local void peak there, while rest of bubbles maintain contact with the hydrophobic cylinder, reaching the rear stagnation point (figure 3.17*b*). Furthermore, near the rear stagnation point, bubbles as a form of thin gas-layer keep gathering from both sides of the cylinder and coalescence actively, which collectively results in a region of higher mean void fraction ($152^\circ < \theta < 180^\circ$). When bubbles grow enough to overcome the surface tension, they are individually detached from the cylinder and rise into downstream within $|x/D| < 0.5$ while intensively agitating the surrounding liquid (inset in figure

3.17*b*). To explain the difference in the behaviors of bubbles near the hydrophobic circular cylinder, we have measured the circumferential distributions of the mean bubble size and a void fraction (figures 3.18*a* and 3.18*b*). It is shown that, although we injected similar bubbles at upstream ($d_b \sim 3.4$ mm), the mean bubble size is significantly decreased along the hydrophobic cylinder surface. We suspect that, due to the hydrophobicity nature of the cylinder, bubbles sliding along the cylinder lose some of the gas to the grooves of the hydrophobic cylinder, which is also visualized in figure 3.17*c*, thus resulting in reduced bubble size and void fraction. Meanwhile, this characteristic is also related to the early separation point (θ_{sep}) of bubbles from the cylinder surface such that larger bubbles with an enhanced inertia can withstand an adverse pressure gradient at the hydrophilic cylinder surface (or skin friction) longer ($\theta_{sep} = 140^\circ$) (figure 3.17*a*) while it is not the case for the smaller bubbles at the hydrophobic cylinder ($\theta_{sep} = 60^\circ$), rather gas-phase as a form of thin gas-layer (which is expected to be an efficient geometry for a gas-solid contact) can migrate closer to the rear stagnation point. On the other hand, near the hydrophobic cylinder base, an order of the bubble size is increased (~ 10 mm) evolving into cap bubbles (figure 3.17*b*). Another plausible reason for the difference in the bubble behaviors especially at the hydrophobic cylinder is that vertically-oscillating attached bubbles ($\theta = 180^\circ$) can act as a kind of a deformed cylinder, thus modify the liquid-phase flow fields, and this in turn affects the bubble behaviors (e.g. trajectory, bubble-bubble interactions), however this hypotheses needs further considerations.

On the other hand, an interesting flow structure is induced in the wake behind the hydrophobic cylinder (figures 3.18*c* and 3.18*d*). Because sparsely-distributed large deformed bubbles depart from the rear stagnation point of the cylinder, a locally high mean void fraction region is induced along the bubbles' trajectories at downstream ($|x/D| < 0.5$), which is opposite to the case of the hydrophilic cylinder wake (figure 3.18*d*). Moreover, a broad upward convex profile at $|x/D| < 0.5$ is measured for the mean bubble size (figure 3.18*c*), which we have also discussed before. For the bubble-induced liquid-phase, it is expected that the recovery of the liquid-phase velocity-deficit would be much faster because large deformed bubbles agitate the surrounding liquid intensively (e.g., contributions by an averaged-wake

and detached-wake interaction) while giving momentum by buoyancy. However, since information on the bubble-induced liquid-phase flow fields is required for in-depth analysis, we do not proceed further. Nevertheless, we are able to confirm that a significant variation in the gas-liquid two-phase flow fields is occurred by simply changing the surface properties of the circular cylinder.

3.3 Bubble-induced liquid flow around a circular cylinder

3.3.1 Characterization of the upstream flow

In this section, we discuss the quantitative flow statistics for the liquid phase measured upstream. Based on our identification of two flow regimes (figure 3.7), we have confirmed whether the incident liquid flow is developed by a large-scale recirculation liquid motion (e.g., gross upward motion at the core-region of the vessel while downward near the wall-region). If it not, the mean liquid flow can be interpreted as a pure buoyancy-driven homogeneous bubble-swarm. To achieve this, we have operated the bubble-swarm (volume void fraction of 1.1%) for 20 minutes, which is sufficiently long enough to have a fully-developed liquid flow. As soon as the bubble generation is stopped (that is, as soon as the bubble leaves the measurement plane), we have processed PIV measurements behind the bubble-swarm. As shown in figure 3.19, we measured the velocity at the core region (where the circular cylinder is located) and the near-wall region right after the bubble-swarm had been stopped to decompose the measured liquid-phase velocity into contributions by the bubble-swarm and a global liquid-phase recirculation. Near the wall-region, a downward liquid motion with a maximum velocity of -0.08 m/s in the absence of bubbles is observed ($\sim 3D$ away from the sidewalls) which is a signature of the large-scale liquid circulation (figure 3.19d), meaning that a gross upward liquid flow with an averaged velocity of 0.009 m/s should be induced at the core-region of the vessel to keep the mass-conservation, and this is consistent with our measurements (0.011 m/s) (figure 3.19c). This upward liquid motion in the absence of bubbles can be interpreted as the contribution by the global liquid circulation and only accounts for the 8.3% of the measured mean liquid-phase

velocity in the middle of the bubble-swarm at upstream. In the core region, the intensity of the liquid fluctuations is higher at the upper region of the FoV, which is closer to the bottom of the preceding bubble swarm. On the other hand, the standard deviation of the transverse liquid velocity over the whole FoV (35.6 mm/s) is higher than that of the streamwise direction (28.5 mm/s), and descending liquid flows are also observed, intermittently. A downward liquid flow, on the other hand, is observed only in the narrow region along the sidewall ($\sim 3D$ away from the sidewalls) and it is then separated from the wall after the passage of the bubble swarm. Here, the intensity of the liquid fluctuation in the transverse direction is slightly suppressed due to the wall confinement effect (22.8 mm/s) while that of streamwise direction (36.7 mm/s) is slightly larger than the core region. Consequently, we did not notice an organized strong liquid-phase recirculating flows that accelerate the bubble (or liquid) in our measured data.

Based on this confirmation, we have proceeded to check the uniformity in liquid-phase just before the cylinder for the cases of $\langle \bar{\alpha} \rangle = 0.006$ and 0.011 for both $D = 20$ mm and 30 mm, representing regimes I and II, respectively. The time-averaged liquid velocity at the upstream ($y/D = -1.5$) location is shown in figure 3.20. Here, the velocities are non-dimensionalized by $\langle \bar{v}_{b\infty} \rangle$. As can be expected from the void distribution (figure 3.6), the upstream liquid-phase velocity is more or less uniform throughout the measurement area. As the inlet volume void fraction increases, the mean streamwise liquid velocity becomes faster (approximately $0.52 \langle \bar{v}_{b\infty} \rangle$) (figure 3.20a) due to the enhanced bubble-bubble interaction. The transverse velocity is almost negligible in a time-averaged sense (figure 3.20b). Although the transverse bubble velocity exists in instantaneous flows due to the axisymmetric oscillating path of an individual bubble, these flows are mitigated by the homogeneous bubble distribution.

As is well known, a substantial level of velocity fluctuation (so-called bubble-induced turbulence or agitation) is also induced by the present bubbles, which increases with increasing $\langle \bar{\alpha} \rangle$ (figure 3.20c). To investigate the turbulent nature of the bubble-agitated turbulent at upstream, we examine the probability density

functions (PDFs) of liquid-phase velocity measured at $-4.0 \leq y/D \leq -0.5$ with increasing volume void fractions (figure 3.21). The streamwise velocity fluctuation shows non-Gaussian behavior: the PDF is observed to exhibit positive skewness, due to the stronger entrainment of the liquid flow into the bubble wake (Risso & Ellingsen 2002; Riboux et al. 2010; Risso 2016, 2018). Moreover, the PDF tends to exhibit exponential decays (with a linear slope on the semilog-axes graph) (figure 3.21a). The transverse velocity fluctuation, however, shows a symmetric behavior with linear exponential tails, which does not change much with $\langle \bar{\alpha} \rangle$ (figure 3.21b). This is because the bubble-induced liquid flow in the vicinity of zigzagging bubbles is axisymmetric on average and the transverse void distribution is also statistically uniform. Previously, Riboux et al. (2010) showed that the root-mean-square of the liquid-phase velocity fluctuation is scaled with $\langle \bar{\alpha} \rangle^{0.4}$ in a homogeneous bubble-swarm, which was extended to the upward laminar bubbly flows (Kim et al. 2016). Under the present conditions, it is found that the spatially averaged streamwise velocity fluctuation is $v_{l,rms}'' / \langle \bar{v}_{b\infty} \rangle = 0.25$ and 0.33 , for $\langle \bar{\alpha} \rangle = 0.006$ and 0.011 , respectively, which is asymptotically scaled with $\langle \bar{\alpha} \rangle^{0.4}$ (figure 3.31). In the next section, we discuss whether this correlation remains valid for the wake region behind the cylinder. The turbulence intensity ($v_{l,rms}'' / \langle \bar{v}_{l\infty} \rangle$) of the upstream liquid-phase flow is calculated to be approximately 0.71 and 0.6 , for $\langle \bar{\alpha} \rangle = 0.006$ and 0.011 , respectively. Based on the PDF of the liquid-phase velocity fluctuation and scaling in relation to $\langle \bar{\alpha} \rangle$, we consider the bubble-induced agitation at the upstream region corresponds to that of a homogeneous swarm of rising bubbles (Risso 2016, 2018).

3.3.2 Bubble-induced flow in the cylinder wake

In this section, Representative instantaneous flow fields with velocity vectors (gas- and liquid-phase) and spanwise vorticities ($\omega_z^* = \bar{\omega}_z D / \langle \bar{v}_b \rangle$) are visualized at

upstream (figure 3.22). Here, the spanwise vorticity is normalized by the cylinder diameter (D) and the mean bubble rise velocity at upstream, and we highlighted bubbles that are located on and in front of a narrow focal-plane. For the present cases, bubbles mostly rise in two-dimensional zigzag paths (or sometimes take three-dimensional helical motions), which are expected from the dimensionless numbers (table 3.1). For $\langle \bar{\alpha} \rangle$ of 0.6% (figure 3.22a), the wake structures detached from the bubbles' surfaces last for a long duration (marked by filled-arrow) and increase the liquid fluctuations (and enhance TKE in liquid-phase) in the vicinity of them. Nonlinear interactions between detached wakes significantly account for the small-to-moderate liquid fluctuations in the PDFs of the v_t'' and u_t'' , and also solely contribute to the k^{-3} subrange in the wavelength larger the mean bubble diameter. On the other hand, steady spatial fluctuations (or an averaged-wake) are also observed just behind bubbles (opened-arrow), but they are disappeared while stationary (in time) attached behind the bubbles' rear surfaces. The remaining vortical structures and their interactions are known to be immediately dissipated while cascaded into smaller-scale. Interestingly, due to the initially quiescent liquid condition, the instantaneous liquid flows far away from rising bubbles (and their wakes) (solid-box) are almost at static. On the other hand, for $\langle \bar{\alpha} \rangle$ of 1.1% (figure 3.22b), the interactions between the bubble wakes are frequently occurred (dashed-box), generating enhanced liquid perturbations there. The drifted-flow in the close bubble proximities, which is known to generate the most significant liquid fluctuations, is observed in front of bubbles. Especially, because there are more bubbles, more chances for complicated interactions between detached wakes to occur present, resulting in the increased instantaneous liquid velocities and TKE in the liquid-phase. This has visualized that this is evident (dashed-box). However, liquid velocities between the bubbles (or between the bubbles and detached vortical structures) are still relatively small. Interestingly, the downward liquid motion is observed where there are fewer bubbles, which is meaningful in that a strong innate gross recirculating liquid motion does not exist.

Now we look into how the instantaneous two-phase flow fields at upstream (figure 3.22) are modified by the existence of the circular cylinder in downstream

for each regime ($\langle \bar{\alpha} \rangle = 0.006$ and 0.011) in the cylinder wake ($-1.0 \leq y/D \leq 4.0$) (figure 3.23). First of all, even downstream of the circular cylinder, most of the bubbles were observed to rise in a two-dimensional plane by tracking the center positions of each bubble. For regime I ($\langle \bar{\alpha} \rangle = 0.006$), bubbles are hardly observed in the near-wake region ($y/D < 2.0$), thus bubble-induced liquid flow is relatively weak there (figure 3.23a). Because the rising bubbles induce spatially nonuniform flow instantaneously, the organized evolution of a separating shear layer behind the cylinder is not clearly observed. As the flow continues to develop, the uniform distribution of the bubbles is restored. Similar to the upstream flow, the individual bubble wake structure is sustained for a certain period. As $\langle \bar{\alpha} \rangle$ increases to 0.011 (regime II), the near wake has a greater population of bubbles, inducing an enhanced shear flow (with intensive turbulence, as well) behind the cylinder edge (figure 3.23b). This strong shear in turn forces the trajectories of rising bubbles to deflect toward the center of the cylinder. It is also noted that bubble-induced flow structures become complex as the interaction between the bubble-wakes occurs more frequently. Although the overall difference between the two regimes is maintained for the larger cylinder diameter, the enlarged wake width appears to affect the two-phase flow pattern (figure 3.24). For example, at $\langle \bar{\alpha} \rangle = 0.006$, more bubbles are entrained and rise along with the separating shear layer, which would perturb the liquid-phase flow more frequently (figure 3.24a). As shown in figures 3.11(d)-(f), the rising bubbles disperse slowly and thus the higher concentration along the shear layer is sustained longer in downstream. With $\langle \bar{\alpha} \rangle = 0.011$, the entrainment of the bubbles into the near wake region also becomes more vigorous, but the relative size of bubble-induced vortical structures compared to the cylinder size (D) is reduced (figure 3.24b).

More specifically, we have investigated behaviors of the bubble-agitated structures in the close vicinity of the cylinder, here it is worth noting that, due to the absence of the background (bulk) liquid flow, an organized periodic liquid shear separating from the cylinder surface does not exist in the present study, rather it is generated randomly together with the instantaneous secondary vortex nearby

(figure 3.25). For example, when an individual bubble rises near the cylinder surface, the accumulated vorticity ($\omega_z^* = \omega_z D / \langle \bar{v}_b \rangle$) on a bubble surface sheds into pairs of counter-rotating vortices, extending within $2-3d_b$ (attached vortex chain). Later this initially attached vortex chain is detached from the bubble surface and sustained for a comparatively long time along the cylinder surface (highlighted as an arrow). The remaining counter-rotating vortices are elongated toward downstream over time and significantly interact with the wakes of the trailing bubbles, generating large liquid perturbations (dashed-box). Considering the fact that rising bubbles at upstream inevitably collide with the cylinder and subsequently rise along the cylinder surface, the attached (and then detached) counter-rotating vortices are built along with the bubble rise trajectories and they do not deviate much and stay within the vicinity of the cylinder ($0.5 < |x/D| < 1.0$). On the other hand, the origin of the secondary vortices which are absent in the single-phase flow past a circular cylinder may come from the collective accumulation of the counter-rotating bubble wakes along the cylinder surface and also possibly from the instantaneous local acceleration in the liquid flow, encompassed in the bubble wakes (opened-arrow in figure 3.25).

The time-averaged spanwise vorticity ($\bar{\omega}_z^* = \bar{\omega}_z D / \langle \bar{v}_b \rangle$) of the bubble-induced liquid flow is shown in figure 3.26, together with the contour of $\bar{\alpha}^*$. As the bubble-induced mean liquid flow passes around the cylinder, a shear layer evolves from the cylinder edge ($x/D = 0.5$). Interestingly, the aforementioned secondary vortices (with an opposite sign of ω_z) are more distinctively induced next to this main shear layer ($x/D = 0.7-0.8$). This secondary vortex structure becomes more elongated as $\langle \bar{\alpha} \rangle$ and D increase. To understand this, we compared the mean spanwise vorticity ($\bar{\omega}_z^*$) and transverse gradient of the streamwise liquid velocity ($\partial \bar{v}_l / \partial x$) in the near wake (for example, at $y/D = 0.65$), and found that the magnitude and location of local peaks match well each other. Furthermore, the local void peaks (α_{peak}) are located between the main and secondary vortices. Thus, it is understood that the bubbles that rise along the cylinder surface generate regions with a higher void fraction near $x/D = 0.7$ and

thus locally accelerates the liquid flow (higher shear is induced) in these locations, which leads to the evolution of the secondary vortex. As $\langle \bar{\alpha} \rangle$ increases, following the change in the void distribution, the higher vorticity region ($\bar{\omega}_z^* \geq 2.0$) becomes wider along with both the streamwise and transverse directions, and thus the location of maximum spanwise vorticity moves accordingly (figures 3.26b and 3.26d). As D increases, the maximum void fraction increases and is observed farther downstream for both flow regimes. Therefore, the magnitude of the bubble-induced $\bar{\omega}_z$ increases as well and the corresponding position is delayed into the downstream region (figures 3.26c and 3.26d).

Considering that bubble-induced liquid flow induces a specific flow structure around the cylinder, it would be interesting to investigate the detailed flow statistics resulting from the bubble-induced flow. The streamwise variations in the time-averaged streamwise (v_i) and transverse (u_i) velocity profiles are shown in figures 3.27 and 3.28, respectively. As shown, the streamwise velocity shows a symmetric distribution that resembles that of a wake defect in the single-phase flow and the transverse component has a skew-symmetric profile with peaks located along with the shear layer, which flattens out fast as the flow develops. The liquid flow is locally accelerated in the presence of more bubbles ($x/D = \pm 0.5$) but is decelerated where the void fraction is smaller ($x/D = 0$). For both regimes, the streamwise velocity profile thus has two maximum and one minimum peaks in the near wake ($y/D \leq 2.0$) following the local void distributions. However, the recovery of the downstream velocity deficit ($y/D \geq 2.0$) is faster for regime II ($\langle \bar{\alpha} \rangle = 0.011$) owing to the enhanced bubble dispersion along the transverse direction (figure 3.27). As $\langle \bar{\alpha} \rangle$ increases, the bubble-induced liquid flow becomes faster from $0.35 \langle \bar{v}_{b\infty} \rangle$ to $0.55 \langle \bar{v}_{b\infty} \rangle$, and the velocity gradient near the cylinder edge becomes sharper. As the diameter of the cylinder increases, the bubble-induced velocity is accelerated even more, with a steeper gradient in the near wake. This is because more bubbles are entrained and shed into the downstream area in the form of a bubble cluster, as shown in figures 3.23b and 3.24b. In addition, this tendency is retained farther downstream and thus the recovery of the velocity deficit is delayed

(figure 3.27b). On the other hand, compared to the single-phase wake at an identical Reynolds number (Re_D where D is the diameter of the cylinder), the size ($x_{1/2}$) of the cylinder wake which corresponds to the locations where the bubble-induced mean liquid velocity equals half the maximum defect velocity ($\overline{v}_l(x_{1/2}, y) = 0.5 \cdot [\langle \overline{v}_{l\infty} \rangle - \overline{v}_l(x=0, y)]$) is reduced significantly, and the recovery of the liquid velocity deficit at downstream is much faster (Parnaudeau et al. 2008; Liu, Deng & Mei 2016). These behaviors are closely related to the bubbles' behaviors in the vicinity of the cylinder (figure 3.25). More specifically, a periodic vortex shedding is hardly developed in the present study, rather a counter-rotating vortex-pair is observed along the trajectories of the rising bubbles blocked by the cylinder (figure 3.25a), because of the liquid-phase acceleration by bubbles (opened-arrow) as well as the accumulation of the bubble wakes. Moreover, bubbles residing along the cylinder surface or inside the cylinder wake agitate the surrounding liquid intensively (figures 3.25b and 3.25c), which contributes to delay the liquid separation from the cylinder surface and makes the liquid velocity deficit rapidly recover ($y/D < 3.5$), collectively shortening the size of the recirculation bubble (figure 3.29). From the viewpoint of a circular cylinder, the Reynolds number for the liquid flow is in the range $Re_D = \langle \overline{v}_l \rangle D / \nu = 2000-5000$, where ν is the kinematic viscosity of water. For a single-phase flow at an identical Re_D , the typical size of a recirculation bubble (the distance from the cylinder base to the location of the zero-mean streamwise velocity on the centerline) has been reported as $l_r/D = 1.4-1.5$ (Parnaudeau et al. 2008; Kim et al. 2015; Liu, Deng & Mei 2016). For the present two-phase flows, it is measured to be $l_r/D = 0.31$ for $\langle \overline{\alpha} \rangle = 0.006$. This indicates that the extent to which the fluid is mixed by surrounding fluids is enhanced significantly compared to a single-phase flow. Because the surrounding water is initially static and the existence of bubbles affects the flow property (e.g., the effective viscosity and density change), the comparison would require more cautious analysis. However, it is understood that the highly enhanced turbulence at the upstream flow (figures 3.20 and 3.22) and the preferential migration of the bubbles behind the cylinder (figure 3.25) are responsible for the considerably reduced size of the recirculation bubble in the wake.

Compared to the streamwise velocity, the magnitude of the transverse liquid velocity (u_t) is quite small and shows an antisymmetric distribution with local peaks (along with the separating-shear layers) where the bubbles are accumulated (figure 3.28). Similar to the streamwise velocity, higher u_t is induced as $\langle \bar{\alpha} \rangle$ increases, which is reduced significantly at $y/D > 2.0$. Even though the defect in the streamwise velocity is recovered faster in regime II, the convergence of the transverse velocity occurs faster in regime I, because of the slight preferential migration of bubbles along the transverse direction. This corresponds to the change in the void distribution (figure 3.11). For $D = 30$ mm, the velocity distribution has the same overall trend but the maximum peak of u_t increases and the slope of the velocity gradient becomes steeper, which is maintained longer downstream (figure 3.28b).

3.3.3 Bubble-induced turbulence in the cylinder wake

Here, we discuss how the bubble-induced turbulence is modified by the existence of the bluff body. First, we analyzed the PDFs of the liquid velocity fluctuations in the wake ($0.5 \leq y/D \leq 3.0$) behind a circular cylinder, to check that the bubble-agitated turbulence contributes dominantly while the destabilization of the mean flow is negligible in the present flow. As shown in figure 3.30, the PDFs of the streamwise and transverse liquid velocity fluctuation (for $\langle \bar{\alpha} \rangle = 0.006, 0.0095$ and 0.011) show the typical trends of bubble-induced agitation both at $|x/D| \leq 0.5$ and $|x/D| > 0.5$ (Risso 2016, 2018). The streamwise velocity exhibits an asymmetric behavior (positive skewness) for all the considered volume void fractions. In addition, the PDFs decay with a slight exponential tail, known as the signature of the bubble wake. The transverse velocity is rather symmetrically distributed centered at the origin with a distinctive exponential tail. Obviously, these characteristics are different from the velocity fluctuation PDF resulting from the mean velocity destabilization in single-phase turbulent flows, in which a Gaussian distribution is measured for homogeneous isotropic turbulence (Alm eras et al. 2017) or an asymmetric distribution with a slight negative skewness for a

fully developed channel flow (Castaing et al. 1990). Thus, it is reasonable to exclusively consider the bubble-induced agitation in the present cases. Although the global shape of the PDFs inside the wake ($|x/D| \leq 0.5$) is similar to that outside ($|x/D| > 0.5$) and of upstream (both are mainly affected by the bubbles) (figure 3.21), it is found that the width of the transverse (streamwise) velocity fluctuation PDF becomes wider (narrower) compared to those measured outside of the wake and upstream (figure 30a-b). This indicates that the bubble-induced flows are more agitated along the transverse direction because a randomly generated separating liquid-shear from the cylinder surface perturbs the surrounding liquid-phase toward the cylinder base in the transverse direction, which is also visually confirmed in figure 3.25.

Nevertheless, one might wonder the turbulent nature of the bubble-induced turbulence is still dominant inside the cylinder wake. To supplementary confirm this, we also find that the scaling relation for $\langle v_{l,rms}'' \rangle / \langle \bar{v}_{b\infty} \rangle \sim \langle \bar{\alpha} \rangle^{0.4}$ is valid at both upstream and downstream even inside the cylinder wake ($|x/D| \leq 0.5$) (figure 3.31a). Moreover, this is in common with the transverse direction (figure 3.31b). Nevertheless, we fully aware that the scaling relation at $|x/D| < 0.5$ alone slightly deviates the trend-line because the turbulence modification ($\Delta v_l''$) caused by the existence of the circular cylinder is quite localized, meaning that the undisturbed bubbly flow at the region outside the cylinder ($|x/D| \geq 0.5$) in downstream maintains the upstream characteristics.

In this context, the detailed spatially-varying root-mean-square values of velocity fluctuations in the streamwise ($v_{l,rms}''$) and transverse ($u_{l,rms}''$) directions are shown in figures 3.32 and 3.33, respectively, and the turbulent stress ($-\overline{v_l'' u_l''}$) profiles are plotted in figure 3.34. These show that even a small amount of bubbles in the system significantly generates a certain level of turbulence in the flow; because there is no background flow, the trends represent the nature of pure bubble-induced turbulence (agitation) around a solid body (figures 3.30 and 3.31). On the other hand, as the upstream flow has quite a high level of turbulence, significant turbulence intensity is also measured outside of the cylinder ($|x/D| >$

0.5) in downstream (figures 3.32 and 3.33). More specifically, the streamwise turbulence intensity shows a relatively simple distribution where it has a broad minimum valley behind the cylinder ($-0.5 < x/D < 0.5$), following the local void distribution (figure 3.11). As the flow develops, this local minimum is mildly restored to the upstream value, which occurs slower with a lower volume void fraction and larger D . As the size (D) of the cylinder increases (figure 3.32b), however, the turbulence level decreases slightly at $-0.5 < x/D < 0.5$. This is interesting because the liquid-velocity gradient becomes steeper in the wake (figures 3.27 and 3.28), which would increase the contribution by the shear-induced turbulence. However, the decrease of liquid-velocity fluctuation with a larger D under an identical volume void fraction indicates that the subsequent contribution by the shear-induced turbulence is not significant in the present flow compared to the changes in bubble-induced fluctuation because, as we mentioned, an organized separating liquid-shear shed from the cylinder surface does not exist (figure 3.25), which is also evidenced in the decrease of the turbulent stress with a larger D (figure 3.34). The dominance of bubble-induced fluctuation in the cylinder wake is identified based on the PDFs of liquid-velocity fluctuations (see figures 3.30a-b), which is the basis of our models for the bubble-induced fluctuation (see chapter 2). As shown in figure 3.11, with a larger D , the recovery of the local void fraction defect in the wake becomes slower, that is, there are fewer bubbles inside the wake region. Since the interaction of wakes behind bubbles has been considered to be the main source of bubble-induced turbulence (Risso 2018), the lower void fraction in the wake would result in the decrease of the bubble-induced fluctuation there. It is also possible that as the ratio $\langle \bar{d}_b \rangle / D$ decreases, i.e., the length scale responsible for the turbulence generation is reduced compared to the characteristic length scale of the flow, the level of turbulence is reduced. However, the size of the cylinder does not alter the turbulence intensity at $|x/D| > 0.5$. The turbulence level in the downstream region outside of the cylinder is proportional to $\langle \bar{\alpha} \rangle^{0.4}$ (figure 3.31); however, it shows a deviation from the scaling relation at $|x/D| < 0.5$. This indicates that the disturbance caused by the existence of the circular cylinder is quite localized and the undisturbed bubbly flow maintains the upstream

characteristics.

The transverse component follows the local void distribution in the wake (figure 3.33). As shown, the $u''_{l,rms}$ has local maximum peaks near the cylinder edge and a minimum valley behind the cylinder base in downstream ($y/D < 2.0$), according to the lateral migration of bubbles. For regime II, the two maximum peaks are in close proximity and a broad peak near $x/D = 0$ is induced along the streamwise direction. In particular, the magnitude of maximum $u''_{l,rms}$ becomes the largest at $y/D = 1.5$ where bubbles that are separated by both sides of the cylinder converge (figures 3.11*b* and 3.11*e*), and decreases as the bubbles disperse. Actually, the transverse turbulence intensity profile shows the most distinct difference between the two regimes, because it is most strongly affected by the wake structure responsible for the oscillating paths of rising bubbles. The transverse turbulence intensity outside of the cylinder ($|x/D| > 0.5$) increases from 0.12 to 0.16 as the inlet volume void fraction increases from 0.006 to 0.011. Together with the liquid-phase velocity data for $\langle \bar{\alpha} \rangle = 0.0095$, we find that the scaling relation of $\langle u''_{l,rms} \rangle / \langle \bar{v}_{b\infty} \rangle \sim \langle \bar{\alpha} \rangle^{0.4}$ is still valid for the downstream flow at $|x/D| > 0.5$ (figure 3.31*b*). The ratio between $v''_{l,rms}$ and $u''_{l,rms}$ is approximately 2:1, which agrees well with that measured for upward laminar bubbly flows (Hosokawa & Tomiyama 2013; Kim et al. 2016) and bubble plume (Simiano et al. 2009) in which the considered gas-phase conditions ($\langle \bar{\alpha} \rangle$ and Re_b) are similar to those in our study.

The turbulent stress ($-\overline{v''_l u''_l}$) has an antisymmetric profile; two peaks (with opposite signs) are located at both sides of the cylinder edge and they rapidly converge to zero along the transverse direction (figure 3.34). In particular, the turbulent stress is very strong in the near wake region ($y/D \leq 1.5$) and decays quite fast at $y/D > 2.0$ as the bubbles disperse and void distributions become uniform. The local peaks of the turbulent stress are enhanced as the inlet volume void fraction increases but are decreased slightly as the cylinder size increases. In the case of $D = 20$ mm (e.g., larger bubbles), the turbulent stress peaks tend to spread widely along the transverse direction, as the flow develops (figure 3.34*a*);

however, it is confined to quite a narrow region (along with the separating shear layers) for the case of $D = 30$ mm (figure 3.34b). The difference between two void fractions ($\langle \bar{\alpha} \rangle = 0.006, 0.011$) becomes smaller for the case of $D = 30$ mm, which is again attributed to the reduced size of the bubble wake relative to the length scale of the flow, indicating that turbulence in the flow is primarily originated from the rising bubbles with deflected trajectories in the transverse direction by the cylinder rather than turbulent production by the destabilization of the upstream bubble-induced mean liquid flow (SIT).

3.4 Interfacial momentum transfer at the phases' interfaces

Thus far, we have discussed the gas- and liquid-phase flow statistics around a circular cylinder, and in terms of time-averaged void distribution, it is classified into two regimes based on the upstream volume void fraction. Here, we explain this regime transition by estimating the lateral forces acting on bubbles with the two-fluid Eulerian interfacial force models available in the literature. Because the present analysis is limited to the time-averaged flow fields, we fully aware that it is insufficient to investigate the dynamics of an individual bubble as a function of time. Nevertheless, we consider it useful to understand the abrupt transition of the mean void distribution according to the condition of the bubble-swarm. We start from the two-fluid momentum balance equations for the gas and liquid phases for the time-averaged flow (equation 1.1). The mechanism for the transverse migration (or preferential concentration) of bubbles toward the cylinder base in downstream can be identified by the balance equation for the hydrodynamic forces in the transverse direction. Therefore, for the sake of convenience, unless specified otherwise, all the forces are written for the transverse direction hereafter. In general, we may select the associated candidates for \bar{M}_g as follows:

$$\bar{M}_g = \bar{F}'_D + \bar{F}'_L + \bar{F}'_{VM} + \bar{F}'_{TD} + \bar{F}'_B + \bar{F}'_W. \quad (3.2)$$

Here, \bar{F}' denotes the time-averaged transverse force per unit volume (N/m^3) and the terms on the right-hand side are drag (\bar{F}'_D), lift (\bar{F}'_L), virtual mass (\bar{F}'_{VM}),

turbulent dispersion (\bar{F}'_{TD}), Basset (history) (\bar{F}'_B), and wall-lubrication (\bar{F}'_W) forces, which are associated with the bubble distributions (Hibiki & Ishii 2007; Hosokawa & Tomiyama 2009; Kim et al. 2016; Lee & Park 2020).

The drag force is proportional to the square of the relative velocity ($\vec{v}_r = \vec{v}_b - \vec{v}_l$) of a bubble, acting to oppose its rising motion, and is expressed as $\bar{F}'_D = c_D \rho_l (3/4 d_b) |\vec{v}_r| \vec{v}_r$. For the drag coefficient, c_D , we use the relation proposed by Ishii & Zuber (1979) such that it reflects the interactions between multiple deformable fluid particles, which is a reasonable choice considering the present gas-phase conditions. The lift force arises when a bubble rises against the (local) velocity gradient of the liquid-phase, and its orientation depends on the direction of \vec{v}_r with respect to that of the out-of-plane liquid vorticity. In our analysis, it is modeled by $\bar{F}'_L = -c_{L0} \rho_l (\vec{v}_b - \vec{v}_l) \times (\nabla \times \vec{v}_l)$ (Drew & Lahey 1987). Here, c_{L0} , is the lift coefficient of a single bubble and we use the model developed for a multi-particle system with the effect of deformation considered (Hibiki & Ishii 2007). For the virtual mass force, it is known to be quite small for lower void fraction cases (Drew & Lahey 1987), and it is calculated to be approximately 0.13% and 0.42% of the total force, for a time-averaged flow, in regimes I and II, respectively. However, in terms of instantaneous flows, the contribution of the virtual mass force increases to approximately 10% owing to the locally accelerated flow near the bubble, indicating that the effect of virtual mass would not be negligible in the instantaneous flow. The turbulent contribution due to the virtual mass force to the interfacial momentum transfer term has been discussed previously (Chahed et al. 2003). This is an interesting point and would be important in analyzing the dynamics of an individual bubble as a function of time. However, as mentioned above, this is beyond the scope of the present study and may be pursued as in a separate future study. The Basset force, i.e., the effect of time decay in boundary layer development at the bubble surface (Reeks & Mckee 1984), is calculated to be below 0.1% of the total force for both time-averaged and instantaneous flow fields. The wall-lubrication force, which represents the confinement effect of the vessel (repelling force away from the wall), can be

considered. However, the present vessel size is quite large (the sidewall is approximately $17D$ away from the cylinder center) such that the repelling force would not affect the bubbles in the current region of interest, i.e., FoV (Antal et al. 1991).

Therefore, from equation 3.2, the resultant transverse (x -direction) momentum balance equation for the gas-phase is reduced to

$$\bar{F}'_T = \bar{\alpha} \left(-\frac{\partial \bar{p}}{\partial x} \right) + \bar{M}'_g = \bar{F}'_p + \bar{F}'_D + \bar{F}'_L + \bar{F}'_{TD}. \quad (3.3)$$

Here, \bar{F}'_T represents the total transverse force (per unit volume) acting on bubbles, and \bar{F}'_p is the contribution from the pressure gradient in the flow. On the other hand, the turbulent dispersion force has previously been modeled in terms of the gradient of the local void distribution ($\nabla \alpha$) (Lahey et al. 1993; Burns et al. 2004), indicating that it is quite challenging to consider \bar{F}'_p and \bar{F}'_{TD} separately because ∇p and $\nabla \alpha$ are closely coupled. Despite this complexity, several previous studies applied the linear superposition of each contribution to study bubbly flows with a lower volume void fraction (Antal et al. 1991; de Bertodano 1998; Troshko & Hassan 2001). This approach would not be conclusive but, as shown below, the pressure gradient becomes more dominant because of the circular cylinder wake and the turbulent force term is negligible compared to the other forces. Among the available models for \bar{F}'_{TD} , we use $\bar{F}'_{TD} = -c_{TD} \rho_l k_l \nabla \bar{\alpha}$ proposed by Lahey et al. (1993). We calculated the turbulent kinetic energy of the liquid phase by assuming that the bubble-induced velocity fluctuations along the transverse and spanwise directions are comparable; that is, $k_l = 0.5 \left(\overline{v_l'' v_l''} + 2 \overline{u_l'' u_l''} \right)$. This assumption on the liquid-phase velocity fluctuations in bubbly flows is supported by previous studies (Troshko & Hassan 2001; Simiano et al. 2009; Riboux et al. 2010; Hosokawa & Tomiyama 2013; Lai & Socolofsky 2019). de Berodano (1998) suggested the turbulent dispersion coefficient as $c_{TD} = 0.1$ for millimeter-sized ellipsoidal bubbles. This was inspired by the eddy diffusivity coefficient ($c_\mu = 0.09$) used in the single-phase k - ε turbulence model because the dispersion force was modeled analogously to the single-phase flow Reynolds stress term to address the closure problem

occurring at the gas-liquid interface (de Bertodano 1998; Troshko & Hassan 2001).

The contribution by the pressure gradient, \bar{F}'_p , is estimated from the momentum balance equation for the liquid phase (equation 1.1), considering the convective acceleration together. This is used to calculate the total lateral force and its decomposition (acting along the x -direction) is calculated for the cases of $D = 20$ mm and 30 mm when $\langle \bar{\alpha} \rangle = 0.0095$ (figure 3.36). We chose $\langle \bar{\alpha} \rangle = 0.0095$ because it belongs to either regime I or II depending on D , and the changes in the interfacial forces would be associated with the regime transition. Shown in figure 3.36 is the streamwise variation of each force (negative values denote the force acting toward the cylinder center) at three transverse locations ($x/D = 0.25, 0.5$ and 0.75) (figures 3.36b and 3.36d), together with the contour of the normalized gradient of the local void fraction ($\partial \bar{\alpha} / \partial x$) (figures 3.36a and 3.36c). Here, it is noted that the summation of each component is not zero (dashed-line) is non-zero in the very near-wake region, indicating that a preferential migration of bubbles occurs along the transverse direction. That is, if we apply equation 3.3 to the upstream ($-4.0 \leq y/D \leq -0.5$) flow where the local void distribution is relatively uniform, we confirm that the magnitude of the net lateral force is calculated to be almost zero (figure 3.35). For both regimes, in general, it is learned that the force due to the pressure gradient plays an important role in understanding the different void distribution, and the turbulent force quite negligible (figures 3.36b and 3.36d). When $D = 20$ mm, at which the case of $\langle \bar{\alpha} \rangle = 0.0095$ is close to the regime II, \bar{F}'_D and \bar{F}'_L are more influential than \bar{F}'_p (figure 3.36b), however, the contribution of \bar{F}'_p also becomes important for $D = 30$ mm ($\langle \bar{\alpha} \rangle = 0.0095$ belongs to the regime I) (figure 3.36d). When $\langle \bar{\alpha} \rangle = 0.0095$ is in regime II, the effect of the pressure gradient (\bar{F}'_p) is very small in the very near wake but is gradually increased at $y/D \geq 2.0$ as the flow develops, and this tends to drive the bubbles away from the cylinder center (figure 3.36b). On the other hand, the lift force (\bar{F}'_L) increases drastically due to the enhanced shear in the liquid flow, causing the bubbles to move toward the cylinder center. These trends are observed

in common at $0.25 \leq x/D \leq 0.75$, resulting in the preferential concentration of bubbles in the wake behind the circular cylinder (characteristic void distribution of regime II).

As the size of the cylinder increases (figure 3.36d), each force component shows a different spatial variation. Inside the wake ($|x/D| \leq 0.5$), the drag force (\bar{F}'_D) is initially balanced by $\bar{F}'_L + \bar{F}'_P$, which changes to $\bar{F}'_L > \bar{F}'_D + \bar{F}'_P$ (at $x/D = 0.25$), and $\bar{F}'_P > \bar{F}'_D + \bar{F}'_L$ (at $x/D = 0.5$) at $y/D > 1.5$. This can be understood to mean that the dominant force component varies along the x -direction and the forces act in opposite directions to prevent the bubbles from gathering at the cylinder center. At $x/D = 0.75$ where the local void peak is found in regime I (figure 3.11), the sum of the lift and pressure gradient forces is counteracted by the drag force and thus the bubbles tend to stay there.

Thus, the balance between the drag force and the pressure gradient and lift forces is mainly responsible for regime I, whereas the strong shear-induced lift force causes the accumulation of bubbles behind the cylinder regime II. As $\langle \bar{\alpha} \rangle$ increases, the bubble velocity decreases but the induced liquid velocity increases even more, as we have shown above. This suggests that the change in the relative bubble velocity tends to reduce the shear-induced lift force; however, the steeper liquid velocity gradient due to the strongly accelerated flow behind the cylinder (at $0.25 \leq |x/D| \leq 0.75$) has a greater influence on increasing the lift force. Therefore, the increase in the bubble-induced mean liquid flow behind the circular cylinder (figure 3.27) is considered to be the main source of enhanced shear-induced lift force. On the other hand, in regime II, the drag force initially dominates (at $y/D > 2.0$), because the void distribution converges rapidly in the downstream region.

3.5 Validations and discussions

As we have shown above, even with a small number of bubbles in the flow, substantial liquid-flow agitation is induced and this phenomenon occurs quite in common in various natural and industrial environments. Especially when an unbounded homogeneous bubble-swarm in quiescent liquid passes a circular

cylinder, the destabilization of the bubble-induced mean liquid flow at downstream supplementary modifies the upstream characteristics of the bubble-agitated turbulence (equation 2.20), which also induces turbulent stresses at downstream. To reflect the actual physics, we have additionally considered (modeled) the turbulence modification by the cylinder in the framework of the two-phase mixing-length theory, which has distinct advantages and also limitations. To achieve this, we have improved the existing model for the mixing-length under a more realistic environment (figure 2.1) to have a dependency on the volume void fraction in the system (equation 2.6). Furthermore, we have proposed (validated) an asymptotic scaling law for the bubble-induced mean liquid flow (equations 2.14 and 2.15). Developing all the submodels needed to close the two-phase Reynolds stress tensor results in the development of a model for the bubble-induced streamwise liquid fluctuation (equation 2.24) and turbulent stress (equation 2.29), respectively. On the other hand, we have confirmed that the fluctuating nature of the pure bubble-induced turbulence is nevertheless maintained inside of the cylinder wake (figure 3.30) where un-organized separating liquid shear layers are developed randomly (figure 3.25), although turbulent production by the gradient of the bubble-induced liquid flow exists to some extents, the typical characteristics of the bubble-agitated turbulence are relevant in this study (figure 3.31).

Based on this background knowledge, we now move on to the validation of the proposed models separately. First of all, we have compared the predicted root-mean-square of the bubble-induced streamwise liquid fluctuation (equation 2.24) with the measurements in figure 3.37. The empirical prefactors (c_n) tuned by the least-square method are shown in figures 3.39(c)-(d). For the considered volume void fraction cases (regime I and II), the prediction results show excellent prediction performance such that the locations and absolute magnitudes of the local peaks are matched well with the measurements. Furthermore, the model is capable of predicting the spatially-varying turbulence quantities in downstream (figures 3.37a and 3.375b), which is in common to the larger D (equivalent to the smaller bubbles) (figures 3.37c-d). It is again worth mentioning that, to the best of our knowledge, even inside the cylinder wake ($|x/D| < 0.5$), our model surely predicts the actual physic, and of course, in regions free of the cylinder influence (e.g.,

upstream and downstream outside the cylinder wake, i.e., $|x/D| > 0.5$), the proposed model (equation 2.24) coincides with the existing model by Riboux et al. (2010). The prefactors (c_n) varies within the ranges of $6 < c_1 < 7$ and $0 < c_2 < 2$ (figures 3.39c-d). Especially c_2 is initially around 2.0 at $y/D < 1.5$ in downstream (figure 3.39d), but decreases gradually away from the cylinder; the complicated nonlinear interactions between the detached wake structures are influential in the cylinder wake, i.e., additional turbulence modification by the re-distributed bubbles, but the extent to which they occur decays gradually as the bubbles disperse more uniformly. Eventually, c_1 responsible for the pure bubble-induced turbulence becomes larger while c_2 is gradually decreased in downstream, indicating that the flow turbulence resembles that by an unbounded homogeneous bubble-swarm in quiescent liquid. Moreover, this characteristic can also be confirmed by decomposing each contribution (first- and second-term in equation 2.24) as shown in figure 3.37a. The pure nature of the bubble-induced turbulence (first-term) alone is accurate outside the cylinder wake at downstream while it underestimates the actual turbulence inside the cylinder wake. On the other hand, the contributions by re-distributed bubble wake (second-term) reasonably supplement these deviations which are attenuated rapidly as bubbles disperse uniformly. Therefore, we judge that each term in our model for the bubble-induced streamwise liquid fluctuation sensitively responds to relevant environments (e.g., an intensity of the separating liquid-shear, or uniformity in bubble distributions) while sufficiently reflecting the physical meanings as well as the previous findings.

Likewise, we have examined the prediction performance of the developed model for the bubble-induced turbulent stress (equation 2.29), which is innately absent at upstream but emerges by the destabilization in the mean liquid flow by the cylinder. In other words, the model would essentially be zero at upstream as well as far away from the cylinder in downstream in the transverse direction ($|x/D| > 1.0$). First, we have compared the estimations with the measurements for the considered volume void fractions (figure 3.38), and the evolution of the prefactors (c_r) is shown in figures 3.39(a)-(b). For all cases, the prediction results are in a reasonably good agreement with the experimentally measured spatially-varying turbulent stress in the cylinder wake ($|x/D| < 0.5$); in particular, magnitudes and

corresponding locations of local peaks are well-matched (figures 3.38a-b), which is in common to the larger D (equivalent to the smaller bubbles) (figures 3.38c-d). It is again worth mentioning that, to the best of our knowledge, even inside the cylinder wake ($|x/D| < 0.5$), our model surely predicts the actual physic, and of course, in regions free of the cylinder influence (e.g., upstream and downstream outside the cylinder wake, i.e., $|x/D| > 0.5$), the proposed model (equation 2.29) becomes negligible. On the other hand, the values of the prefactors used in the estimation are shown in figures 3.39(a)-(b), and this provides an indication of the dominant contribution among the different terms in the model. For example, the contributions by c_{1r} and c_{2r} are initially comparable at the very near wake ($y/D \leq 1.0$), meaning that effects by the bubble-induced mean liquid shear ($\partial \bar{v}_l / \partial x$) and in-homogeneously distributed bubbles' behaviors ($\partial \bar{v}_r / \partial x$, $\partial \bar{\alpha} / \partial x$) are both influential because the upstream bubbles are disturbed most significantly by the cylinder. As the flow develops in downstream, upstream characteristics are rapidly recovered and thus the relative contribution by c_{2r} is suppressed whereas that by c_{1r} becomes larger at $y/D > 1.0$. The value of c_{1r} tends to increase along the downstream while c_{2r} decreases slowly. Here, we have also decomposed the developed bubble-induced turbulent stress model (equation 2.29) into the first- and the rest of terms in the figure 3.36a. It is found that the contribution by the gradient of the bubble-induced mean liquid velocity which is similar to the pure inviscid model by Sato & Sekoguchi (1975) overestimates the actual turbulence: the absolute magnitudes of the local maximum peaks are not matched with the experiments and it also erroneously estimates the secondary peaks with an opposite sign next to the main peaks ($|x/D| = 0.7$). These errors are compensated by the gradients of the bubble velocity and local void fraction where they act adversely to the inviscid flow (similar to the first-term) while eliminating the falsely estimated secondary peaks and ultimately matching the prediction results with the experimental data. The reason why the contributions by the redistributed bubbles by the cylinder (second- and third terms in the equation 2.29) act as oppose to the first-term is that bubbles that are separated from both sides of the cylinder surface do not immediately migrate into the cylinder base right behind the cylinder wake

($0.5 < y/D < 1.0$) (figures 3.8 and 3.9), rather they move almost vertically for a while. However, it is not the case for the separating liquid-phase shear-layer such that the size of the recirculation bubble (L_r) is about $0.31D$ where the turbulent stress is most significant (figure 3.29). Therefore, it can be interpreted that bubble behaviors there destroy the periodic (and organized) vortex shedding and hinder the development of the turbulent stress in the liquid-phase. Therefore, we judge that each term in our model for the bubble-induced turbulent stress sensitively responds to relevant environments (e.g., an intensity of the separating liquid-shear, or uniformity in bubble distributions) while sufficiently reflecting the physical meanings as well as the previous observations.

Application of the present models may cause the prefactors to vary depending on the flow condition and geometry; however, the range of variation does not seem to be significantly wide, rather it is more helpful to understand the dominant contributions from the liquid- and gas-phase statistics to the bubble-induced turbulence, especially for complex geometries.

Considering the reasonably acceptable performance of the models (equations 2.24 and 2.29), despite its simplicity due to the low-order mixing-length approximation, we have learned the importance of considering the contributions of the local void fraction and bubble rise velocity to predict the bubble-agitated turbulence in more complex geometries. On the other hand, an increase in the volume void fraction has the result of strengthening the influence of bubble-wakes (e.g., a spatial- and temporal-fluctuation). Furthermore, the proposed models that account for the bubble-induced flow as well as the potential flow contribution would be expected to be useful even at a higher volume void fraction. However, the void-dependency of the bubble rise velocity in quiescent water ($\langle \bar{v}_b \rangle \sim \langle \bar{\alpha} \rangle^{-0.1}$) and the bubble-induced liquid fluctuation ($v_{l,rms}'' \sim \langle \bar{\alpha} \rangle^{0.4}$) on which the models based were validated for the volume void fraction up to 0.1 (Riboux et al. 2010). As a separate study, it would be thus necessary to verify whether the proposed models could be also applied to different flow geometries with a higher void fraction.

$\langle \bar{\alpha} \rangle$	$\langle \bar{d}_b \rangle$ [mm]	$\langle \bar{v}_{b\infty} \rangle$ [mm/s]	$\langle \bar{\beta} \rangle$	Re	We	Eo	Mo
0.003	3.7	334	1.9	1240	5.8	1.89	1.11×10^{-11}
0.006	3.5	318	1.9	1120	5.0	1.69	1.11×10^{-11}
0.009	3.4	310	1.9	1060	4.6	1.59	1.11×10^{-11}
0.0095	3.4	308	1.9	1050	4.5	1.59	1.11×10^{-11}
0.011	3.5	303	1.9	1060	4.5	1.69	1.11×10^{-11}
0.02	4.2	313	1.9	1320	5.8	2.43	1.11×10^{-11}
0.021	4.1	289	1.9	1190	4.8	2.32	1.11×10^{-11}

Table 3.1. Characteristics of the considered gas-phase. Here, the subscript “ ∞ ” denotes a variable measured at the upstream location.

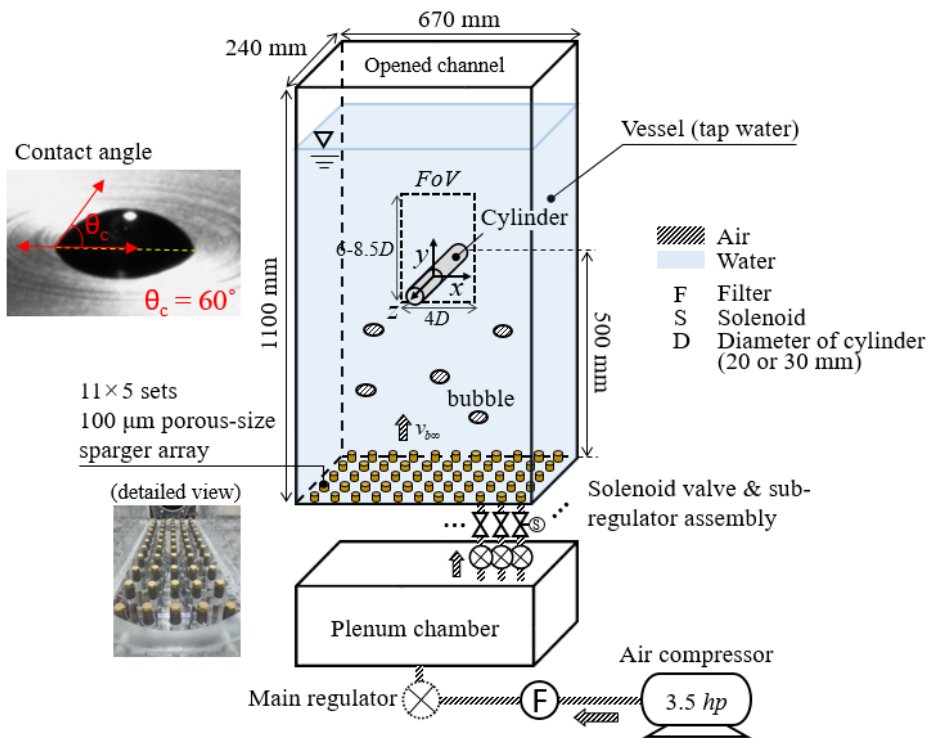


Figure 3.1. Schematic diagram for an experimental setup to generate bubbly flows over a circular cylinder in a stagnant water tank.

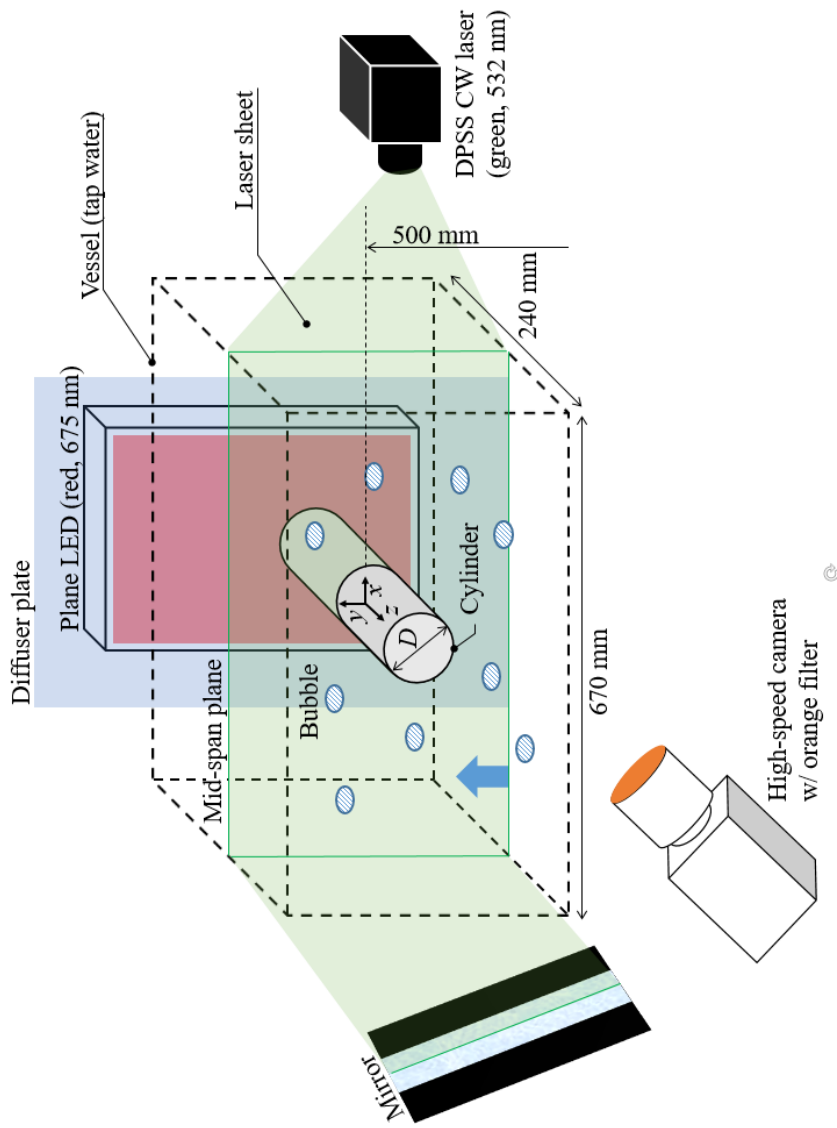


Figure 3.2. Experimental setup for the two-phase high-speed particle image velocimetry measurement.

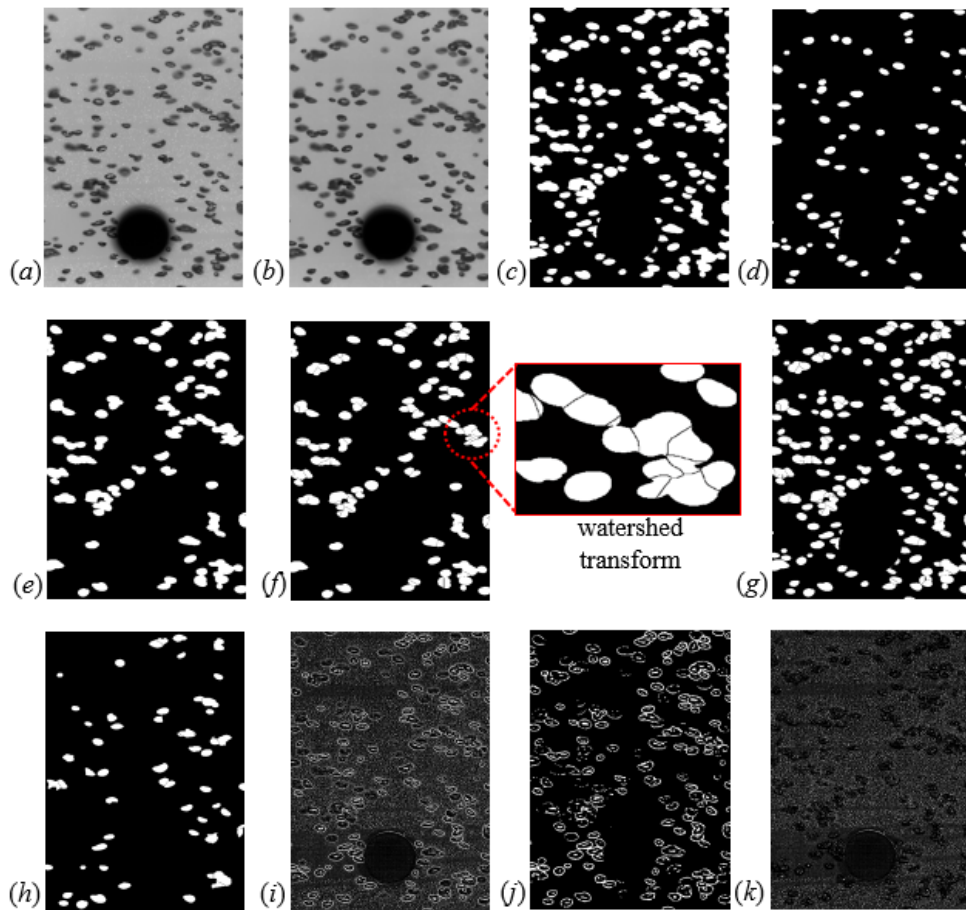


Figure 3.3. Image processing sequence to discriminate gas (*h*) and liquid (*k*) phases from a raw image (*a*) obtained by two-phase particle image velocimetry.

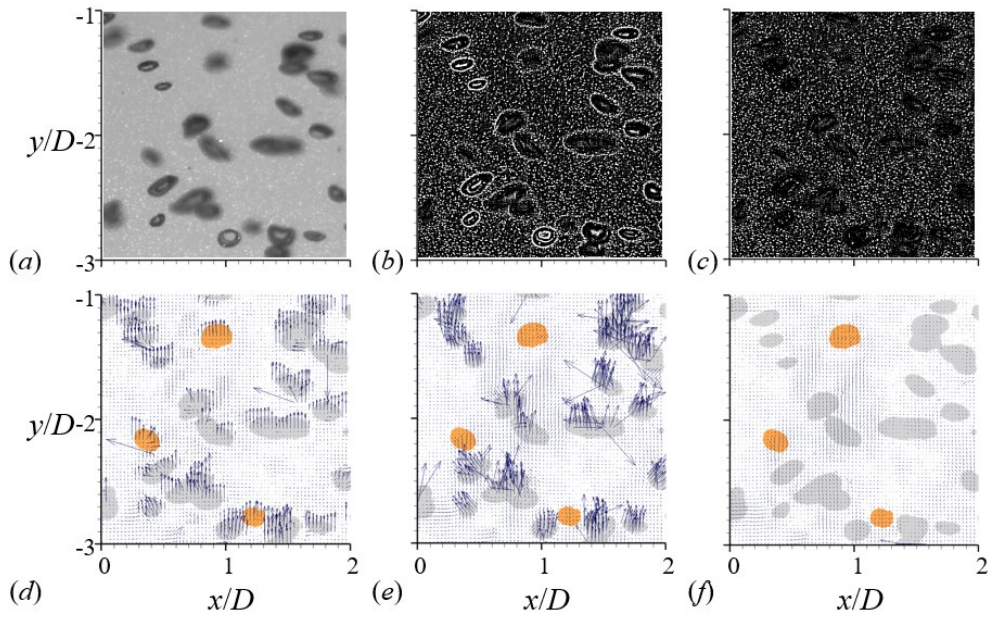


Figure 3.4. Comparison of liquid velocity fields per each post-processing step: (a) a representative raw image measured at upstream for the volume void fraction of 0.006; (b) LoG-filtered image; (c) final image by subtracting median filtered image from the LoG image; (d) calculated liquid velocity field through the PIV with the raw image as an input; (e) with LoG image; (f) with the final image (after weighted spatial linear interpolation); Here the grey-colored bubbles are located on and in front of the half-width of the test section while orange-colored bubbles are behind the measurement plane.

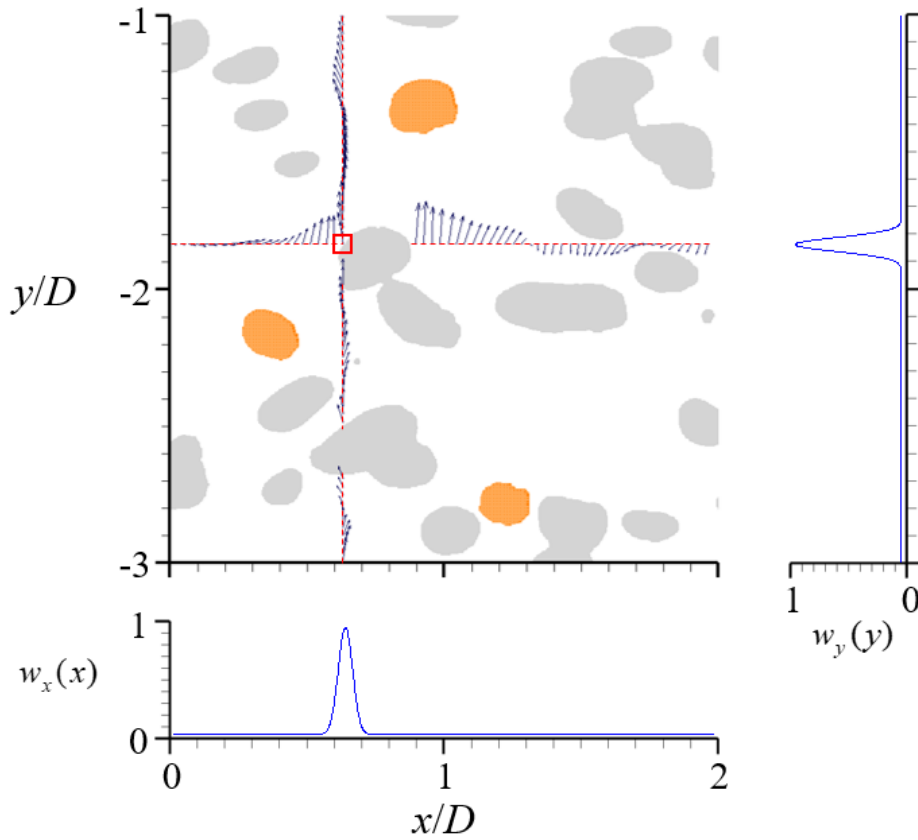


Figure 3.5. An example of the weighted spatial linear interpolation at a point at the bubble interface (red-box): neighboring vectors that have the same x - and y -coordinate outside the bubble are adopted for the interpolation together in the Gaussian weight kernels. Here the grey-colored bubbles are located on and in front of the half-width of the test section while orange-colored bubbles are behind the measurement plane.

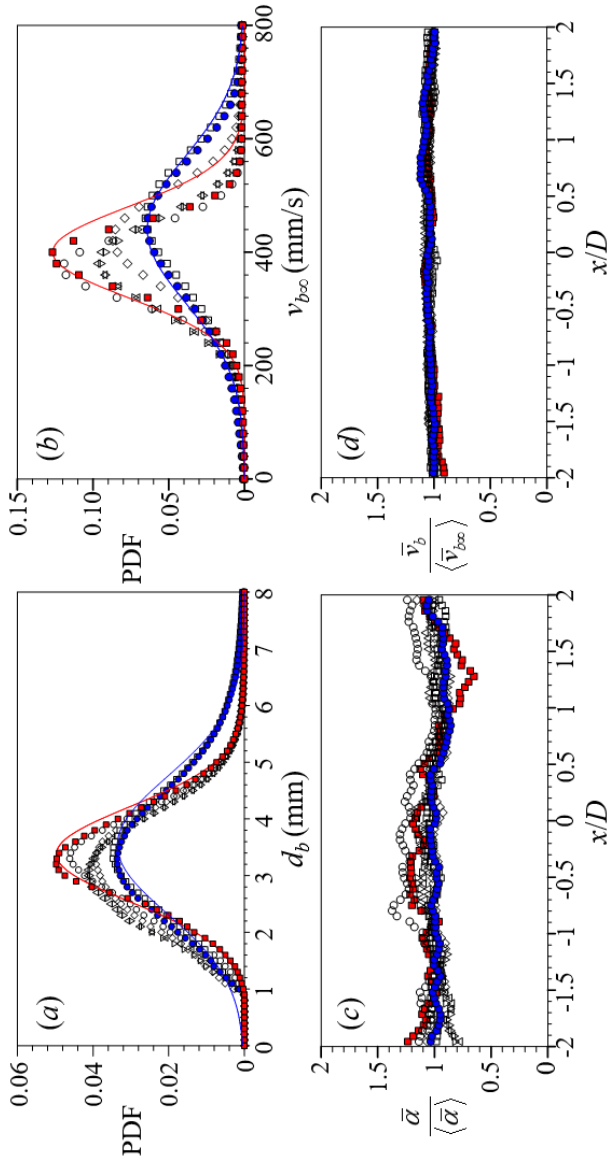


Figure 3.6. Upstream ($y/D = -1.5$) condition of gas phase: (a,b) probability density function (PDF) of equivalent diameter (d_b) and rise velocity ($v_{b\infty}$) of bubbles; (c,d) transverse distribution of local void fraction ($\bar{\alpha}$) and mean bubble rise velocity (\bar{v}_b). ■, $\langle \bar{\alpha} \rangle = 0.003$; ○, 0.006; △, 0.009; ▽, 0.0095; ◇, 0.011; □, 0.02; ●, 0.021. In (a) and (b), Solid lines denote the Gaussian curve for $\langle \bar{\alpha} \rangle = 0.003$ and 0.021, shown for a comparison.

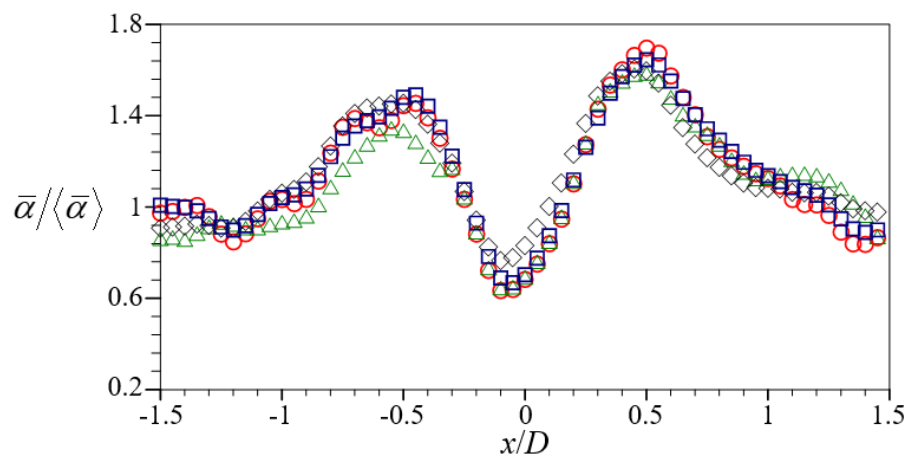


Figure 3.7. Typical local void ($\bar{\alpha}$) distributions in the wake ($y/D = 1.5$) behind a circular cylinder normalized by the upstream volume void fraction ($\langle \bar{\alpha} \rangle$): \square , in-focused bubbles at $z/D = 0$ plane; \triangle , $z/D = -3$; \diamond , $z/D = +3$; \circ , all bubbles. Maximum deviation is about 14% at $x/D = -0.75$.

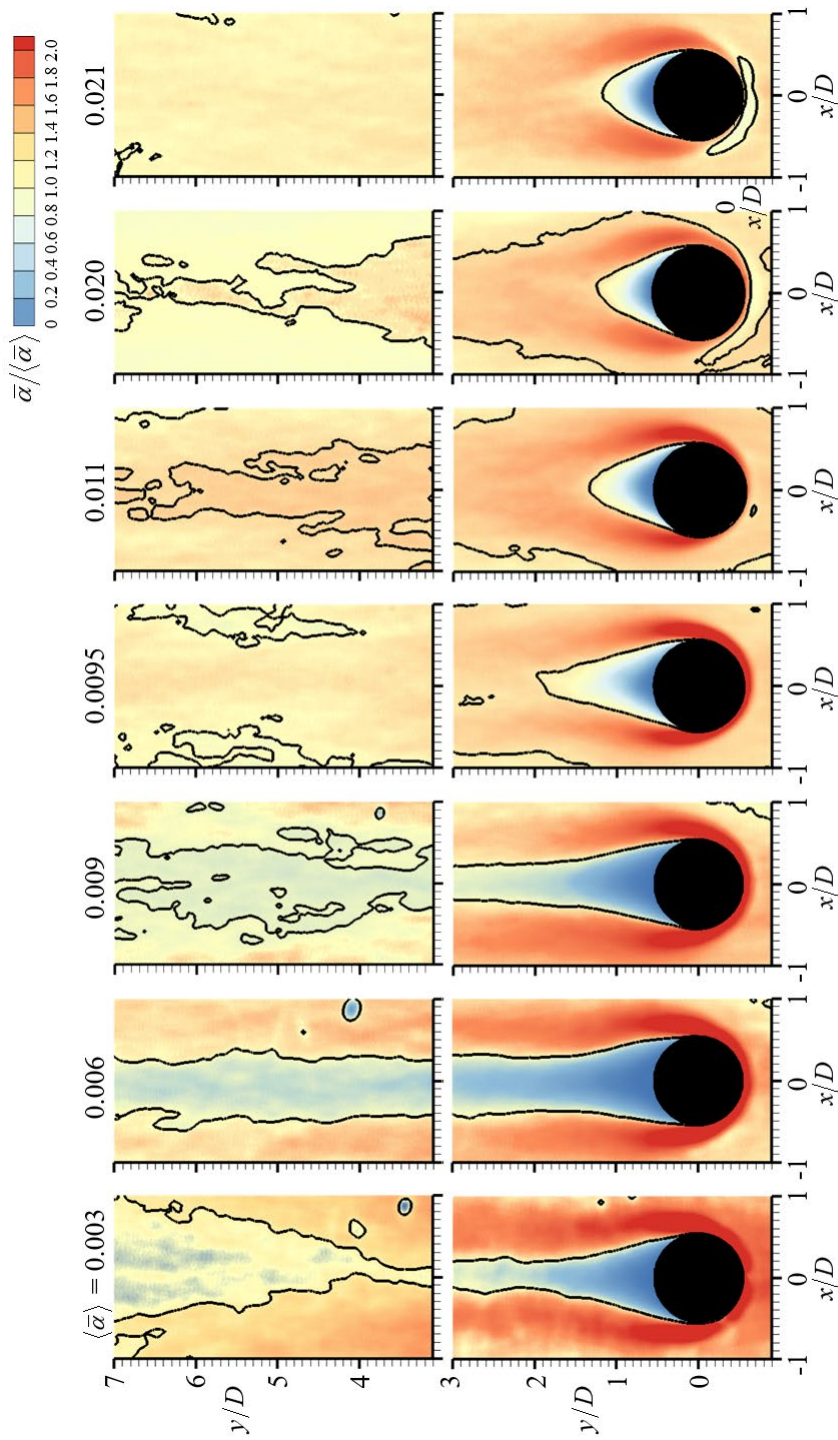


Figure 3.8. Contours of time-averaged in-focus bubble distributions in the cylinder wake (whose diameter is 20 mm, centered at the origin) normalized by the upstream mean void fraction $\langle\bar{\alpha}\rangle$; Normalized void fraction is highlighted when $\bar{\alpha}/\langle\bar{\alpha}\rangle = 1$ (thick solid-line).

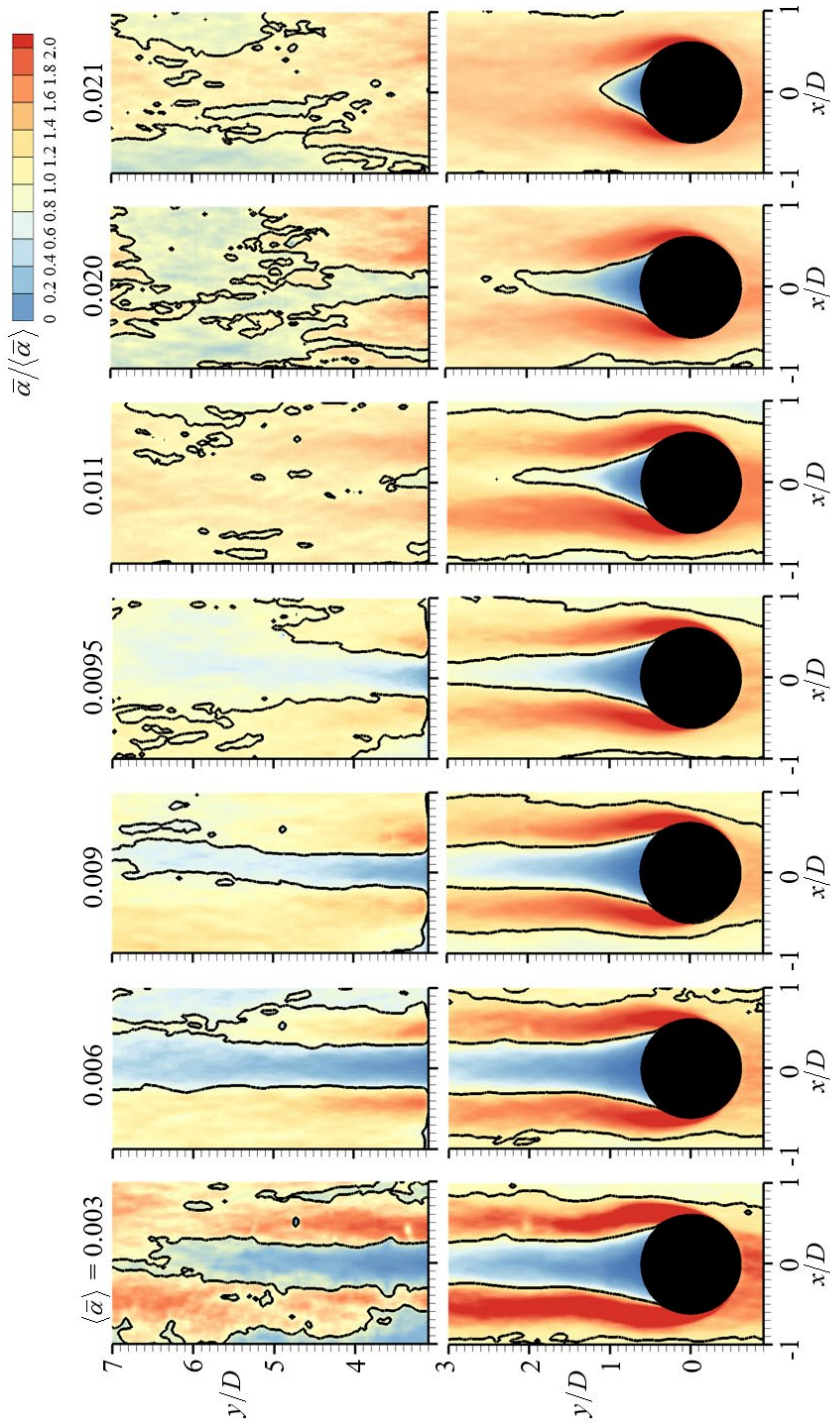


Figure 3.9. Contours of time-averaged in-focus bubble distributions in the cylinder wake (whose diameter is 30 mm, centered at the origin) normalized by the upstream mean void fraction $\langle\bar{\alpha}\rangle$; Normalized void fraction is highlighted when $\bar{\alpha}/\langle\bar{\alpha}\rangle = 1$ (thick solid-line).

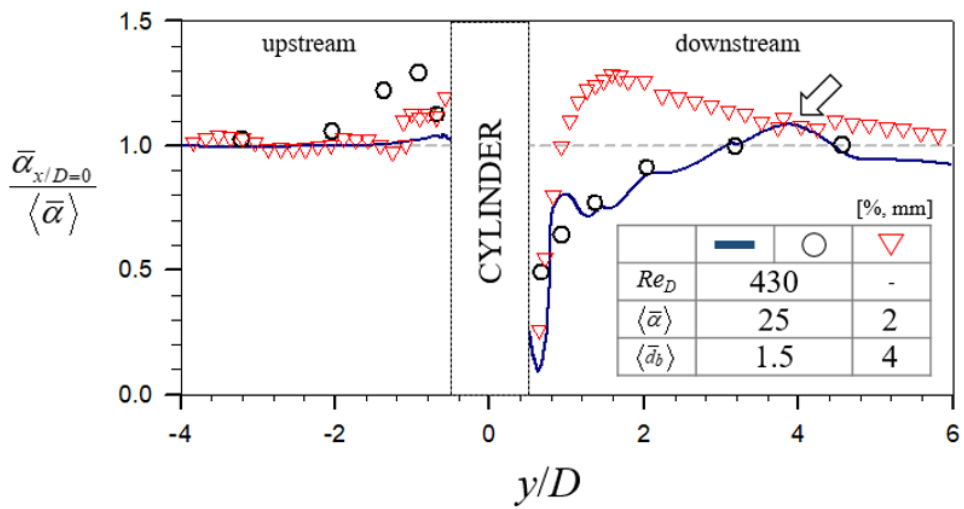


Figure 3.10. Streamwise distributions of the normalized local void fraction measured at the symmetry axis ($x/D = 0$); a solid-line, Sugiyama et al (2001); ○, Joo & Dhir (1994); ▽, present experiment.

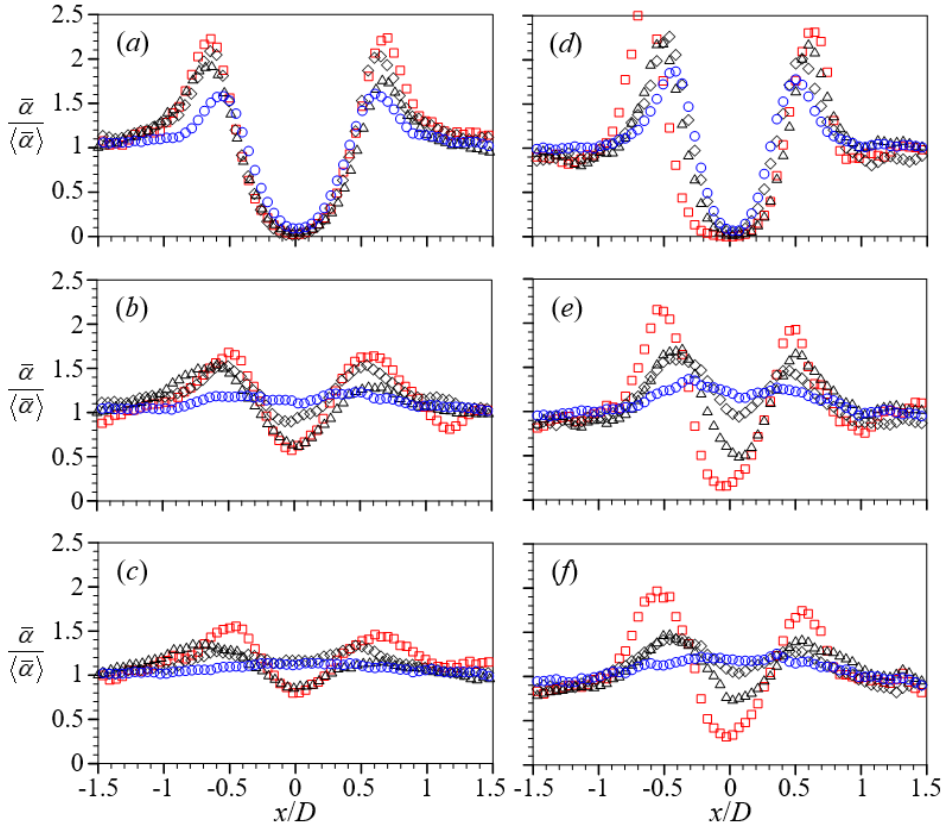


Figure 3.11. Transverse distribution of local void fraction ($\bar{\alpha}/\langle\bar{\alpha}\rangle$) at (a,d) $y/D = 0.65$; (b,e) 1.5; (c,f) 2.5 behind the cylinder of $D = 20$ mm (a-c) and 30 mm (d-f): \square , $\langle\bar{\alpha}\rangle = 0.003$; \triangle , 0.009; \diamond , 0.011; \circ , 0.021.

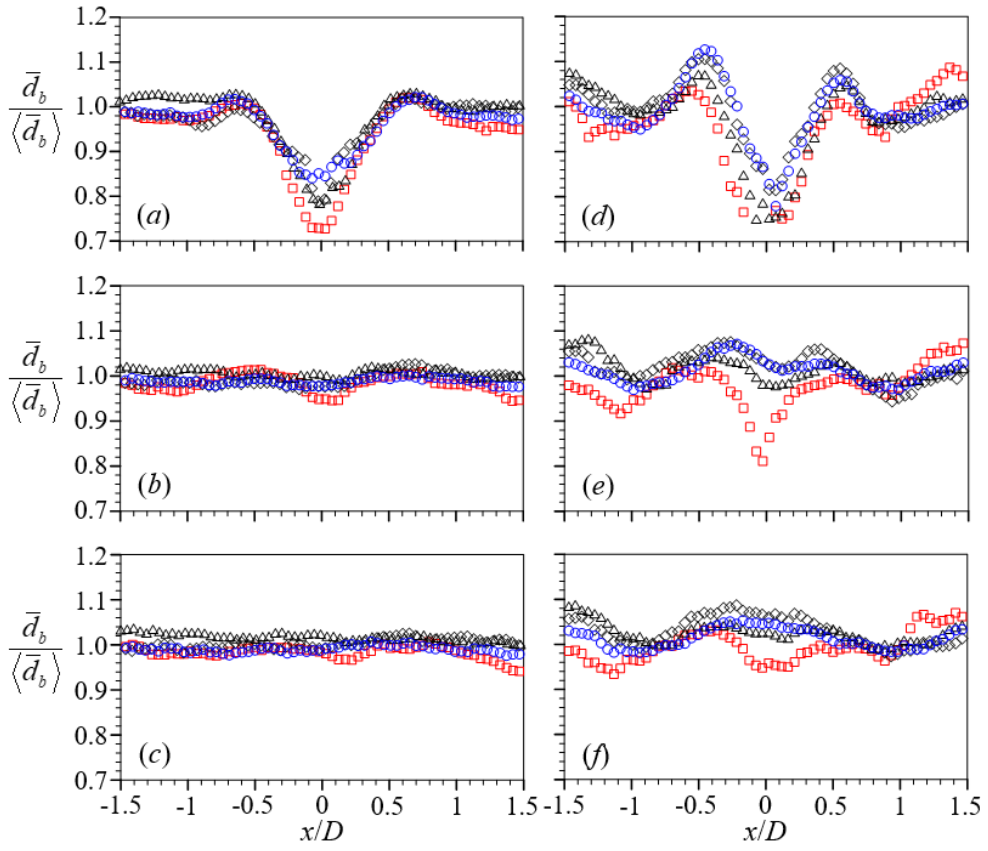


Figure 3.12. Transverse distribution of equivalent bubble diameter ($\bar{d}_b / \langle \bar{d}_b \rangle$) at (a,d) $y/D = 0.65$; (b,e) 1.5; (c,f) 2.5 behind the cylinder of $D = 20$ mm (a-c) and 30 mm (d-f): \square , $\langle \bar{\alpha} \rangle = 0.003$; \triangle , 0.009; \diamond , 0.011; \circ , 0.021.

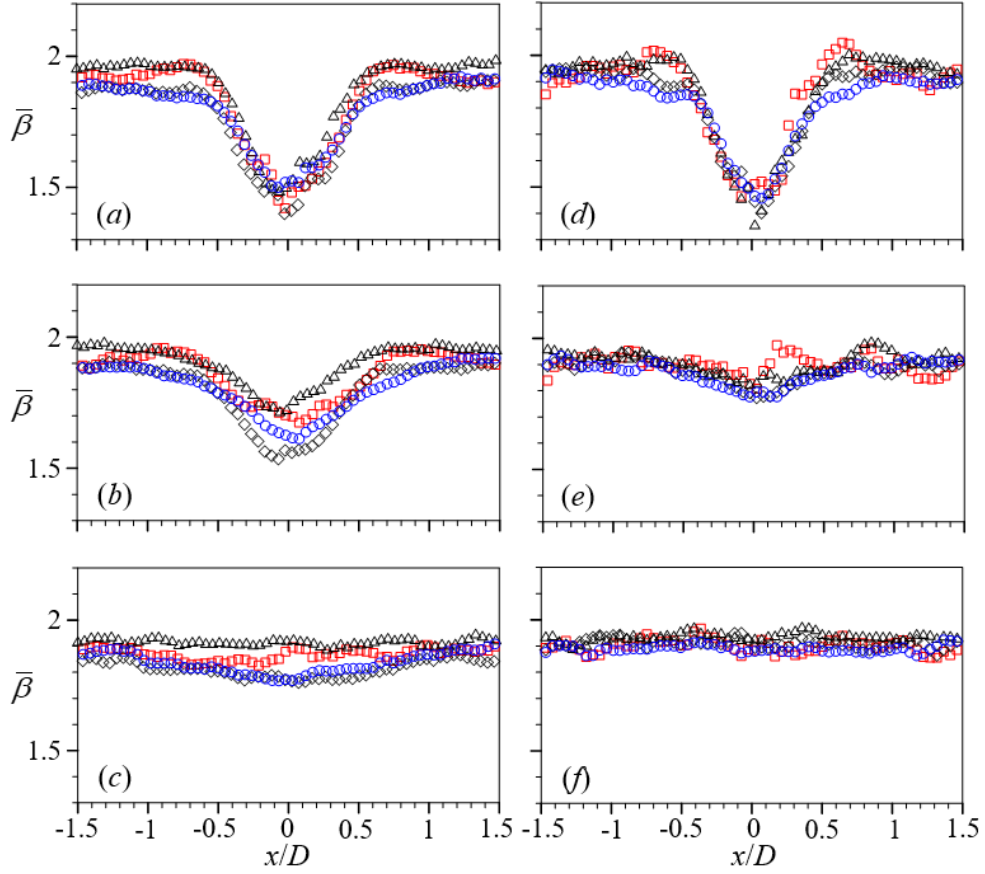


Figure 3.13. Transverse distribution of bubble aspect ratio ($\bar{\beta} = \bar{d}_h / \bar{d}_v$) at (a,d) $y/D = 0.65$; (b,e) 1.5; (c,f) 2.5 behind the cylinder of $D = 20$ mm (a-c) and 30 mm (d-f): \square , $\langle \bar{\alpha} \rangle = 0.003$; \triangle , 0.009; \diamond , 0.011; \circ , 0.021.

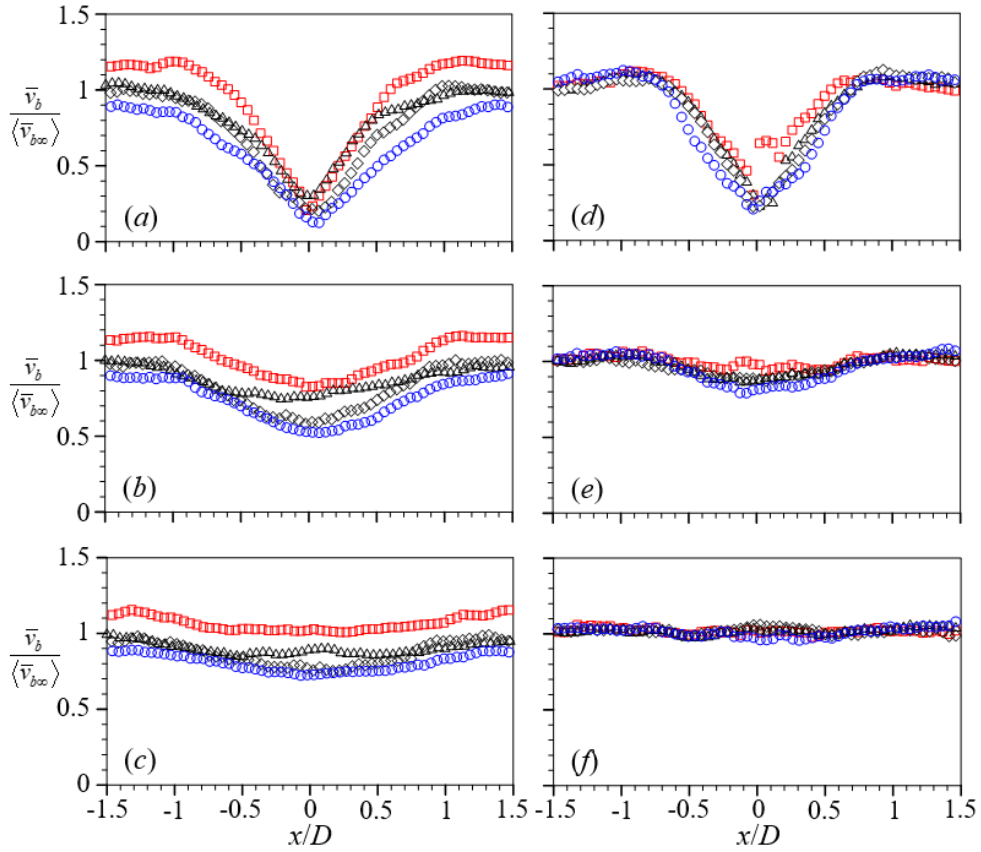


Figure 3.14. Transverse distribution of streamwise mean bubble rise velocity ($\bar{v}_b / \langle \bar{v}_{b,c} \rangle$) at (a,d) $y/D = 0.65$; (b,e) 1.5; (c,f) 2.5 behind the cylinder of $D = 20$ mm (a-c) and 30 mm (d-f): \square , $\langle \bar{\alpha} \rangle = 0.003$; \triangle , 0.009; \diamond , 0.011; \circ , 0.021.

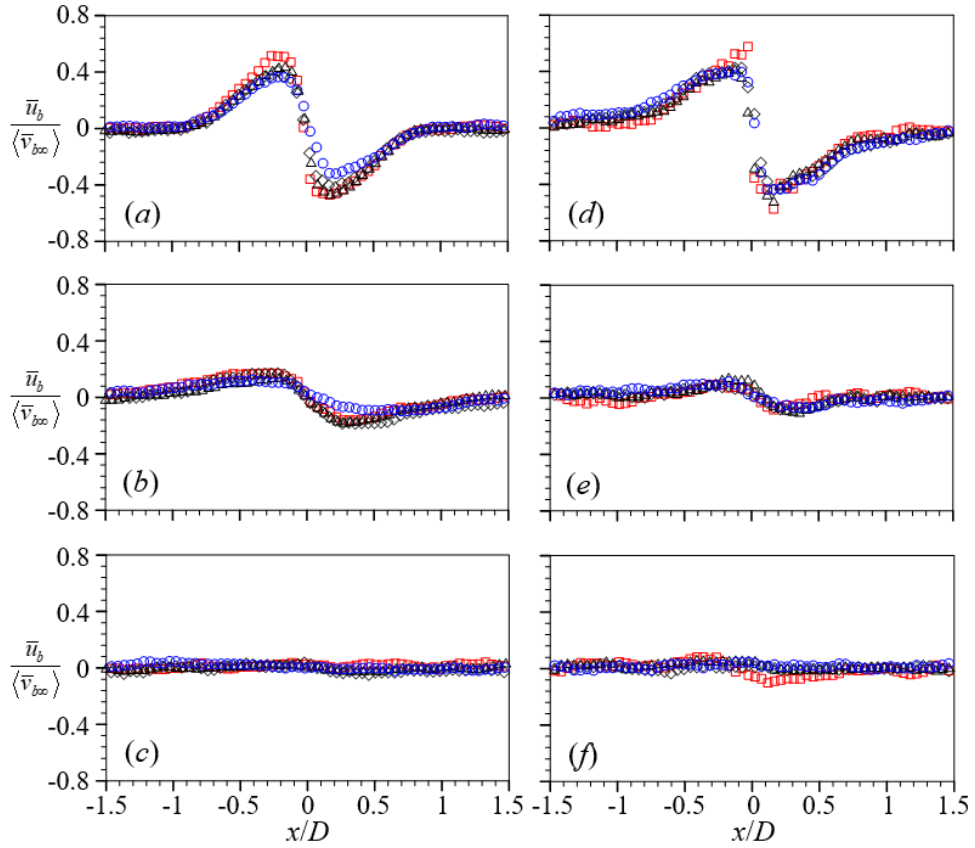
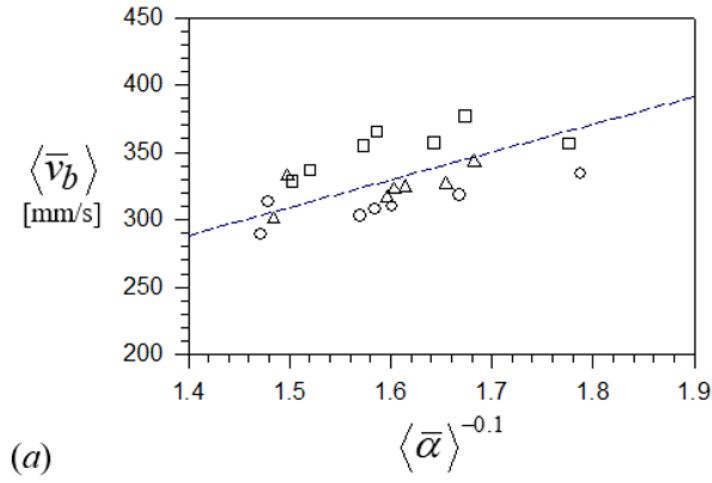
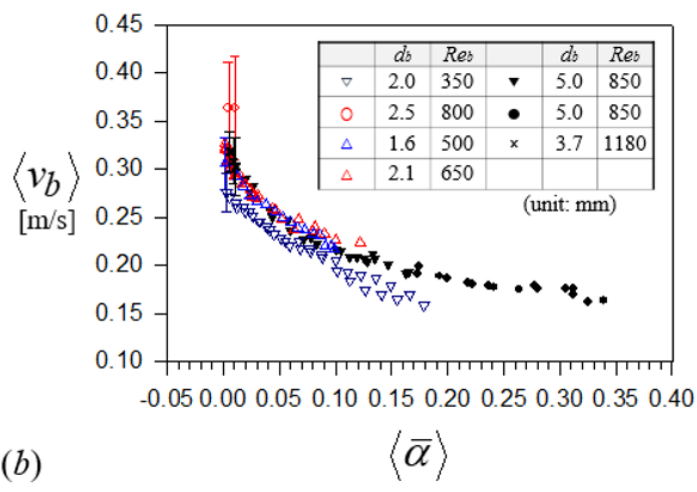


Figure 3.15. Transverse distribution of transverse mean bubble rise velocity ($\bar{u}_b / \langle \bar{v}_{b\infty} \rangle$) at (a,d) $y/D = 0.65$; (b,e) 1.5; (c,f) 2.5 behind the cylinder of $D = 20$ mm (a-c) and 30 mm (d-f): \square , $\langle \bar{\alpha} \rangle = 0.003$; \triangle , 0.009; \diamond , 0.011; \circ , 0.021.



(a)



(b)

Figure 3.16. (a) Scaling relation between mean bubble rise velocity and $\langle \bar{\alpha} \rangle$: \circ , measured at upstream; \triangle , outside of the nearwake ($|x/D| > 0.5$) for $D = 20$ mm; \square , $D = 30$ mm. (b) Variations of spatially-averaged (absolute) bubble rise velocity with $\langle \bar{\alpha} \rangle$. \times , present study; ∇ , Zenit et al. (2001); \circ , Risso & Ellingsen (2002); \triangle , Martínez-Mercado et al. (2007); \triangle , Riboux et al. (2010); \blacktriangledown , Colombet et al. (2011); \bullet , Colombet et al. (2015).

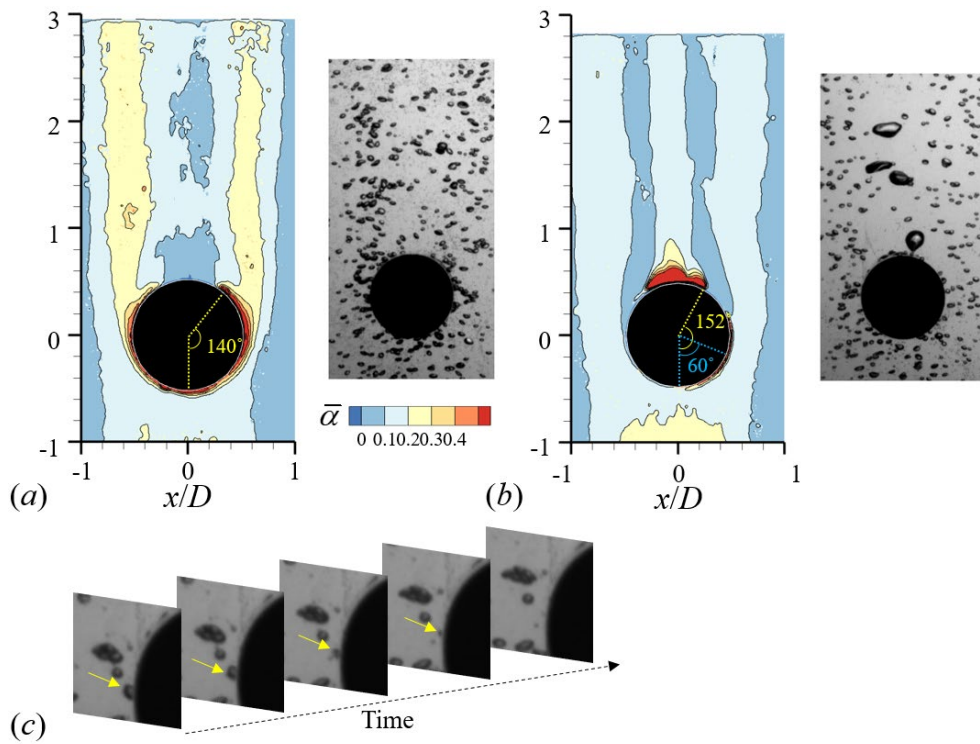


Figure 3.17. (a) Contours of time-averaged in-focus bubble distributions in the hydrophilic cylinder wake (whose diameter is 30 mm, and contact angle is 60°); (b) hydrophobic cylinder wake (30 mm, 140°); (c) time sequence (dt of 1 ms) of instantaneous images showing a bubble trapping into the grooves of the hydrophobic cylinder. In each contour, we highlighted angles at which the maximum mean void fraction is developed.

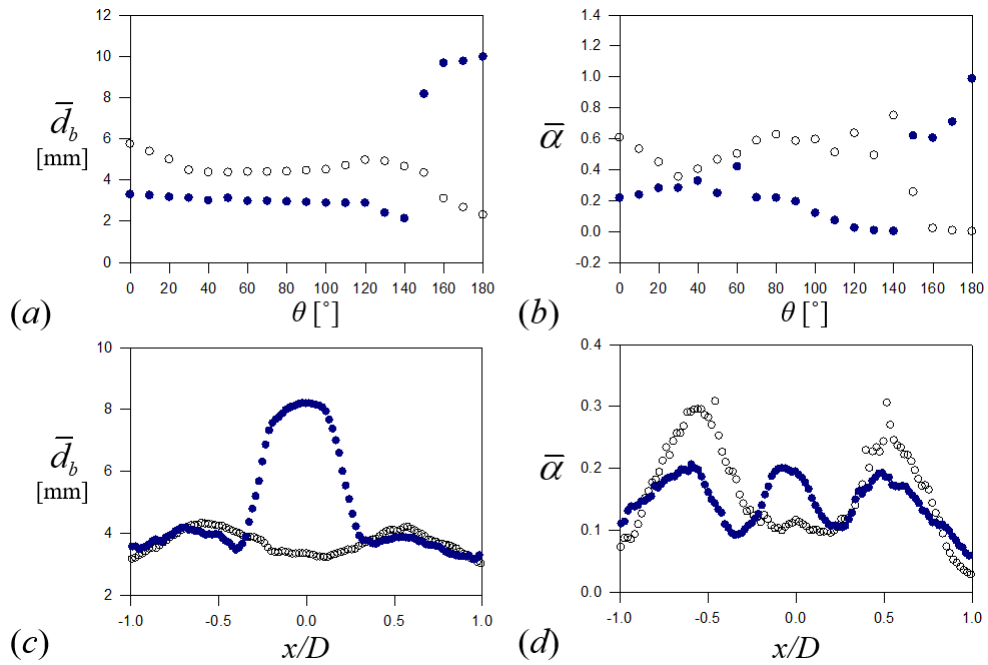


Figure 3.18. (a,b) Gas-phase statistics along the circumferential direction of the cylinder (D of 30 mm); (c,d) in the cylinder wake ($y/D = 1$); (a,c) mean bubble size; (b,d) mean void fraction: \circ , hydrophilic cylinder; \bullet , hydrophobic cylinder. Here, 0° coincides with the front stagnation point.

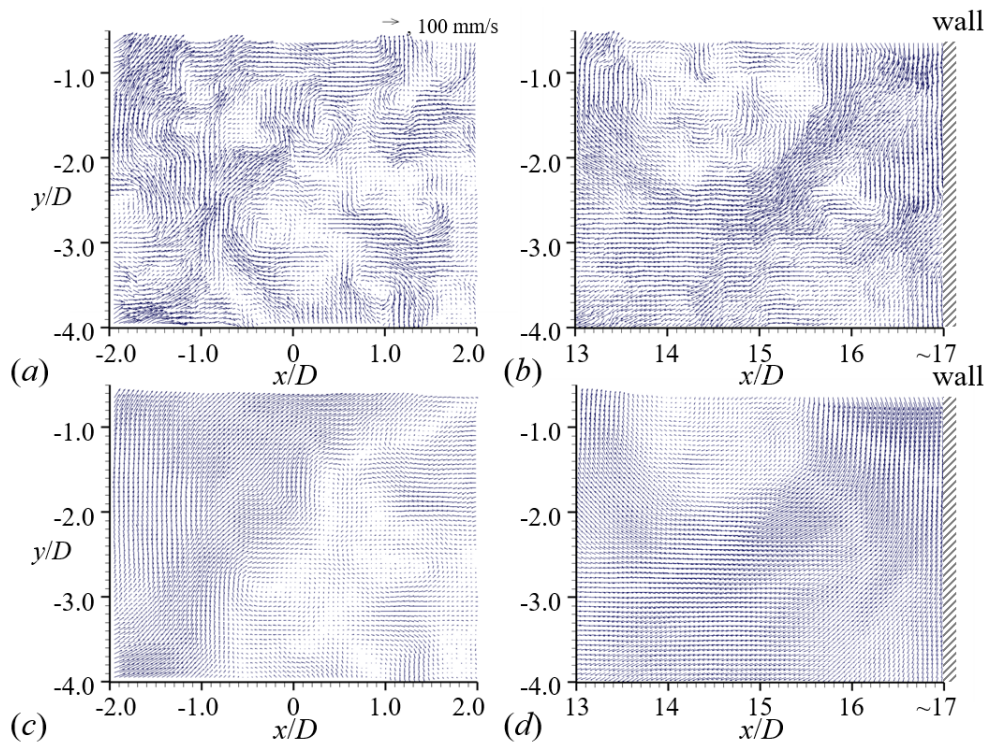


Figure 3.19. (a,b) Instantaneous and (c,d) time-averaged liquid velocity fields behind a homogeneous bubble-swarm at upstream ($\langle \bar{\alpha} \rangle = 0.011$) measured at (a,c) the core region ($|x/D| < 2.0$); (b,d) near the sidewall ($13 < |x/D| < 17$). It is worth noting that the calculated velocity fields are the direct results of the PIV estimation without any post-processing algorithm to suppress the erroneous vectors.

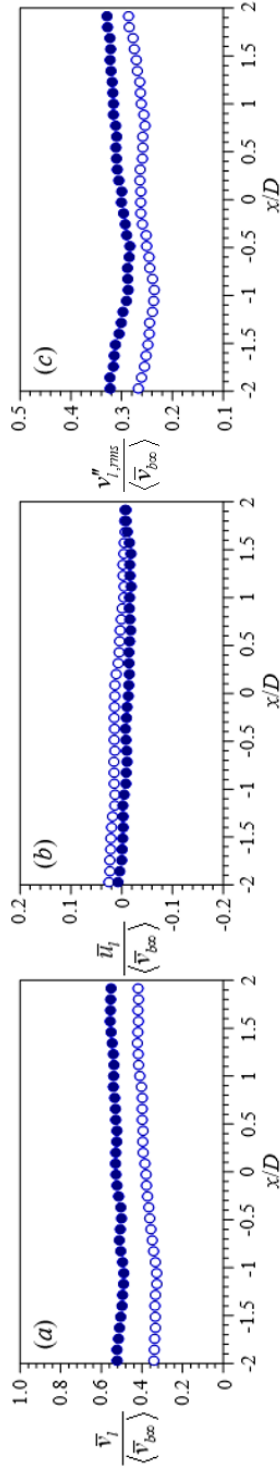


Figure 3.20. Upstream ($y/D = -1.5$) bubble-induced liquid flow: (a) mean streamwise velocity (\bar{v}_t); (b) mean transverse velocity (\bar{u}_t); (c) root-mean-square of streamwise velocity fluctuation ($v''_{t,rms}$); \circ , $\langle \bar{u} \rangle = 0.006$; \bullet , 0.011 .

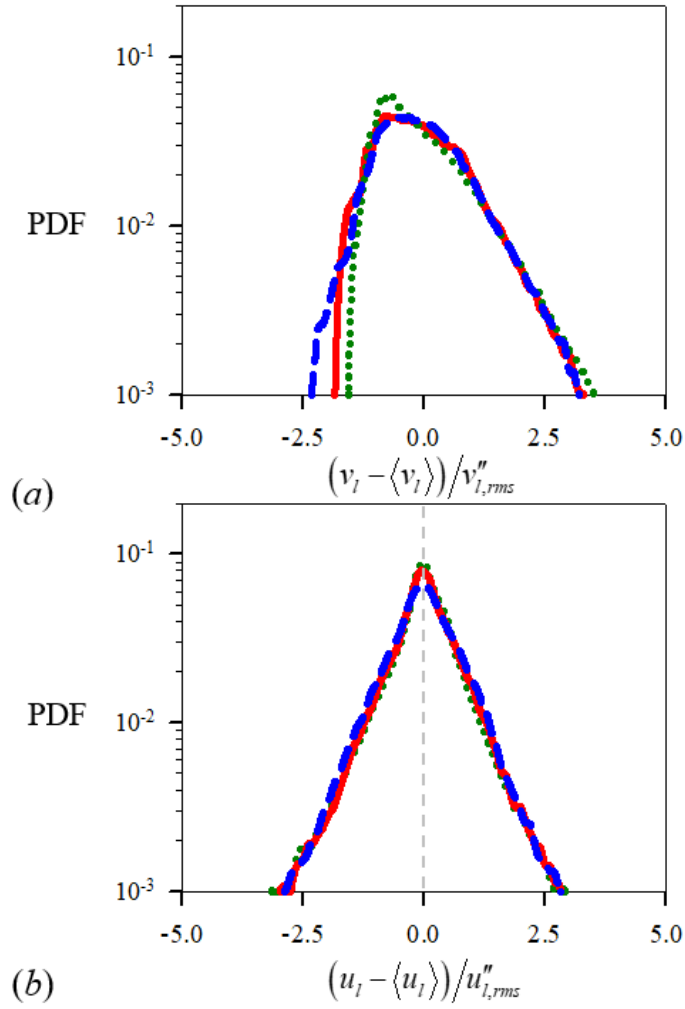


Figure 3.21. Probability density functions (PDFs) of liquid-phase velocity in (a) streamwise and (b) transverse components, measured at the upstream of the circular cylinder.

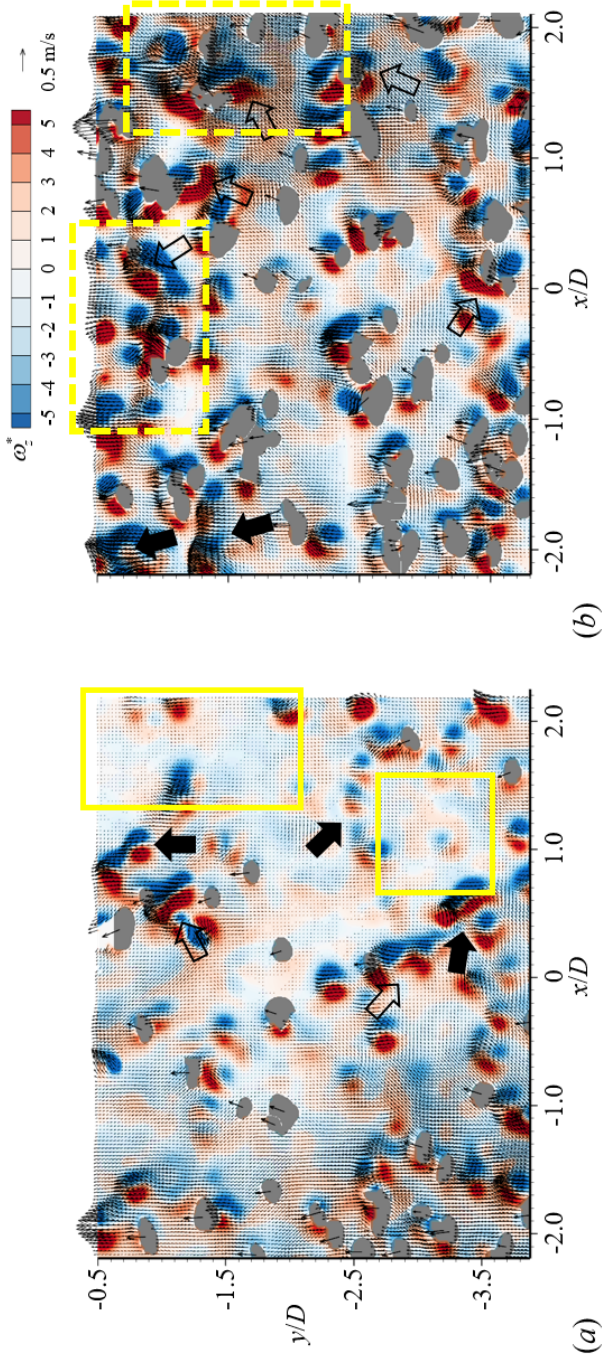


Figure 3.22. Instantaneous two-phase flow fields with velocity vectors and contour of normalized spanwise vorticities ($\omega_z^* = \omega_z D / \langle \bar{v}_{b, \infty} \rangle$) at upstream: (a) $\langle \bar{\alpha} \rangle = 0.006$; (b) 0.011 . Bubbles that are located on and in front of the $z/D = 0$ plane are shown.

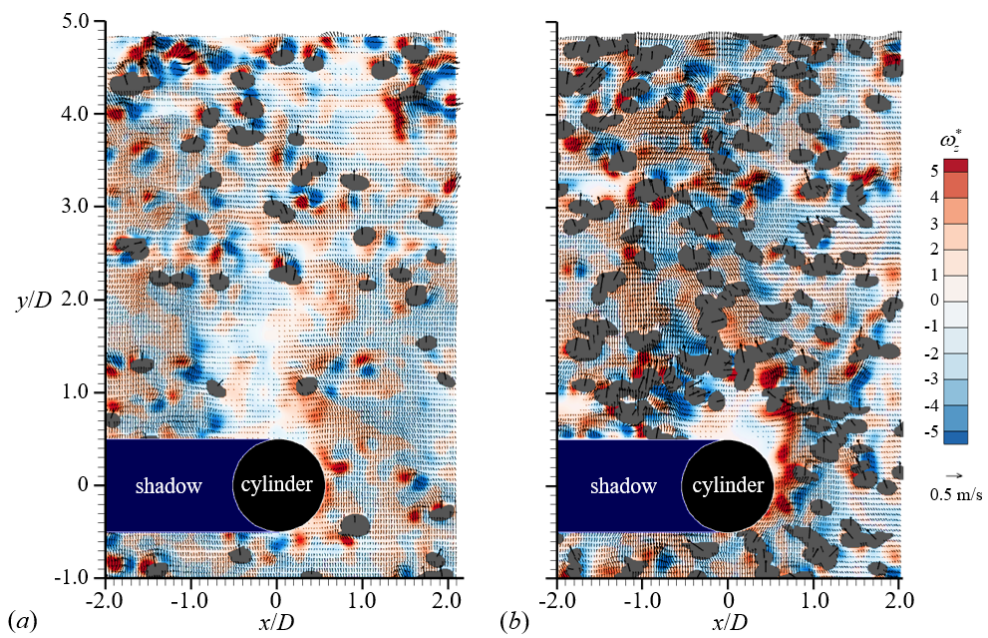


Figure 3.23. Instantaneous two-phase flow around a circular cylinder ($D = 20$ mm): (a) $\langle \bar{\alpha} \rangle = 0.006$; (b) 0.011. Bubbles that are located on and in front of the $z/D = 0$ plane are shown.

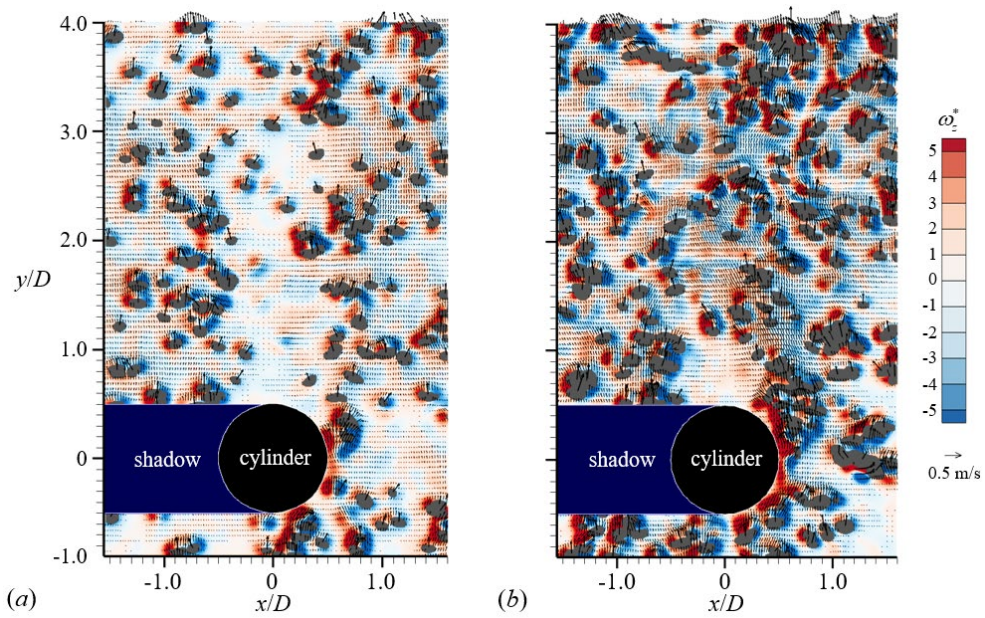


Figure 3.24. Instantaneous two-phase flow around a circular cylinder ($D = 30$ mm): (a) $\langle \bar{\alpha} \rangle = 0.006$; (b) 0.011. Bubbles that are located on and in front of the $z/D = 0$ plane are shown.

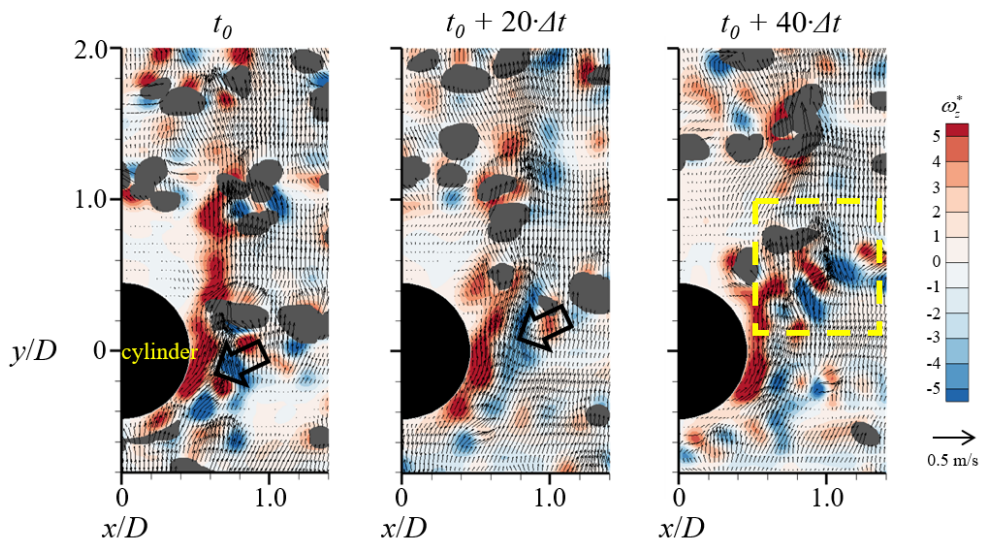


Figure 3.25. Temporal evolution ($\Delta t = 1$ ms) of the instantaneous separating liquid shear-layer in two-phase flows.

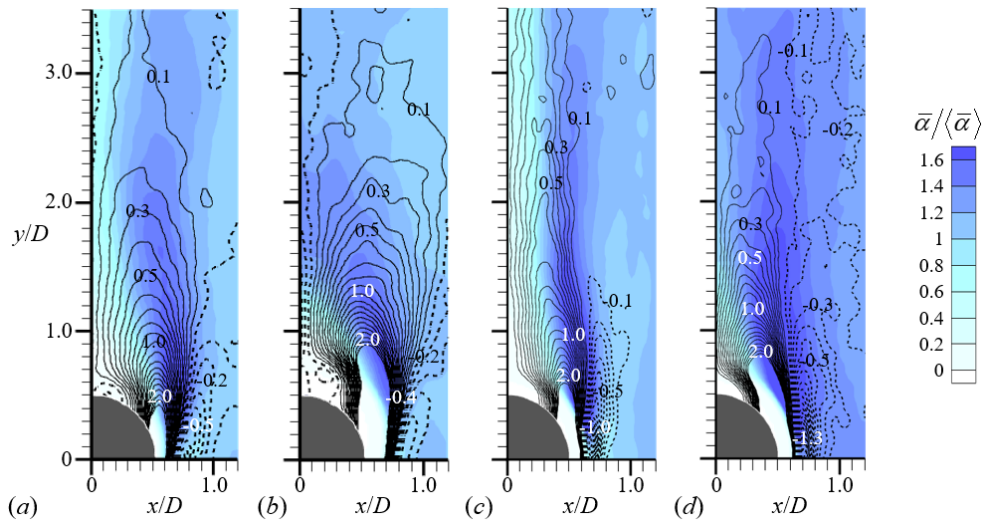


Figure 3.26. Contours of normalized local void fraction, $\bar{\alpha}/\langle \bar{\alpha} \rangle$ (flood) and normalized spanwise vorticity, $\bar{\omega}_z^*$ (line) in the wake behind the cylinder of (a,b) $D = 20$ mm and (c,d) 30 mm: (a,c) $\langle \bar{\alpha} \rangle = 0.006$; (b,d), 0.011. Here, the line contour levels are set in the increments of 0.1, and dashed lines denote negative value.

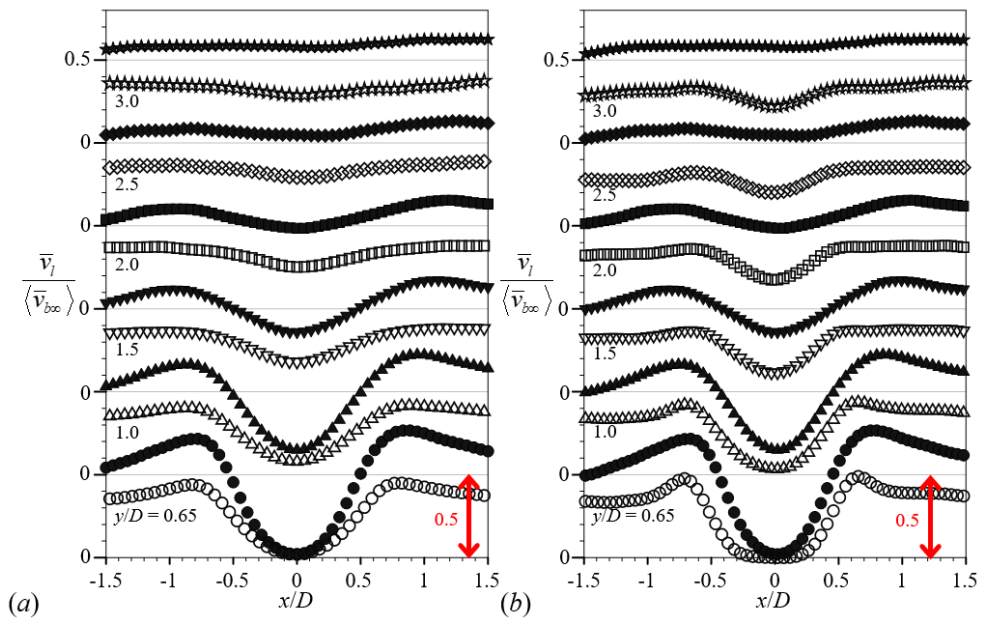


Figure 3.27. Transverse distributions of the mean streamwise velocity (\bar{v}_l) in liquid phase in the wake behind a cylinder: (a) $D = 20$ mm; (b) 30 mm; (open-symbol) $\langle \bar{\alpha} \rangle = 0.006$, (closed) 0.011; \circ , $y/D = 0.65$; \triangle , 1.0; ∇ , 1.5; \square , 2.0; \diamond , 2.5; \star , 3.0.

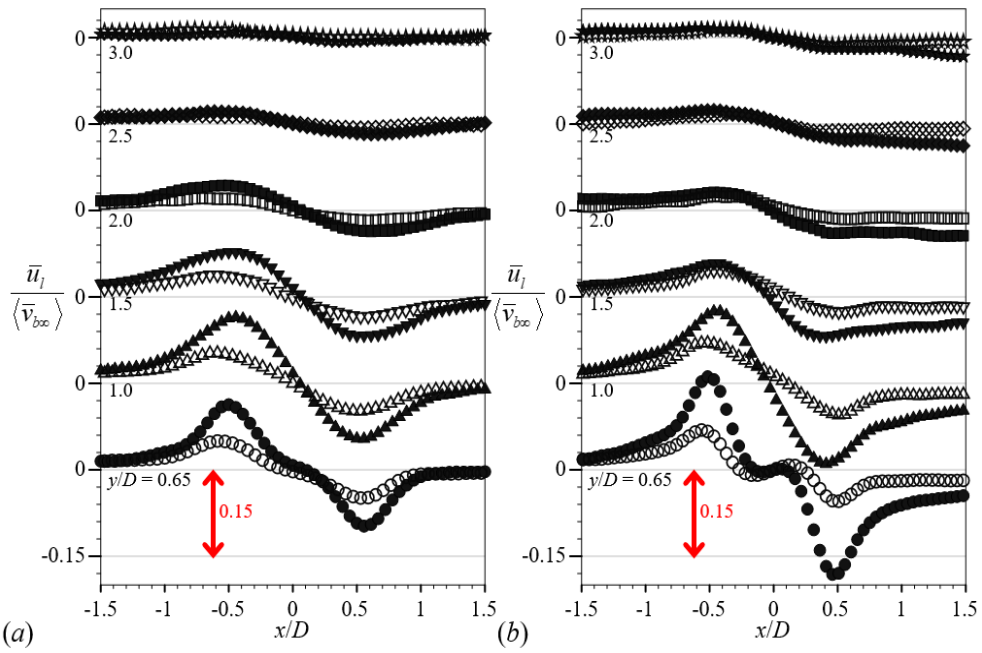


Figure 3.28. Transverse distributions of the mean transverse velocity (\bar{u}_t) in liquid phase in the wake behind a cylinder: (a) $D = 20$ mm; (b) 30 mm; (open-symbol) $\langle \bar{\alpha} \rangle = 0.006$, (closed) 0.011; \circ , $y/D = 0.65$; \triangle , 1.0; ∇ , 1.5; \square , 2.0; \diamond , 2.5; \star , 3.0.

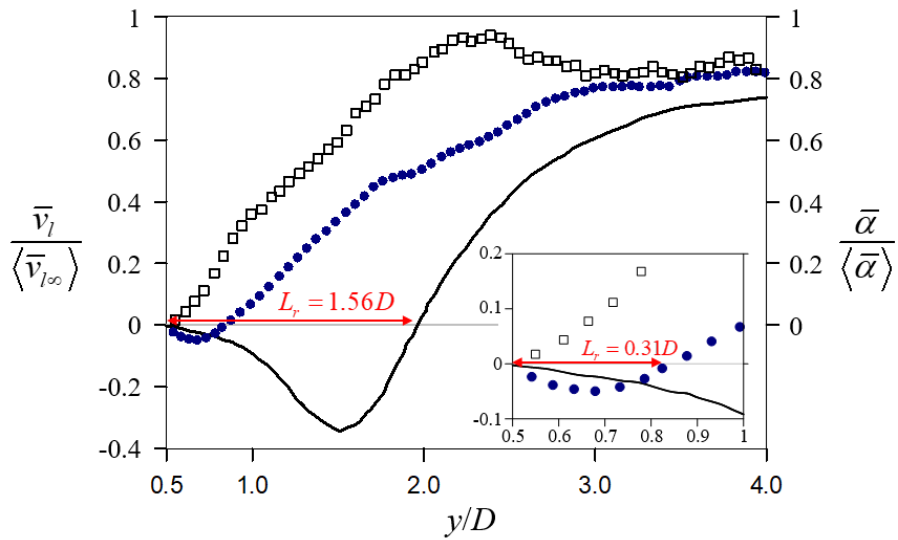


Figure 3.29. Streamwise variations of the normalized bubble-induced mean liquid velocity (●) and local void fraction (□) in the wake behind the cylinder ($Re_D = 2,400$ where D of 20 mm) with $\langle \bar{\alpha} \rangle = 0.006$. A solid-line denotes the mean liquid velocity in the single-phase flow ($Re_D = 3,900$) (Parnaudeau et al. 2008), here L_r denotes the recirculation bubble size and a solid-line.

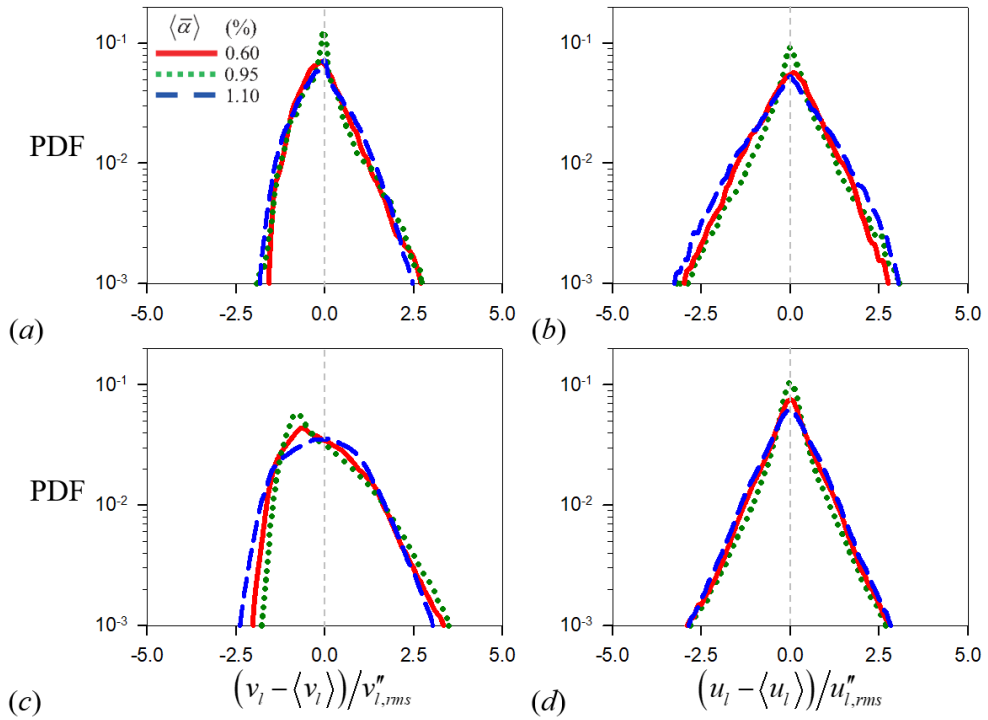


Figure 3.30. Probability density functions (PDFs) of the liquid-phase velocity in (a,c) streamwise and (b,d) transverse directions, (a,b) measured in the wake behind the circular cylinder ($|x/D| \leq 0.5$ and $0.5 \leq y/D \leq 3.0$) and (c,d) outside of the wake ($|x/D| > 0.5$).

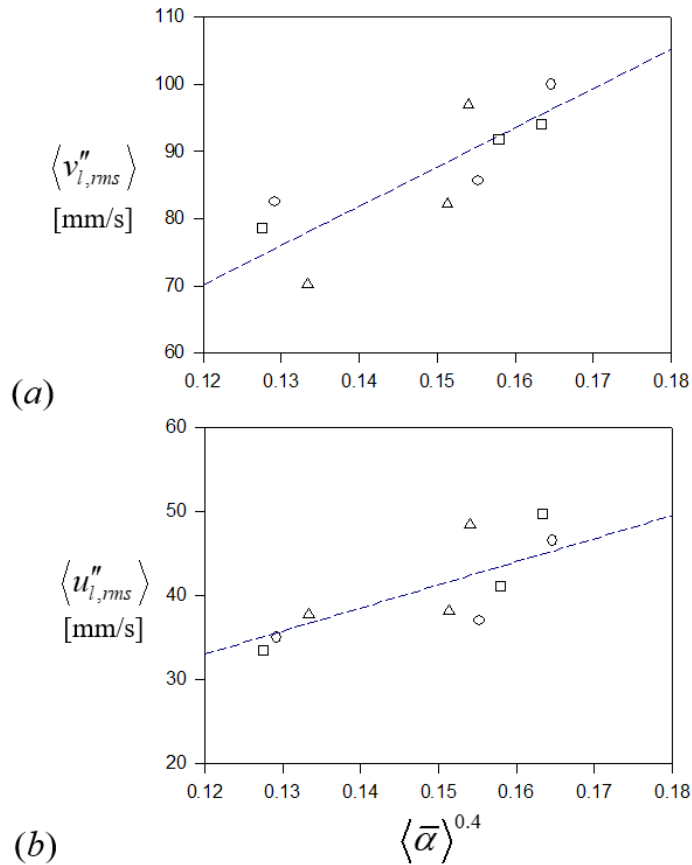


Figure 3.31. Scaling relation between bubble-induced liquid velocity fluctuation and $\langle \bar{\alpha} \rangle$: (a) streamwise velocity fluctuation; (b) transverse velocity fluctuation: \circ , fluctuation measured at upstream; \triangle , outside of the nearwake ($|x/D| > 0.5$) behind the cylinder with D of 20 mm; \square , 30 mm.

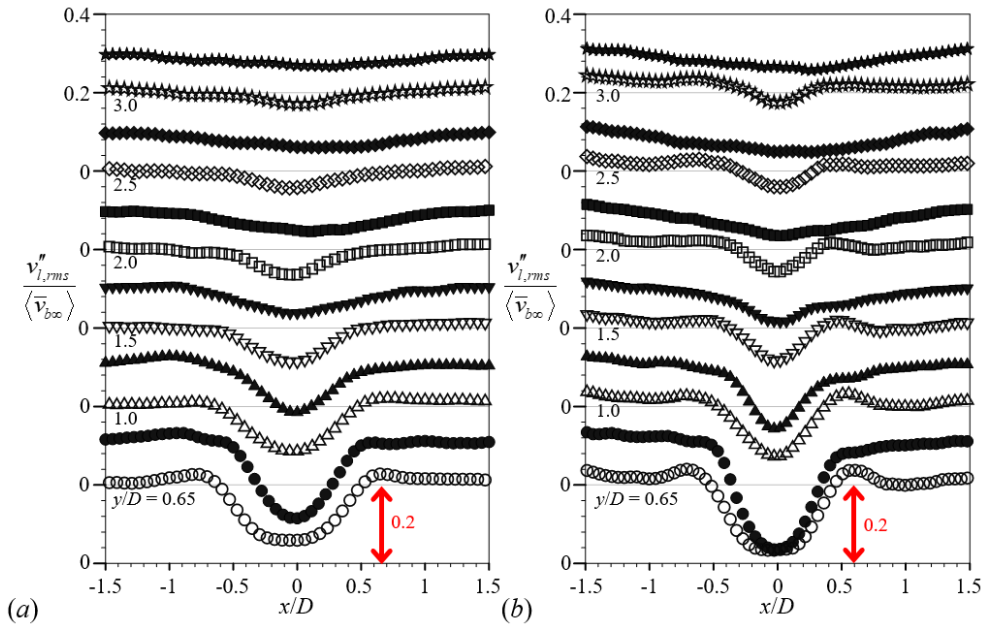


Figure 3.32. Transverse distributions of the root-mean-square of streamwise velocity fluctuation ($v''_{l,rms}$) in liquid phase in the wake behind a cylinder: (a) $D = 20$ mm; (b) 30 mm; (open-symbol) $\langle \bar{\alpha} \rangle = 0.006$, (closed) 0.011; \circ , $y/D = 0.65$; \triangle , 1.0; ∇ , 1.5; \square , 2.0; \diamond , 2.5; \star , 3.0.

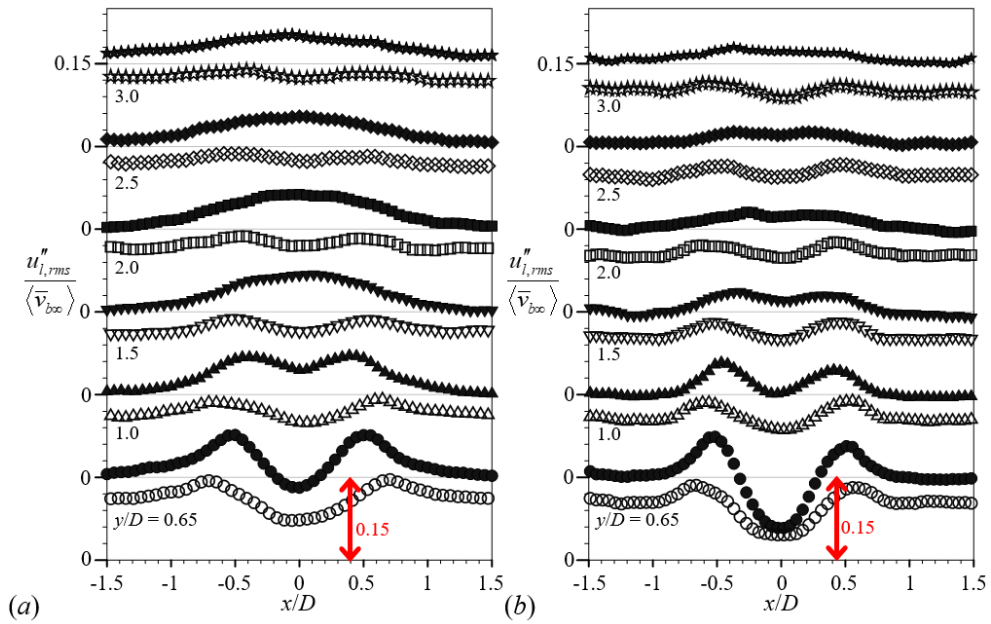


Figure 3.33. Transverse distributions of the root-mean-square of transverse velocity fluctuation ($u''_{l,rms}$) in liquid phase in the wake behind a cylinder: (a) $D = 20$ mm; (b) 30 mm; (open-symbol) $\langle \bar{\alpha} \rangle = 0.006$, (closed) 0.011; \circ , $y/D = 0.65$; \triangle , 1.0; ∇ , 1.5; \square , 2.0; \diamond , 2.5; \star , 3.0.

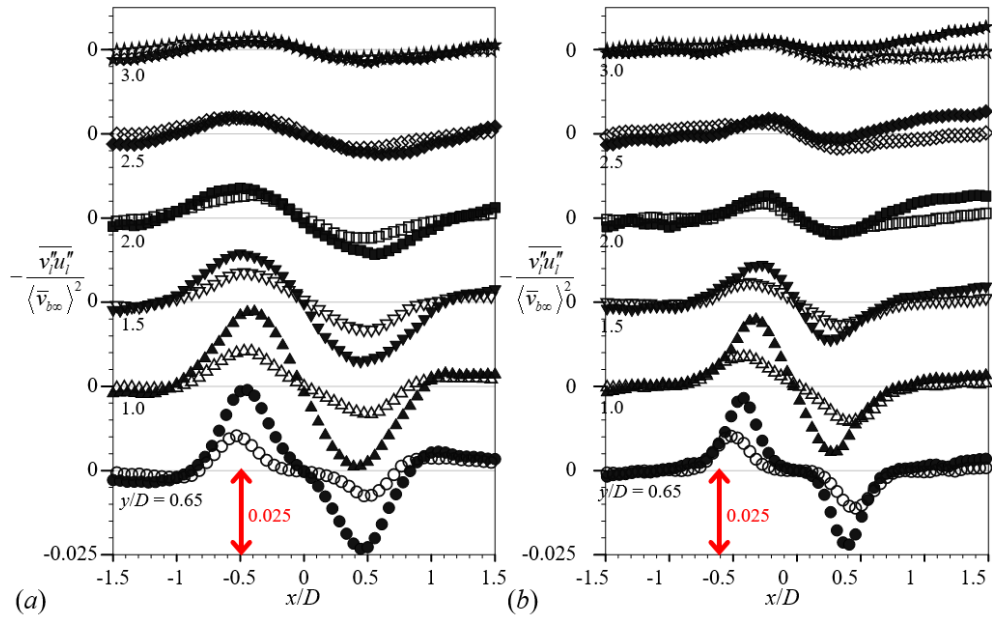


Figure 3.34. Transverse distributions of the turbulent stress ($-\overline{v_i''u_j''}$) in liquid phase in the wake behind a cylinder: (a) $D = 20$ mm; (b) 30 mm; (open-symbol) $\langle \bar{\alpha} \rangle = 0.006$, (closed) 0.011; \circ , $y/D = 0.65$; \triangle , 1.0; ∇ , 1.5; \square , 2.0; \diamond , 2.5; \star , 3.0.

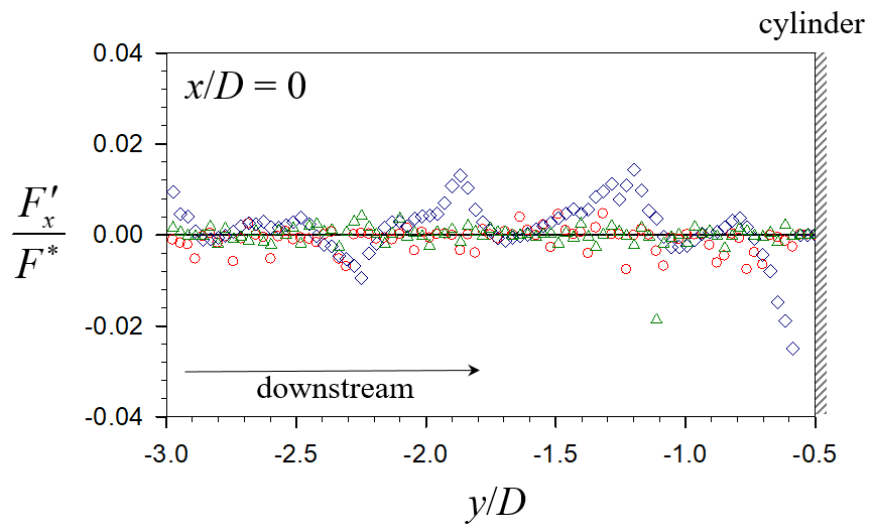


Figure 3.35. Distributions of the lateral force acting on bubbles for $\langle \bar{\alpha} \rangle = 0.0095$ measured at upstream along $x/D = 0$ normalized by the maximum total force measured at downstream $(-0.44D, 0.89D)$: \circ , drag; \diamond , lift; \triangle , turbulent dispersion force.

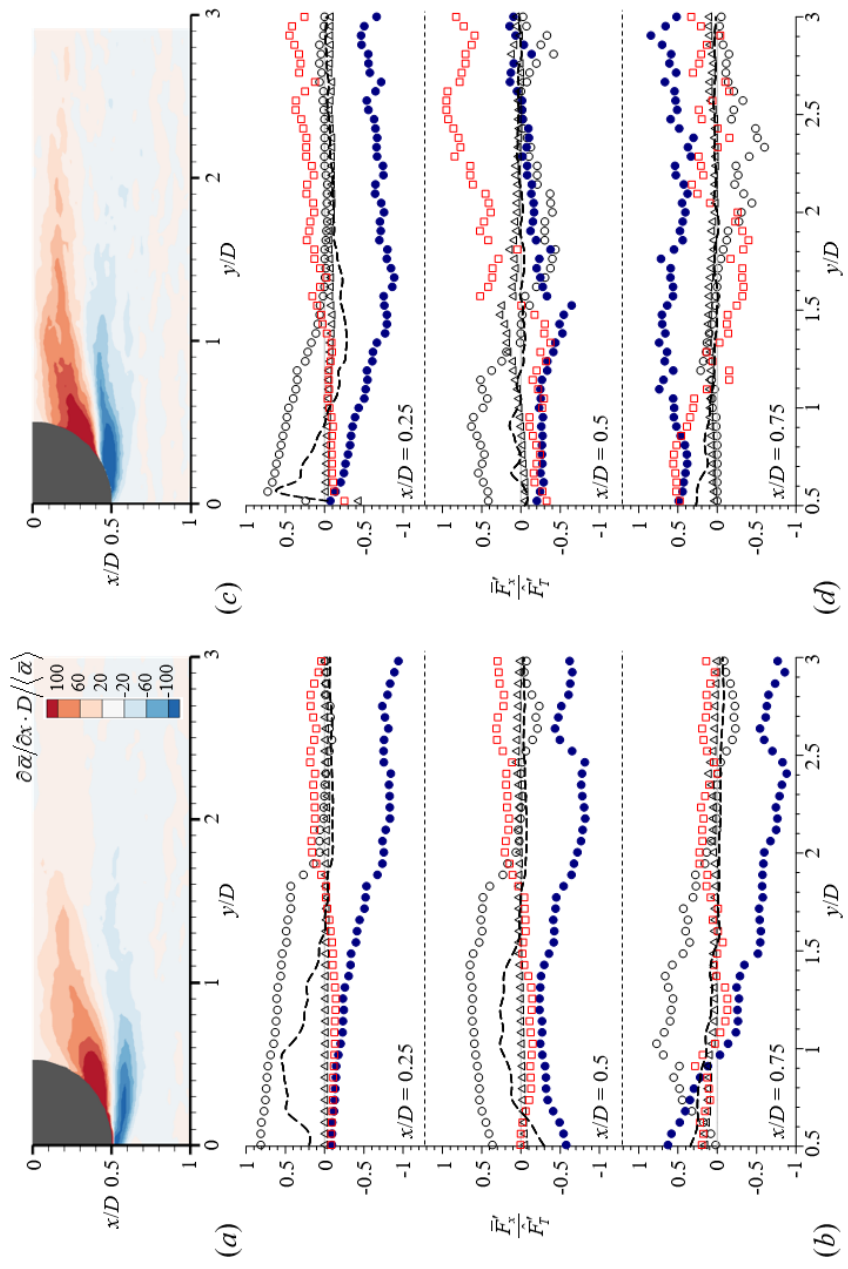


Figure 3.36. (a,c) Contour of normalized transverse gradient of local void fraction ($\partial \bar{\alpha} / \partial x \cdot D / \langle \bar{\alpha} \rangle$). (b,d) Distributions of ratio of lateral force to the summation of the magnitude of each force (\bar{F}_x / \bar{F}_T) acting on bubbles for $\langle \bar{\alpha} \rangle = 0.0095$: (a,b) $D = 20$ mm; (c,d) $D = 30$ mm. \circ , drag; \bullet , lift; Δ , turbulent dispersion force, \square , pressure-gradient and a dashed-line denotes a summation force.

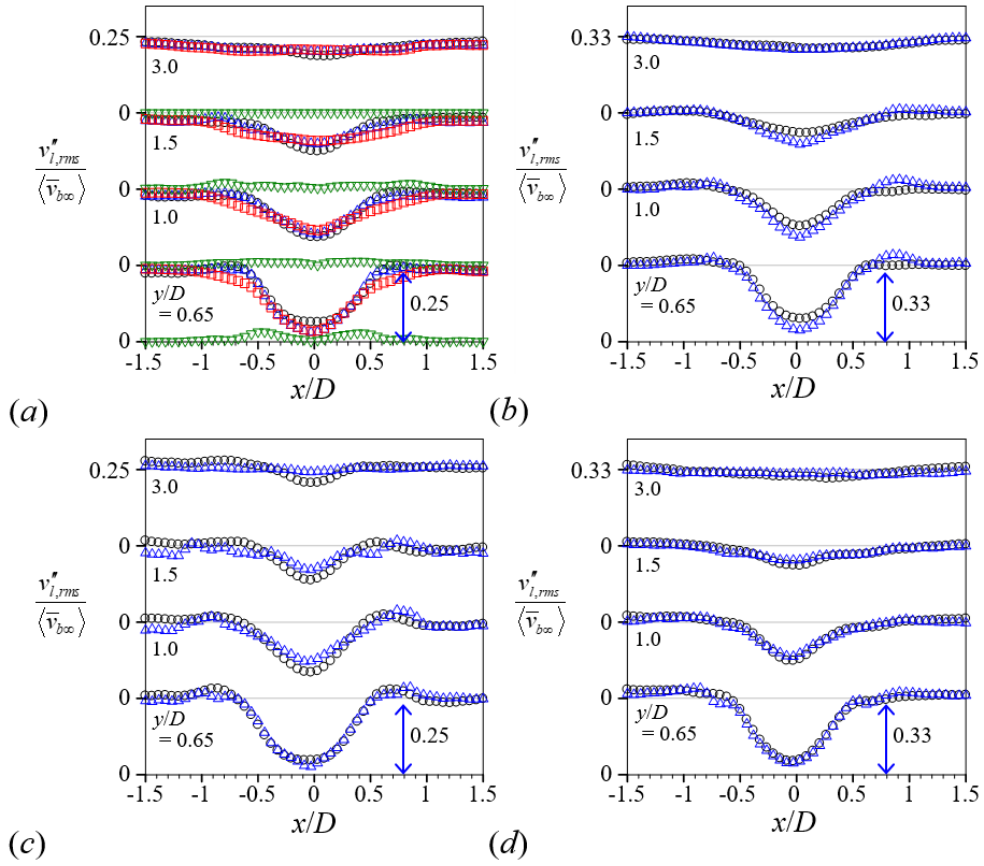


Figure 3.37. Comparison between the modeled (Δ) and measured (\circ) distribution of the streamwise velocity fluctuations in liquid phase behind the cylinders of (a,b) $D = 20$ mm and (c,d) 30 mm: (a,c) for $\langle \bar{\alpha} \rangle = 0.006$; (b,d) 0.011. Here, we decomposed the contributions by the pure bubble-induced turbulence (\square) and by the redistributed bubbles by the cylinder (∇) in equation 2.24.

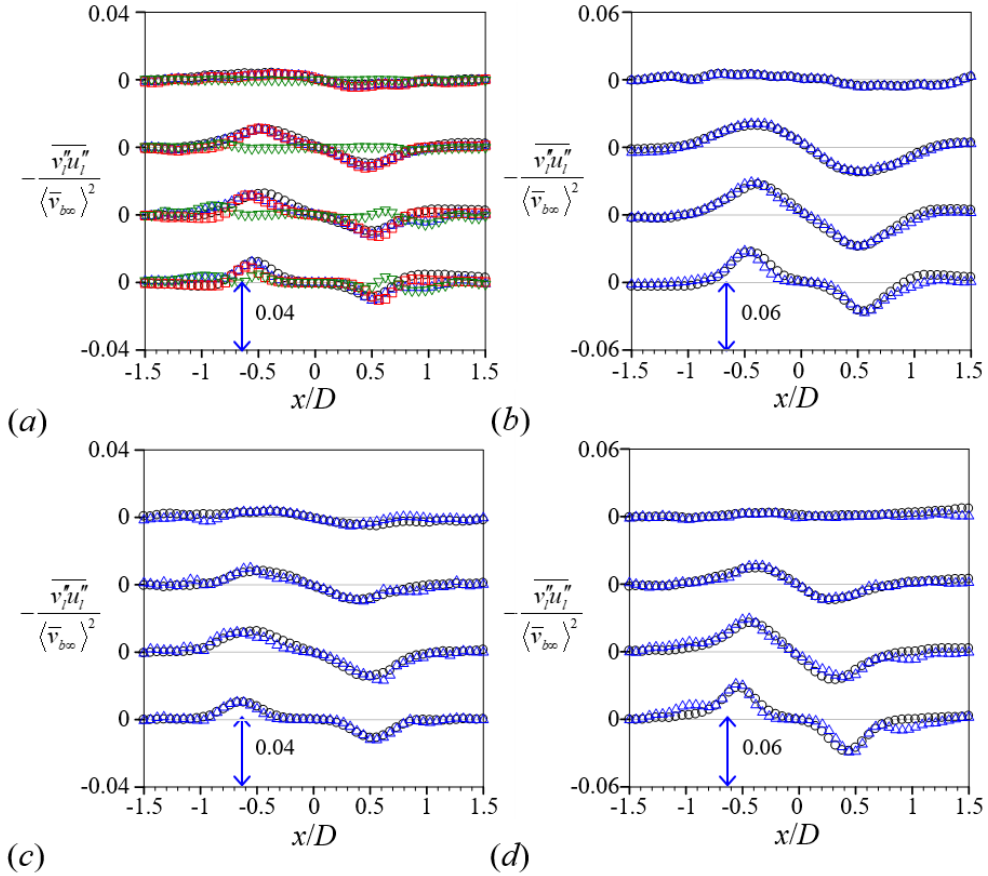


Figure 3.38. Comparison between the modeled (Δ) and measured (\circ) distribution of the bubble-induced turbulent stress in liquid phase behind the cylinders of (a,b) $D = 20$ mm and (c,d) 30 mm: (a,c) for $\langle \bar{\alpha} \rangle = 0.006$; (b,d) 0.011. Here, we decomposed the contributions by the inviscid flow (\square) and by the redistributed bubbles by the cylinder (∇) in equation 2.29.

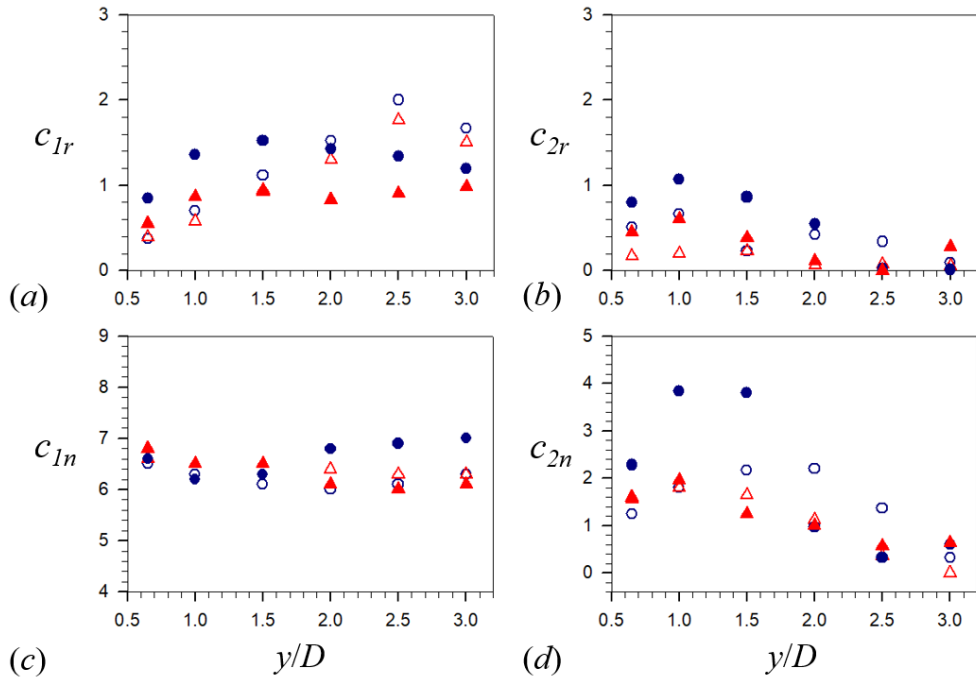


Figure 3.39. (a,b) Evolution of resultant prefactors of the bubble-induced Reynolds stress model (c,d) those of the streamwise liquid fluctuation model along downstream. \circ , D of 20 mm for $\langle \bar{\alpha} \rangle = 0.006$; \triangle , 20 mm, 0.011; \bullet , 30 mm, 0.006; \blacktriangle , 30 mm, 0.011.

Chapter 4.

Application of the developed model to laminar and turbulent bubbly pipe (channel) flows

4.1 Turbulent nature of the BIT

We now proceed to validate the developed models for bubbly internal flows. In many gas-liquid two-phase flow applications (e.g., heat- and mass-transfer and transportation, to name but a few), a gas-liquid mixture must be conveyed in a confined channel (pipe), which means that the initial conditions for liquid-phase do not static, i.e., $j_i > 0$, and boundary layers at the wall could significantly modify the typical characteristics of the bubble-agitated turbulence (e.g., nonlinear interactions between shear-induced turbulence and BIT). Therefore, the aforementioned models in a liquid initially at rest (equations 2.24 and 2.29) do not relevant here anymore. Consequently, based upon this (dynamic) environment, we have proposed a model for the bubble-induced streamwise liquid fluctuation (equations 2.35) and turbulent stress (equations 2.40) respectively in the framework of the two-phase mixing-length theory (equations 2.12). Before we independently validate the developed models in laminar and turbulent bubbly flows available in the literature (table 2.1), we have confirmed whether the fluctuating nature of the pure bubble-induced turbulence is still dominant in the confined channel at a high bulk Reynolds number ($Re_D = 44,000$), especially near the wall-region (figures 4.1c-d) (Lee et al. 2021).

When a homogeneous bubble-swarm rises in quiescent liquid, it agitates surrounding liquid to have a typical asymmetric profile with positive skewness in the PDF of the liquid fluctuation in the streamwise direction, exhibiting exponential tails (linear evolution on the semilog-axes), while it is not for the transverse direction that a rather symmetric shape centered at the origin is observed, regardless of the $\langle \bar{\alpha} \rangle$ (Risso 2016). Although most of the turbulent energy is generated by the temporal wakes' interactions (Riboux et al. 2013; Amoura et al.

2017), the asymmetric shape of the PDF in streamwise direction is predominantly originated by an inviscid flow and the spatial fluctuations (an averaged-wake) in the vicinity of bubbles (Risso 2016). Taking all the self-similar properties of BIT into account, the bubble-induced liquid fluctuation is evolved as $V_0 \langle \bar{\alpha} \rangle^{0.4}$ in the absence of SIT. This relation is applicable up to $\langle \bar{\alpha} \rangle$ of 0.14 (Martínez-Mercado et al. 2007; Roig & de Tournemine 2007; Riboux et al. 2010). Interestingly, this tendency is also observed when the low Reynolds number bubble-induced mean liquid flow ($Re_d \sim 2,000$, where the diameter of the cylinder (d) is 20 mm) passes around the circular cylinder, even inside the cylinder wake ($|x/d| \leq 0.5, 0.5 \leq y/d \leq 3.0$) (figures 4.1a-b) (Lee & Park 2020) as well as the core-region ($|xD| \leq 0.1$, where D of 40 mm) of the turbulent pipe flows with $Re_D = 44,000$ (figures 4.1c-d) (Lee et al. 2021). However, when an intense turbulence modification ($\Delta v_i''$) by the gradient of the mean liquid velocity (e.g., boundary-layer at sidewalls in pipes) occurs, such characteristics are more or less modified. For example, in the streamwise direction, positive fluctuations are slightly more pronounced near the wall ($0.38 \leq xD \leq 0.4$) compared to the Gaussian-curve with zero-skewness (figure 4.1c) because the ascending bubble rise motions are decelerated by the wall interference, but the PDF remains nearly Gaussian for negative and more probable values, while in the transverse direction, the typical features of BIT are maintained but the tail of the PDF more fluctuates at the large liquid perturbation parts (figure 4.1d). It has been shown by Riboux et al. (2010) that the exponential tails are mainly due to the agitation produced by the wakes interaction. However, in turbulent bubbly flows, turbulence in the flow does not result solely from the complicated interactions of the detached wake structures distributed over the entire-domain, since the incident turbulence may play a role as well (Alm eras et al. 2017). A detailed mechanism for the modification of BIT, when surrounded by external turbulence, is described in the Alm eras et al. (2017) and Lee et al. (2021). Here, we emphasize that the turbulent nature of the BIT is modified depending on flow geometries, thus such scaling ($v_i'' \sim V_0 \langle \bar{\alpha} \rangle^{0.4}$) alone is insufficient to completely estimate the spatially-varying turbulence quantities especially in

laminar and turbulent bubbly pipe flows. In this context, we justify the necessity of quantifying the additional turbulence modulation ($\Delta v_l''$) by incident turbulence, magnitudes of which may vary depending on the bulk liquid Reynolds number (Re_D) and flow configurations.

Nevertheless, in the case when the bubble-induced turbulence is surrounded by external turbulence (e.g., shear-induced turbulence and grid-turbulence as well), the positive skewness, i.e., asymmetric profile, of the PDF in the streamwise direction and zero-skewness for transverse direction centered at the origin are both observed experimentally near the wall-region for different operating conditions (figures 4.1c-d) and these are known to be the signature of the bubble wakes (Risso & Ellingsen 2002; Riboux et al. 2010; Risso 2016, 2018), meaning that, although there must exist a turbulence modification ($\Delta v_l''$) by the wall-generated turbulence to some extent, the bubble-induced turbulence cannot be neglected, rather it seems more influential than other turbulence sources including interactions between the BIT and incident turbulence. Classically, these interactions have been neglected (this is our case) (Lance & Bataille 1991), and isolating (quantifying) them is harsh to perform, except the works by du Cluzeau et al. (2019) where a direct numerical simulation (DNS) for turbulent bubbly flows is systematically conducted. A brief discussion on this issue and our response are shown below.

4.2 A short comment on the nonlinear interaction by external turbulence

As previously mentioned, the complex interaction between BIT and external turbulence is classically neglected (Lance & Bataille 1991) even if several phenomena, such as turbulence suppression, are in contradiction with this hypothesis. To the best of our knowledge, du Cluzeau et al. (2019) first quantified the degree of the interaction in turbulent bubbly pipe flows by extracting single-phase turbulence in two-phase equivalent (with mono-dispersed deformable bubbles) and compare the residue to the reference single-phase turbulence. It turns out that non-negligible turbulence attenuation has occurred, and it is intensified away from the sidewalls, i.e., near the core-region, where large deformable bubbles

are populated, while near the wall-region in the absence of bubbles, the turbulent boundary layer then freely develops such that the classical large-scale streaks of the wall-generated turbulence are retained as in the single-phase flow, which is also materialized (see figure 5 in du Cluzeau et al. 2019). However, an identifying mechanism on which the observed phenomena is based still remains to be uncovered to date, nevertheless, in very near-wake ($|x/D| > 0.4$), none of the turbulence enhancement (and also suppression) has occurred. In real physics where various-sized bubbles exist, smaller spherical bubbles tend to accumulate near the wall-region while larger deforming ones at the core-region (Hibiki & Ishii 2007), both of which exhibit quite a random trajectory, meaning that turbulence could be enhanced and also suppressed at any region with similar possibilities. In this regard, considering the recent understanding in the community, neglecting the uncovered interactions which seem to be distributed over the entire-domain at small extents is not that absurd, and we have no choice but to follow this attribute. In the community, it is also plausible that cross-correlation between the BIT and incidence turbulence is zero, i.e., $\overline{u'_i u''_i} = 0$ (Lance & Bataille 1991). It is worth mentioning that although we have neglected the aforementioned mutual interactions that exist in context, the proposed models (equations 2.35 and 2.40) without them faithfully predict the measured (total) turbulence both at the core- and near wall-region of pipes for wider ranges of the volume void fraction (< 0.1) and bulk Reynolds number ($\sim \mathcal{O}(10^4\text{-}10^5)$), which would be shown later.

4.3 Prefactor optimization

In the developed bubble-induced turbulence models, we are fully aware that the existence of tuning parameters seriously impairs the potential applicability in the two-fluid RANS simulation. Nevertheless, as an example, we found optimal coefficients (c_n) in the v''_i model using the least-square method and compared the prediction result with the experimental work by Liu & Bankoff (1993) as shown in figure 4.3(▼-symbol). Here, the proposed model shows excellent prediction performance at both core- and near wall-region of the turbulent bubbly pipe flow

($Re_D = 14,288$). However, varying the constants from case to case to fit the experimental data is irrelevant, thus we check the variability of the prefactors (c_{1n} , c_{2n} , and c_{3n} in equation 2.35 and c_{1r} and c_{2r} in equation 2.40) which are empirically found by the least-square method with increasing $\langle \bar{\alpha} \rangle$ (figure 4.2).

Since we have developed the pure BIT models (equations 2.35 and 2.40), all the coefficients tend to evolve linearly with increasing the volume void fraction. Especially for the v_l'' (figure 4.2a), as the number of bubbles increase in the system ($\langle \bar{\alpha} \rangle < 0.1$), the inviscid drift-flow (c_{1n}) in front of bubbles and the steady averaged-wake partially explaining the behavior of c_{2n} , both of which are known to be localized in the close vicinity of the bubbles ($\sim 3 \langle \bar{d}_b \rangle$), become influential, and this is consistent with prior observations (Risso & Ellingsen 2002; Risso 2016, 2018). Of course, the isotropic nature of the temporal fluctuations (e.g., wakes interactions) which is rather homogeneously distributed over the liquid-phase, is evident (Riboux et al. 2013; Amoura et al. 2017), and can also account for the linear evolution of c_{2n} with increasing $\langle \bar{\alpha} \rangle$. Since most of the turbulent energy is generated by temporal wakes' interactions capable of producing k^{-3} subrange alone, c_{2n} exhibits the largest absolute magnitude than the rest of the coefficients. Meanwhile, turbulence modification (c_{3n}) by the gradient of the mean liquid flow ($\Delta v_l'' \sim l_b \cdot |\partial \bar{v}_l / \partial x|$) by the sidewalls is non-negligible and mildly proportional to the volume void fraction. According to own experience (Lee & Park 2020), for an identical configuration, a somehow higher volume void fraction induces faster mean liquid flow, as scaled by $v_r |v_r| \sim (1 - \alpha) 4d_b / 3c_D$ (Ishii & Zuber 1979), thus the destabilization of the mean flow by the redistributed bubbles by the sidewalls in confined bubbly flows is expected to be enhanced with increasing the volume void fraction, which explains the behavior of c_{3n} . Consequently, taking all of these behaviors into account, we linearly approximate each coefficient as:

$$\begin{aligned} c_{1n} &= 54 \langle \bar{\alpha} \rangle - 0.225, \\ c_{2n} &= 200 \langle \bar{\alpha} \rangle - 1.15, \\ c_{3n} &= 11 \langle \bar{\alpha} \rangle - 0.08, \end{aligned} \tag{4.1}$$

where $\langle \bar{\alpha} \rangle$ is the dimensionless volume void fraction averaged in time and space.

The overall behaviors of the prefactors in the predicted $-\rho_l \overline{v_l'' u_l''}$ (equation 2.40) are similar to those in v_l'' , each showing a linear evolution with a milder slope with increasing $\langle \bar{\alpha} \rangle$, and explanations for these behaviors are analogous to those of c_{3n} , except for the cases of c_{2r} in experiments by Kim et al. (2016) and both c_{1r} and c_{2r} by Shawkat et al. (2008) (figure 4.2b). Since the turbulent (shear) stress does not develop in an unbounded homogeneous bubble-swarm, behaviors of all the prefactors (c_{1r} and c_{2r}) here are closely related to the non-uniform distributions of gas-phase statistics (e.g., $\nabla \bar{\alpha}$ and $\nabla \bar{v}_r$) near the wall-region of bounded flows. In this context, the transverse distribution of the local void fraction ($\partial \bar{\alpha} / \partial x$), measured at fully-developed region ($z/D = 42$) in the experiments by Kim et al. (2016), more or less deviates from the typical wall-peaking void distribution (see the figure 7c in that paper), but rather behaves an intermediate-peaking, i.e., a transient state between wall- and core-peaking, thus the contribution of a somewhat steep gradient of the local void fraction ($\partial \bar{\alpha} / \partial x$) in the equation 2.40, responsible for the c_{2r} , is expected to be small. In reality, although the empirically optimized c_{2r} ($= 0.18$) deviates much from the linear-approximation (a dashed-line in figure 4.2b), it does not critically alter the overall prediction performance (equation 2.40) near the wall-region due to the small ($\partial \bar{\alpha} / \partial x$, i.e., $c_{1r} \nabla \bar{v}_r / c_{2r} \nabla \bar{\alpha} \cong 20$). The situation for the abnormal c_r behaviors is quite different in the experiments by Shawkat et al. (2008) in which millimeter-sized bubbles ($\langle \bar{\alpha} \rangle$ of 1.2% with $\langle \bar{d}_b \rangle = 3$ mm) are injected in a vertical pipe (Re_D of 154,000 where D is 200 mm) in which the integral length-scale ($L \sim \mathcal{O}(D/2)$) is much larger than the bubble size ($(D/2) / \langle \bar{d}_b \rangle \cong 33$). Therefore, this configuration is a manifestation of turbulence suppression as a result of nonlinear interactions between BIT and SIT (Serizawa & Kataoka 1990; du Cluzeau et al. 2019; Lee et al. 2021). More specifically, when the liquid flux is relatively high while smaller bubbles are injected into a pipe with a larger diameter, the near-wall turbulence is

reported to be suppressed, compared to the counterpart in the single-phase flow due to the energy damping effect occurring at the bubble interfaces (Serizawa & Kataoka 1990; Kataoka et al. 1993), shortening the classical large-scale wall-induced turbulence streaks (see the figure 5 in the du Cluzeau et al. 2019). Therefore, the data extracted according to our standard (e.g., $v_l'' = v_{l,TP}' - v_{l,SP}'$) in Shawkat et al. (2008) may contain the contribution by non-negligible interactions between BIT and SIT with a high possibility, thus our approach to model the pure BIT itself cannot perfectly represent the experiment data, which can explain the abnormal behaviors of each prefactor (c_{1r} and c_{2r}). Nevertheless, to the best of our knowledge, we have no choice but to adopt this data. As a result, the equations that most closely follow each coefficient are as follow:

$$\begin{aligned} c_{1r} &= 5.6\langle\bar{\alpha}\rangle - 0.0038, \\ c_{2r} &= 1.0\langle\bar{\alpha}\rangle - 0.0667, \end{aligned} \tag{4.2}$$

where $\langle\bar{\alpha}\rangle$ is the dimensionless volume void fraction averaged in time and space. Heretofore, we have developed turbulence models (equations 2.35 and 2.40) in a wall-bounded bubbly flow, and all the prefactors in them are explicitly optimized as a function of the volume void fraction as we intend (equations 4.1 and 4.2). Collecting all the submodels, we have checked the prediction performance of the proposed models by exclusively referring to previous experiments available in the literature.

4.4 Validations and discussions

Heretofore, we have modeled the realistic two-phase mixing-length (equation 2.12) in the presence of neighboring bubbles under the dynamic background liquid-shear and proposed (validated) a scaling law for the mean liquid velocity in bounded bubbly flows (equation 2.17). By combining these with theoretical reasoning, we have proposed the BIT models (equations 2.35 and 2.40) which are equivalent to one-third of the bubble-induced stress tensor. Furthermore, behaviors of each prefactor are discussed and their optimizations are proposed accordingly. Next, we have independently checked the performance of the developed models by

comparing prediction results with prior experimental data available in the literature (figures 4.3 and 4.4).

To begin with, we exclusively selected the maximum volume void fraction case for each reference (table 2.1), except the works by Shawkat et al. (2008) because the aforementioned non-linear interactions between the BIT and external turbulence are dominant in that specific configuration (e.g., $(D/2)/\langle \bar{d}_b \rangle \cong 33$), which becomes more evident with increasing the volume void fraction, thus we choose the minimum volume void fraction, i.e., $\langle \bar{\alpha} \rangle$ of 1.2%. As shown in figure 4.3, the pure bubble-induced streamwise liquid fluctuation in the presence of the bulk liquid flow exhibit a typical core-peaking distribution for laminar (Hosokawa & Tomiyama 2013; Kim et al. 2016) and most of the turbulent flows (Liu & Bankoff 1993; Lee et al. 2021) while a wall-peaking distribution is observed at Shawkat et al. (2008), all of which result from their respective physics. We will not go into a deep discussion on these differences because it is beyond our scope, but we suspect that the smaller-sized (compared to the diameter of the pipe (channel)) bubble-agitated flow is modified by the wall-generated turbulence ($L \sim \mathcal{O}(D/2)$) instantaneously, resulting in a turbulence attenuation which is known to be more pronounced at the core-region of the pipe (du Cluzeau et al. 2019). This may contribute to the wall-peaking distribution of v_1'' in that configuration. However, near the wall-region ($|x/D| \geq 0.4$) (Lee et al. 2021) where the aforementioned interactions are less significant, the negative v_1'' values, i.e., turbulence suppression, is originated from the fragmentation of flow structures generated by bubbles into smaller ones, which is also materialized in du Cluzeau et al. (2020), inferring that bubbles rising near the wall are not capable of generating flow structures strong enough to induce the energy-containing motions, but rather they are more likely to be attenuated near the wall (Re_D of 44,000).

In general, the proposed model for the streamwise liquid fluctuation (equation 2.35) reasonably predicts the experimental data both at the core- and near the wall-region for laminar and turbulent bubbly flows among the considered references (figure 4.3). Both the absolute magnitudes, corresponding locations, and the

transverse distributions of v_i'' are faithfully followed by the model. Especially for laminar bubbly flows, an average accuracy exceeds 80%, which is among the previous studies most superior. Furthermore, both turbulence enhancement and suppression by bubbles are reasonably predicted enough to be utilized in the two-fluid large-scale Reynolds-averaged Navier-Stokes (RANS) simulation. However, the deviation ($\Delta v_i''$) between the predictions and experimental data is obvious at Liu & Bankoff (1993), maintaining this difference as approximately 0.02 m/s both at the core- and near wall-region, which is originated from the magnification error in the process of the linear-approximation of optimized prefactors, compared to those (\blacktriangledown -symbol) tuned by the least-square method, meaning that a bit higher coefficient (c_n) is constantly determined by the equation 4.1 (figure 4.2a). Nevertheless, for the potential applicability of the proposed model, we reasonably decide to adopt these linear approximations for c_n at the cost of sacrificing the accuracy. However, we judge that the prediction performance of the proposed model (equation 2.35) is still reasonable. Likewise, in our model for the bubble-induced turbulent (shear) stress, i.e., $-\rho_l \overline{v_i'' u_i''}$ (equation 2.40), the prediction results match with the experimental data for the considered volume void fractions ($\langle \bar{\alpha} \rangle \sim \mathcal{O}(10^{-2} \sim 10^{-1})$) and bulk liquid Reynolds number ($Re_D \sim \mathcal{O}(10^5)$) (figure 4.4). Both turbulence enhancement and suppression by bubbles are reasonably predicted. On the other hand, a convex profile at the intermediate-region ($0.05 \leq |xD| \leq 0.4$) in the experiments by Shawkat et al. (2008) is observed, which is not predicted by the present model. It is worth noting that, in other references, most of the $-\rho_l \overline{v_i'' u_i''}$ are concentrated near the wall-region ($x/D > 0.4$) where turbulence modification by the redistributed bubbles ($\nabla \bar{\alpha} \neq 0$) by the sidewalls, which is a manifest of reproducing $\partial \bar{v}_r / \partial x$ and $\partial \bar{\alpha} / \partial x$, is significant while they are negligible at the core-region with a flat-profile at $x/D \leq 0.4$. Furthermore, in own experience (Lee & Park 2020), when the mean liquid flow generated by a homogeneous bubble-swarm in quiescent water is deflected by a cylinder, the turbulent (shear) stress is then generated behind the cylinder along with $\partial \bar{v}_b / \partial x$ and $\partial \bar{\alpha} / \partial x$. However, in

the experiments by Shawkat et al. (2008), non-negligible magnitudes of $-\rho_l \overline{v_l'' u_l''}$ (a convex-profile) at the intermediate-region ($0.05 \leq |x/D| \leq 0.4$) where both $\partial \overline{v_r} / \partial x$ and $\partial \overline{\alpha} / \partial x$ already exhibit a flat-profile can be attributed to the aforementioned interactions between SIT and BIT in that specific configuration (e.g., $(D/2) / \langle \overline{d_b} \rangle \cong 33$ with $Re_D \sim \mathcal{O}(10^5)$). Our model (equation 2.40) cannot predict this kind of phenomena, which we admit is the absolute limitation of applicability. Actually, in this case, a more sophisticated higher-order prediction model other than the mixing-length theory such as the differential transport equation for the Reynolds stress (du Cluzeau et. al 2019; Ma et al. 2020) would be needed while implementing some limitations mentioned in the introduction.

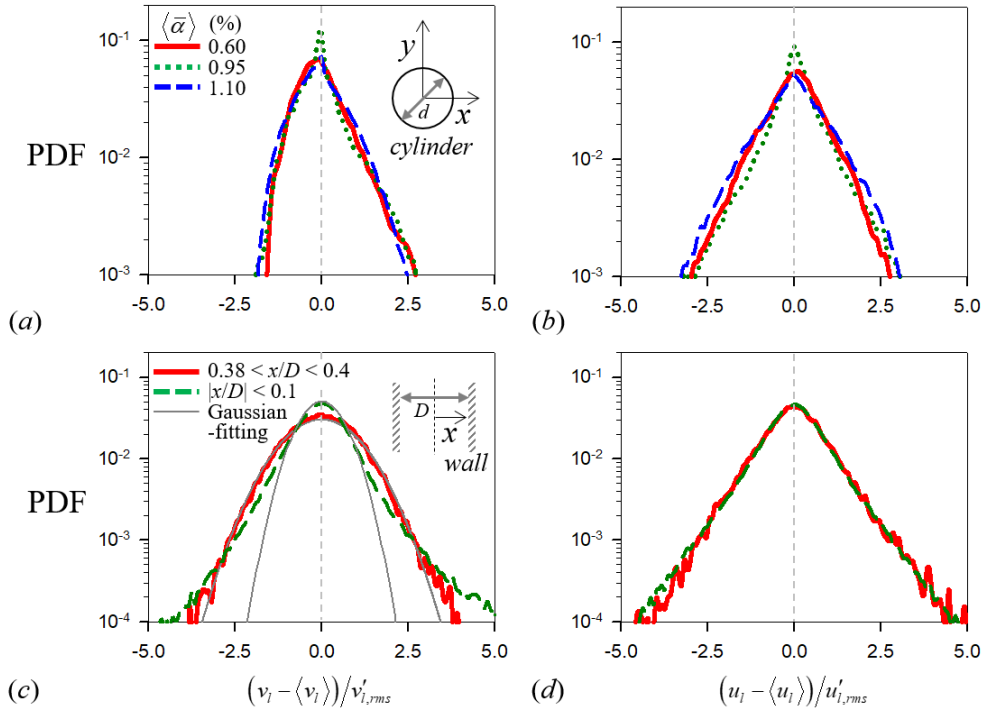


Figure 4.1. (a,b) Probability density functions (PDFs) of liquid velocity fluctuations in the wake behind a circular cylinder ($|x/d| < 0.5$, $0.5 < y/d < 3.0$) (Lee & Park 2020); (c,d) those in the core- ($|x/D| < 0.1$) and near wall-region ($0.38 < x/D < 0.4$) of turbulent bubbly pipe flows for $Re_D = 44,000$ (Lee et al. 2021), here a Gaussian-curve is drawn for comparison in streamwise direction: (a,c) streamwise-; (b,d) transverse-fluctuation in liquid-phase.

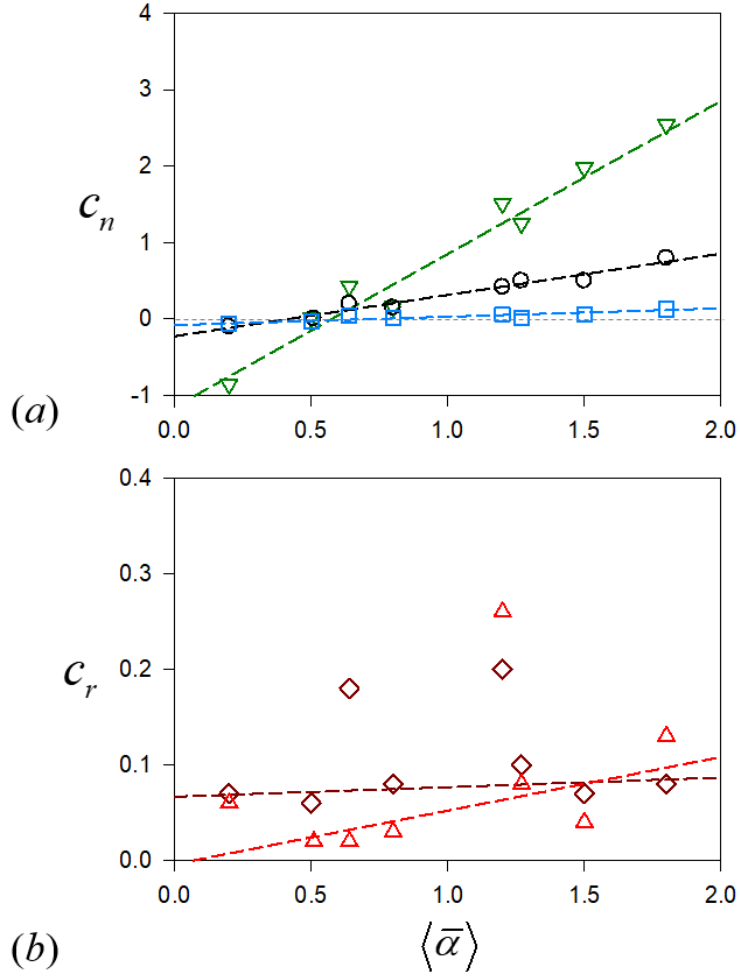


Figure 4.2. (a) Linear evolutions of tuning parameters in the predicted bubble-induced streamwise liquid fluctuation (v_l'') with increasing $\langle \bar{\alpha} \rangle$; (b) those in turbulent stress ($-\overline{v_l''u_l''}$); O, c_{1n} ; ∇ , c_{2n} ; \square , c_{3n} ; \triangle , c_{1r} ; \diamond , c_{2r} .

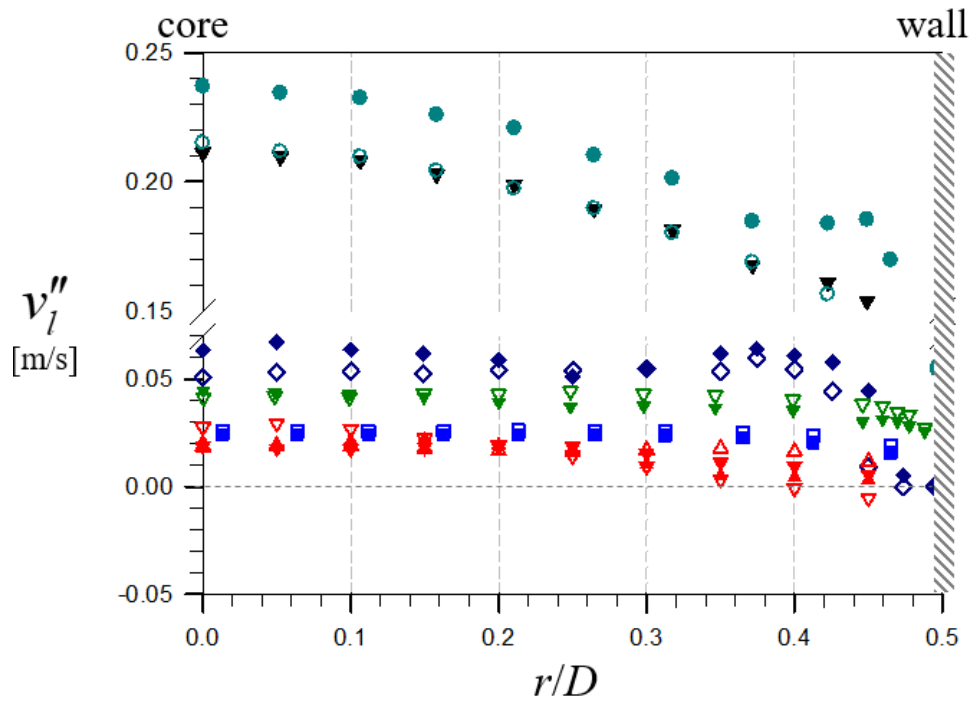


Figure 4.3. Comparison between the predicted (closed-) and measured (opened-symbol) bubble-induced streamwise liquid fluctuation. We exclusively selected the maximum volume void fraction case for each bulk Reynolds number (Re_D), except the works by Shawkat et al. (2008). The symbol is the same as specified in table 2.1 and \blacktriangledown denotes the prediction result in which the prefactors are optimized by the least-square method as an example.

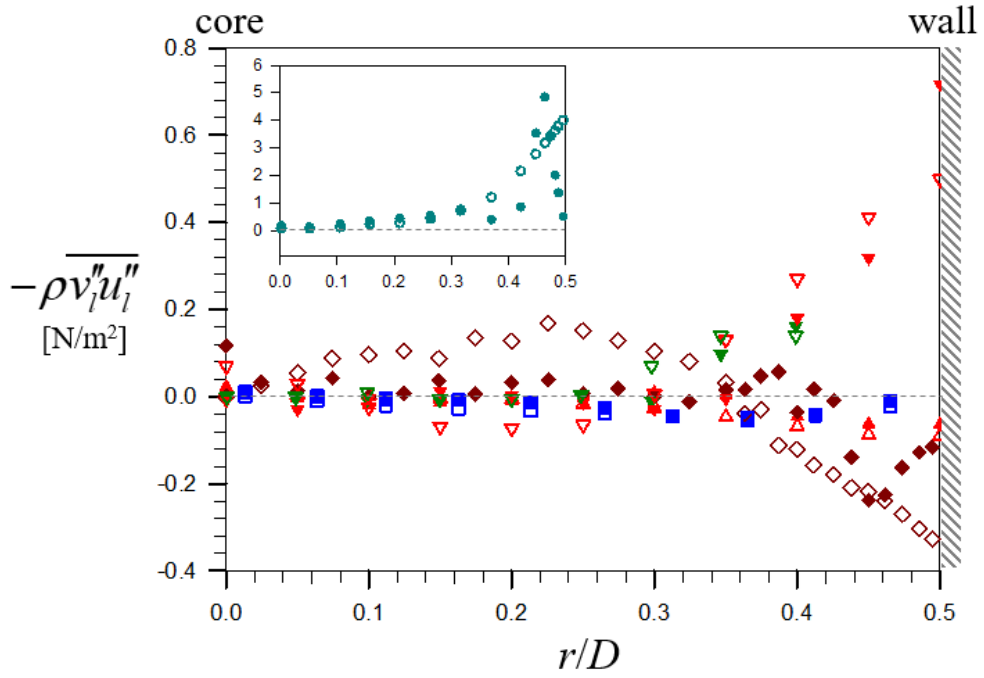


Figure 4.4. Comparison between the predicted (closed-) and measured (opened-symbol) bubble-induced turbulent (shear) stress. The description for each symbol is the same as in figure 4.3. Inset represents the data from Liu and Bankoff (1993) sharing the same axes titles and units.

Chapter 5.

Suggestion to the two-fluid Euler-Euler RANS simulation and following works

The lessons learned so far are finally applied here to the Euler-Euler (EE) RANS formulation to provide some insights and our next missions into the improvement of submodels and we ultimately contribute to reducing computation cost while reinforcing the accuracy. In the Reynolds-averaged Navier-Stokes equation in liquid-phase in the two-fluid EE-framework (equation 1.1), the interfacial momentum transfer (M_I) can be composed of relevant hydrodynamic forces depending on flow geometries on purposes (see section 3.3.4), and $M_I = -M_g$ if all the surface tension effects are neglected (du Cluzeau et al. 2020). As noted, the total (measured) Reynolds stress can be decomposed into two parts, simply one from the innate turbulence in the absence of bubbles, i.e., $\overline{u'_i u'_i}$, and the other from the bubble-induced turbulence, i.e., $\overline{u''_i u''_i}$, provided that mutual interactions are negligible, i.e., $\overline{u'_i u''_i} = 0$. For background turbulence in the absence of bubbles, one can use any approaches available in the classical single-phase theory like an eddy-viscosity hypothesis such as a zero-equation (e.g., mixing-length) or two-equation models (e.g., k - ε model, or another equivalent parameters like a characteristics frequency, ω). For example, if one uses the classical k - ε model to predict the background turbulence, the stress term in the momentum balance equation in liquid-phase is expressed as:

$$(1-\alpha) \frac{D}{Dt} \bar{u}_i = -(1-\alpha) \frac{1}{\rho_l} \frac{\partial \bar{p}}{\partial x_i} + (1-\alpha) \frac{\partial}{\partial x_j} \left[\left(\nu + c_\mu \frac{k^2}{\varepsilon} \right) \frac{\partial \bar{u}_i}{\partial x_j} - \overline{u''_i u''_j} \right], \quad (5.1)$$

Where both the transport equation for the turbulent kinetic energy (k) and the dissipation rate (ε) are identical to the single-phase equivalent without additional source terms (e.g., S_k and S_ε), and c_μ is 0.09. On the other hand, for the bubble-agitated turbulence, a total of six components of Reynolds stress should be closed via individual predictions based on an identical principle or a model-set. Utilizing

(and improving) the classical mixing-length theory as much as possible while additionally reflecting the complicated bubble wake's effects, we have developed a model for bubble-induced streamwise liquid fluctuation (equations 2.24 and 2.35) and turbulent (shear) stress (equations 2.29 and 2.40) respectively from the same root, which means that additional closure models for the remaining two-thirds (e.g., $\overline{u_i''u_i''}$, $\overline{w_i''w_i''}$, $\overline{u_i''w_i''} = \overline{w_i''u_i''}$, $\overline{v_i''w_i''} = \overline{w_i''v_i''}$) are needed to be developed (which would be our next missions) to practically utilize the results of this study in EE-RANS simulation. Nevertheless, in response to the community's desire to develop a full BIT model, we have done some of this, which is meaningful in that it gave good performance under various experiments studies available in the literature, of course, independent of our group.

The remaining closures can be accomplished in the following way. The modulation of the bubble-induced transverse liquid fluctuation ($\Delta u_i''$) by redistributed bubbles by a cylinder or sidewalls is closely related to

$$\Delta u_i'' \sim l_b \cdot \left| \frac{\partial \overline{u_i}}{\partial x} \right|, \quad (5.2)$$

then, the resultant liquid fluctuation in the transverse direction is

$$u_i'' \sim V_0 \langle \alpha \rangle^{0.4} + l_b \cdot \left| \frac{\partial \overline{u_i}}{\partial x} \right|, \quad (5.3)$$

analogous to the streamwise equivalent (v_i'') (equation 2.20) where l_b is the two-phase mixing-length (equations 2.6 and 2.12). The key here is to develop a $\overline{u_i}$ as in equations 2.14 and 2.17 that comprehensively reflects the bubble wake effects, which is tricky. On the other hand, the modeling of the shear stresses ($\overline{u_i''w_i''}$ and $\overline{v_i''w_i''}$) is rather straightforward, but, to the best of our knowledge, there are no prior experiments that provide the spatially-varying these quantities, which hinders us to check thorough validations. Excluding these difficulties, we have no obstacle in completing our mission.

Chapter 6.

Concluding remarks

In response to the community's desire to develop a full BIT model, new explicit algebraic turbulence models have been developed in the framework of the two-phase mixing-length theory in an unbounded homogeneous bubble-swarm past a circular cylinder in quiescent liquid and bounded laminar and turbulent bubbly flows for wide ranges of volume void fractions ($\mathcal{O}(10^{-2}-10^{-1})$) and bulk liquid Reynolds number ($Re_D \sim \mathcal{O}(10^5)$). These models could be expressed as a function of the mean liquid flow removing any references to the fluctuating part of the liquid velocity to overcome another closure problem encountered in the gas-liquid flow in the Euler-Euler Reynolds-averaged Navier-Stokes equation. Here, we attempt to analytically consider turbulence modification (e.g., enhancement or suppression) of the pure bubble-induced turbulence when it surrounded by external turbulence sources by the existence of a bluff body or sidewalls in confinements *via* a realistic bubbly mixing-length under the relevant configuration and an asymptotic scaling law for the mean liquid velocity under the influences of bubbles, all of which have been discussed thoroughly and validated independently. When the developed submodels are used together, it yields to an explicit algebraic model for the bubble-induced liquid fluctuation (equivalent to the square-root of the streamwise normal stress) and turbulent stress, respectively. The detailed procedures to derive the proposed models and the theoretical reasoning for them are also provided, all of which are consistent with the previous observations (e.g., PDFs of the liquid fluctuations). To independently validate the proposed models, we have configured the homogeneous bubble-swarm and let it flow over a circular cylinder at downstream to artificially generate turbulence modulation of the upstream characteristics of the bubble-induced turbulence while varying the volume void fraction in a small-to-moderate range and cylinder diameter. The Reynolds number of rising bubbles is approximately 10^3 . We focused on how the preferred concentration of bubbles past a cylinder is established and how its wake is induced. We measured the gas- and liquid-phase velocity fields simultaneously

by using a high-speed two-phase particle image velocimetry technique. Depending on the void distribution in the wake region, two regimes are classified. In the first regime (smaller $\langle \bar{\alpha} \rangle$), the bubbles tend to accumulate downstream of the side of the cylinder (along the shear-layer region), which is attributed to the mitigated lateral migration of bubbles via the balance between the drag force with the pressure gradient and shear-induced lift forces acting on them. As $\langle \bar{\alpha} \rangle$ increases, in the second regime, the shear-induced lift force becomes sufficient enough to move the bubbles toward the center of the cylinder, resulting in the local void fraction, exhibiting a broad peak at this position. Based on the void distribution, the liquid flow forms an interesting wake structure behind the cylinder. For example, a wake-defect-like streamwise velocity profile and skew-symmetric turbulent stress are induced; however, the distortion by the circular cylinder is restored quite fast (within $5D$ along the streamwise direction). Increasing the cylinder size, however, delays the recovery of uniform flow statistics and reduces the turbulence level in the wake. Based on the observed physics, the proposed models, which is an extension of the classical eddy-diffusivity hypothesis, but additionally considers the effects of bubble-induced flow and multiple bubbles, are in a reasonably good agreement with the experimental data measured at downstream of the circular cylinder. Especially, the absolute magnitudes and the tendencies of the bubble-induced turbulence are reasonably predicted at both inside and outside of the cylinder by the proposed models, and we have also discussed the evolutions of each prefactor along downstream, and reasoning for them is also provided. We have expanded the validation tests to other bubbly flows (e.g., wall-bounded upward laminar and turbulent bubbly flows) by gathering all the available pieces of experimental data available in the literature. We have confirmed that the absolute magnitudes and the tendencies of the bubble-induced turbulence when surrounded by incidence turbulence are reasonably predicted at both the core- and near wall-region of pipes (channels) by the proposed models, and we have also discussed some abnormal discrepancies and their putative origination. Comparisons of the developed models with other experiments are highly desirable, but to the best of our knowledge, there are no more published works that provide the spatially-varying experimental data. We try not to hide our limitations of future applicability,

but rather objectively evaluate the strength and weakness of the proposed models. Lastly, a short guideline for a large-scale Reynolds-averaged Navier-Stokes simulation in a two-fluid Euler-Euler framework is provided and our next plan for constructing a full-set explicit Reynolds stress tensor is presented, and of course, concrete alternatives to achieve the goal are discussed together. The simplicity and robustness of these purely algebraic models make them very attractive for utilizing in many engineering problems to efficiently predict the turbulent nature of the various bubbly configurations with lower cost and we expect them to be useful in the development of future BIT models.

Bibliography

- ADOUA, S. R., LEGENDRE, D. & MAGNAUDET, J. 2009 Reversal of the lift force on an oblate bubble in a weakly viscous linear shear flow. *J. Fluid Mech.* **628**, 23–41.
- ADRIAN, R. J. & WESTERWEEL, J. 2011 *Particle image velocimetry*. Cambridge University Press.
- ALMÉRAS, E., MATHAI, V., LOHSE, D. & SUN, C. 2017 Experimental investigation of the turbulence induced by a bubble swarm rising within incident turbulence. *J. Fluid Mech.* **825**, 1091–1112.
- AMOURA, Z., BESNACI, C. & RISSO, F. 2017 Velocity fluctuations generated by the flow through a random array of spheres: a model of bubble-induced agitation. *J. Fluid Mech.* **823**, 592–616.
- ANTAL, S. P., LAHEY, JR. R. T. & FLAHERTY, J. E. 1991 Analysis of phase distribution in fully developed laminar bubbly two-phase flow. *Int. J. Multiph. Flow* **17**, 635–652.
- BATCHELOR, G. K. 1967 *An Introduction to Fluid Dynamics*. Cambridge University Press.
- DE BERTODANO, M. A. L. 1998 Two fluid model for two-phase turbulent jets. *Nucl. Eng. Des.* **179**, 65–74.
- DE BERTODANO, M. L., LAHEY JR, R. T. & JONES, O. C. 1994 Turbulent bubbly two-phase flow data in a triangular duct. *Nucl. Eng. Des.* **146**, 43–52.
- BRÖDER, D. & SOMMERFELD, M. 2007 Planar shadow image velocimetry for the analysis of the hydrodynamics in bubbly flows. *Meas. Sci. Technol.* **18**, 2513–2528.
- BURNS, A. D., FRANK, T., HAMILL, I. & SHI, J. M. 2004 The Favre averaged drag model for turbulent dispersion in Eulerian multi-phase flows. *In 5th International Conference on Multiphase Flow*.
- CAO, Y., TAMURA, T. & KAWAI, H. 2020 Spanwise resolution requirements for the simulation of high-Reynolds-number flows past a square cylinder. *Comput. Fluids* **196**, 104320.
- CASTAING, B., GAGNE, Y. & HOPFINGER, E. J. 1990 Velocity probability

- density functions of high Reynolds number turbulence. *Physica D* **46**, 177–200.
- CHAHED, J., ROID, V. & MASBERNAT, L. 2003 Eulerian-Eulerian two-fluid model for turbulent gas-liquid bubbly flows. *Int. J. Multiph. Flow* **29**, 23–49.
- CLIFT, R., GRACE, J. R. & WEBER, M. E. 1978 *Bubbles, Drops and Particles*. New York: Academic Press.
- DU CLUZEAU, A., BOIS, G. & TOUTANT, A. 2019 Analysis and modelling of Reynolds stresses in turbulent bubbly up-flows from direct numerical simulations. *J. Fluid Mech.* **866**, 132–168.
- DU CLUZEAU, A., BOIS, G., TOUTANT, A. & MARTINEZ, J. M. 2020 On bubble forces in turbulent channel flows from direct numerical simulations. *J. Fluid Mech.* **882**, A27.
- COLOMBET, D., LEGENDRE, D., COCKX, A. & GUIRAUD, P. 2015 Dynamics and mass transfer of rising bubbles in a homogenous swarm at large gas volume fraction. *J. Fluid Mech.* **763**, 254–285.
- COLOMBET, D., LEGENDRE, D., COCKX, A., GUIRAUD, P., RISSO, F., DANIEL, C. & GALINAT, S. 2011 Experimental study of mass transfer in a dense bubble swarm. *Chem. Eng. Sci.* **66**, 3432–3440.
- DREW, D. & LAHEY JR., R. T. 1987 The virtual mass and lift forces on a sphere in a rotating and straining flow. *Int. J. Multiph. Flow* **13**, 113–121.
- ELLINGSEN, K. & RISSO, F. 2001 On the rise of an ellipsoidal bubble in water: oscillatory paths and liquid-induced velocity. *J. Fluid Mech.* **440**, 235–268.
- ERN, P., RISSO, F., FABRE, D. & MAGNAUDET, J. 2012 Wake-induced oscillatory paths of bodies freely rising or falling in fluids. *Annu. Rev. Fluid Mech.* **44**, 97–121.
- GARNIER, C., LANCE, M. & MARIÉ, J. L. 2002 Measurement of local flow characteristics in buoyancy-driven bubbly flow at high void fraction. *Exp. Therm. Fluid Sci.* **26**, 811–815.
- GONZALEZ, R. C., WOODS, R. E. & EDDINS, S. L. 2011 *Digital image processing using MATLAB, 2nd edn*. McGraw-Hill Education.
- HIBIKI, T. & ISHII, M. 2007 Lift force in bubbly flow systems. *Chem. Eng. Sci.* **62**, 6457–6474.

- HOSOKAWA, S. & TOMIYAMA, A. 2009 Multi-fluid simulation of turbulent bubbly pipe flows. *Chem. Eng. Sci.* **64**, 5308–5318.
- HOSOKAWA, S. & TOMIYAMA, A. 2013 Bubble-induced pseudo turbulence in laminar pipe flows. *Int. J. Heat Fluid Flow* **40**, 97–105.
- ISHII, M. & ZUBER, N. 1979 Drag coefficient and relative velocity in bubbly, droplet or particulate flows. *AIChE J.* **25**, 843–855.
- JEONG, H. & PARK, H. 2015 Near-wall rising behaviour of a deformable bubble at high Reynolds number. *J. Fluid Mech.* **771**, 564–594.
- JOHNSON, T. A. & PATEL, V. C. 1999 Flow past a sphere up to a Reynolds number of 300. *J. Fluid Mech.* **378**, 19–70.
- JOO, Y. & DHIR, V. K. 1994 An experimental study of drag on a single tube and on a tube in an array under two-phase cross flow. *Int. J. Multiph. Flow* **20**, 1009–1019.
- KATAOKA, I., BESNARD, D. C. & SERIZAWA, A. 1992 Basic equation of turbulence and modeling of interfacial transfer terms in gas-liquid two-phase flow. *Chem. Eng. Commun.* **118**, 221–236.
- KATAOKA, I., SERIZAWA, A. & BESNARD, D. C. 1993 Prediction of turbulence suppression and turbulence modeling in bubbly two-phase flow. *Nucl. Eng. Des.* **141**, 145–158.
- KIM, M., LEE, J. H. & PARK, H. 2016 Study of bubble-induced turbulence in upward laminar bubbly pipe flows measured with a two-phase particle image velocimetry. *Exp. Fluids* **57**, 55.
- KIM, N., KIM, H. & PARK, H. 2015 An experimental study on the effects of rough hydrophobic surfaces on the flow around a circular cylinder. *Phys. Fluids* **27**, 085113.
- KIM, Y. & PARK, H. 2019 Upward bubbly flows in a square pipe with a sudden expansion: Bubble dispersion and reattachment length. *Int. J. Multiph. Flow* **118**, 254–269.
- LAHEY JR., R. T., LOPEX DE BERTODANO, M. & JONES JR., O. C. 1993 Phase distribution in complex geometry conduits. *Nucl. Eng. Des.* **141**, 177–201.
- LAI, C. C. & SOCOLOFSKY, S. A. 2019 The turbulent kinetic energy budget in a

- bubble plume. *J. Fluid Mech.* **865**, 993–1041.
- LANCE, M. & BATAILLE, J. 1991 Turbulence in the liquid phase of a uniform bubbly air-water flow. *J. Fluid Mech.* **222**, 95–118.
- LAU, Y. M., DEEN, N. G. & KUIPERS, J. A. M. 2013 Development of an image measurement technique for size distribution in dense bubbly flows. *Chem. Eng. Sci.* **94**, 20–29.
- LAWSON, N. J., RUDMAN, M., GUERRA, A. & LOIW, J.-L. 1999 Experimental and numerical comparisons of the break-up of a large bubble. *Exp. Fluids* **26**, 524–534.
- LEE, J. & PARK, H. 2017 Wake structures behind an oscillating bubble rising close to a vertical wall. *Int. J. Multiph. Flow* **91**, 225–242.
- LEE, J. & PARK, H. 2020 Bubble dynamics and bubble-induced agitation in the homogeneous bubble-swarm past a circular cylinder at small to moderate void fractions. *Phys. Rev. Fluids* **5**, 054304.
- LEE, J. H., KIM, H., LEE, J. & PARK, H. 2021 Scale-wise analysis of upward turbulent bubbly flows: an experimental study. *Phys. Fluids*, under review.
- LIAO, Y., MA, T., LIU, L., ZIEGENHEIN, T., KREPPER, E. & LUCAS, D. 2018 Eulerian modelling of turbulent bubbly flow based on a baseline closure concept. *Nucl. Eng. Des.* **337**, 450–459.
- LINDKEN, R. & MERZKIRCH, W. 2002 A novel PIV technique for measurements in multiphase flows and its application to two-phase bubbly flows. *Exp. Fluids* **33**, 814–825.
- LIU, K., DENG, J. & MEI, M. 2016 Experimental study on the confined flow over a circular cylinder with a splitter plate. *Flow Meas. Instrum.* **51**, 95–104.
- LIU, T. J. & BANKOFF, S. G. 1993 Structure of air-water bubbly flow in a vertical pipe - I. Liquid mean velocity and turbulence measurements. *Int. J. Heat Mass Transf.* **36**, 1049–1060.
- LU, J. & TRYGVASON, G. 2013 Dynamics of nearly spherical bubbles in a turbulent channel upflow. *J. Fluid Mech.* **732**, 166–189.
- MA, T., LUCAS, D. & BRAGG, A. D. 2020 Explicit algebraic relation for calculating Reynolds normal stresses in flows dominated by bubble-induced turbulence. *Phys. Rev. Fluids* **5**, 084305.

- MA, T., LUCAS, D., JAKIRLIĆ, S. & FRÖHLICH, J. 2020 Progress in the second-moment closure for bubbly flow based on direct numerical simulation data. *J. Fluid Mech.* **883**, A9.
- MA, T., SANTARELLI, C., ZIEGENHEIN, T., LUCAS, D. & FRÖHLICH, J. 2017 Direct numerical simulation-based Reynolds-averaged closure for bubble-induced turbulence. *Phys. Rev. Fluids* **2**, 034301.
- MAGNAUDET, J. & EAMES, I. 2000 The motion of high-Reynolds-number bubbles in inhomogeneous flows. *Annu. Rev. Fluid Mech.* **32**, 659–708.
- MARIÉ, J. L., MOURSALI, E. & TRAN-CONG, S. 1997 Similarity law and turbulence intensity profiles in a bubbly boundary layer at low void fractions. *Int. J. Multiph. Flow* **23**, 227–247.
- MARTINEZ-MERCADO, J., PALACIOS-MORALES, C. A. & ZENIT, R. 2007 Measurement of pseudoturbulence intensity in monodispersed bubbly liquids for $10 < \text{Re} < 500$. *Phys. Fluids* **19**, 103302.
- MILNE-THOMSON, L. M. 1996 *Theoretical hydrodynamics*. London: Macmillan.
- MOUGIN, G. & MAGNAUDET, J. 2006 Wake-induced forces and torques on a zigzagging/spiralling bubble. *J. Fluid Mech.* **567**, 185–194.
- NAKORYAKOV, V. E., KASHINSKY, O. N., BURDUKOV, A. P. & ODNORAL, V. P. 1981 Local characteristics of upward gas-liquid flows. *Int. J. Multiph. Flow* **7**, 63–81.
- NIGMATULIN, R. I. 1979 Spatial averaging in the mechanics of heterogeneous and dispersed systems. *Int. J. Multiph. Flow* **5**, 353–385.
- OTSU, N. 1979 A threshold selection method from gray-level histograms. *IEEE Trans. Syst. Man. Cybern.* **9**, 62–66.
- OZGOREN, M., PINAR, E., SAHIN, B. & AKILLI, H. 2011 Comparison of flow structures in the downstream region of a cylinder and sphere. *Int. J. Heat Fluid Flow* **32**, 1138–1146.
- PANG, M. & WEI, J. 2013 Experimental investigation on the turbulence channel flow laden with small bubbles by PIV. *Chem. Eng. Sci.* **94**, 302–315.
- PARNAUDEAU, P., CARLIER, J., HEITZ, D. & LAMBALLAIS, E. 2008 Experimental and numerical studies of the flow over a circular cylinder at Reynolds number 3900. *Phys. Fluids* **20**, 085101.

- PRAKASH, V. N., MERCADO, J.M., VAN WIJNGAARDEN, L., MANCILLA, E., TAGAWA, Y., LOHSE, D. & SUN, C. 2016 Energy spectra in turbulent bubbly flows. *J. Fluid Mech.* **791**, 174–190.
- REEKS, M. W. & MCKEE, S. 1984 The dispersive effects of Basset history forces on particle motion in a turbulent flow. *Phys. Fluids*, **27**, 1573–1582.
- RENSSEN, J., LUTHER, S. & LOHSE, D. 2005 The effect of bubbles on developed turbulence. *J. Fluid Mech.* **538**, 153–187.
- RIBOUX, G. & LEGENDRE, D. & RISSO, F. 2013 A model of bubble-induced turbulence based on large-scale wake interactions. *J. Fluid Mech.* **719**, 362–387.
- RIBOUX, G., RISSO, F. & LEGENDRE, D. 2010 Experimental characterization of the agitation generated by bubbles rising at high Reynolds number. *J. Fluid Mech.* **643**, 509–539.
- RISSO, F. 2016 Physical interpretation of probability density functions of bubble-induced agitation. *J. Fluid Mech.* **809**, 240–263.
- RISSO, F. 2018 Agitation, mixing, and transfers induced by bubbles. *Annu. Rev. Fluid Mech.* **50**, 25–48.
- RISSO, F. & ELLINGSEN, K. 2002 Velocity fluctuations in a homogeneous dilute dispersion of high-Reynolds-number rising bubbles. *J. Fluid Mech.* **453**, 395–410.
- ROIG, V. & DE TOURNEMINE, A. L. 2007 Measurement of interstitial velocity of homogeneous bubbly flows at low to moderate void fraction. *J. Fluid Mech.* **572**, 87–110.
- SANTARELLI, C. & FRÖHLICH, J. 2016 Direct numerical simulations of spherical bubbles in vertical turbulent channel flow. Influence of bubble size and bidispersity. *Int. J. Multiph. Flow* **81**, 27–45.
- SATHE, M. J., THAKER, I. H., STRAND, T. E. & JOSHI, J. B. 2010 Advanced PIV/LIF and shadowgraphy system to visualize flow structure in two phase bubbly flows. *Chem. Eng. Sci.* **65**, 2431–2442.
- SATO, Y. & SEKOGUCHI, K. 1975 Liquid velocity distribution in two-phase bubble flow. *Int. J. Multiph. Flow* **2**, 79–95.
- SERIZAWA, A. & KATAOKA, I. 1990 Turbulence suppression in bubbly two-

- phase flow. *Nucl. Eng. Des.* **122**, 1–16.
- SHAWKAT, M. E., CHING, C. Y. & SHOUKRI, M. 2008 Bubble and liquid turbulence characteristics of bubbly flow in a large diameter vertical pipe. *Int. J. Multiph. Flow* **34**, 767–785.
- SIMIANO, M., LAKEHAL, D., LANCE, M. & YADIGAROGLU, G. 2009 Turbulent transport mechanisms in oscillating bubble plumes. *J. Fluid Mech.* **633**, 191–231.
- SUGIYAMA, K., TAKAGI, S. & MATSUMOTO, Y. 2001 Three-dimensional numerical analysis of bubbly flow around a circular cylinder. *JSME Int. J. Ser. B Fluids Therm. Eng.* **44**, 319–327.
- TAKAGI, S. & MATSUMOTO, Y. 2010 Surfactant effects on bubble motion and bubbly flows. *Annu. Rev. Fluid Mech.* **43**, 615–636.
- TROSHKO, A. A. & HASSAN, Y. A. 2001 A two-equation turbulence model of turbulent bubbly flows. *Int. J. Multiph. Flow* **27**, 1965–2000.
- WEST, G. S. & APELT, C. J. 1982 The effects of tunnel blockage and aspect ratio on the mean flow past a circular cylinder with Reynolds numbers between 10^4 and 10^5 . *J. Fluid Mech.* **114**, 361–377.
- ZENIT, R., KOCH, D. L. & SANGANI, A. S. 2001 Measurements of the average properties of a suspension of bubbles rising in a vertical channel. *J. Fluid Mech.* **429**, 307–342.
- ZENIT, R. & MAGNAUDET, J. 2008 Path instability of rising spheroidal air bubbles: a shape-controlled process. *Phys. Fluids* **20**, 061702.
- ZIEGENHEIN, T., RZEHAKE, R., MA, T. & LUCAS, D. 2017 Towards a unified approach for modelling uniform and non-uniform bubbly flows. *Can. J. Chem. Eng.* **95**, 170–179.

기포 유도 난류응력 모델 개발 및 원형 실린더 주위를 흐르는 균일한 기포스웜에서 실험적 검증

서울대학교 대학원
기계항공공학부
이주범(LEE JUBEOM)

요약

지금까지 기포 유도 난류응력 모델을 개발하기 위한 많은 선행 연구들이 있었지만, 같은 원리를 바탕으로 한번에 두 가지 성분 이상의 난류응력 모델들을 개발한 연구는 없었다. 본 연구에서는 기체-액체 2상유동 내 새로운 혼합길이 체계를 기저로 한 명시적 대수 모델들을 개발하였고, 이를 초기 정지한 액체 내 상승하는 bubble swarm이 원형 실린더 주위를 흐르는 유동에 적용하였다. 또한 본 연구에서 개발된 난류응력 모델들을 넓은 체적기포분율 및 배경 액상 레이놀즈 수 범위를 갖는 관내 층류 및 난류 기포류유동에서 대해 확장 적용하였다. 개발된 모델들은 액체상의 시간평균된 1차 통계량으로만 표현되며, 2상유동 내 필연적으로 발생하는 closure problem을 극복하기 위해 액체 섭동 속도에 대한 참조를 두지 않는다. 여기서, 각 유동 환경에 부합되는 사실적인 기포류 혼합 길이를 바탕으로, 순수 기포 유도 난류가 잠긴 물체 또는 벽면 경계조건에 의해 추가적으로 변화되는 난류도 증가 (또는 감소) 경향을 예측한다. 뿐만 아니라 오직 기포 통계량만으로 구성된 평균 액체 속도에 대한 스케일링 법칙을 제안하여, 이에 대한 상세한 토론 및 독립적인 검증을 진행한다. 개발된 하위 모델들을 모두 종합하면, 기포가 유발시킨 주 유동방향 액체 섭동 속도 및 레이놀즈 전단 응력에 대한 명시적 대수 모델들이 각각 도출된다. 보다 상세한 유도 과정 및 각 과정에서 적절한 이론적 뒷받침 또한 제시되었으며, 이는 과거 실험 연구 결과와 일치한다 (예: 각 방향 액체 섭동에 대한 확률 밀도 함수 분포 및 액체 난류

강도와 체적기포분율 간 상관관계). 개발된 모델들의 예측 성능을 독립적으로 비교하기 위해, 우리는 초기 정지한 액체 내 상승하는 균질 bubble-swarm을 조성하였고, 이것을 원형실린더 주위에 흐르게 하여 인위적인 난류도 변화를 발생시켰다. 또한 입구에서 주입되는 체적기포분율 범위와 실린더 직경을 가변시켜 실험을 반복하였다. 이때 기포의 레이놀즈 수는 약 10^3 이다. 먼저 실험 결과를 설명하면, 우리는 기포들이 실린더 주위를 지나며 발생시키는 우위농도(preferential concentration) 및 이것이 실린더 후류에 어떤 영향을 미치는지에 대한 정량 연구를 초고속 2상 입자영상속도계(particle-image velocimetry) 기법을 이용하여 실험적으로 분석하였다. 입구에서 체적기포분율이 증가함에 따라 하류에서 기포 분포 및 그에 따른 기포 통계량 분포는 서로 전혀 다른 두 가지 대표 영역(regime)을 나타낸다. 우리는 이러한 차이를 발생시키는 원인을 규명하기 위해 각 상(phase)의 경계에 작용하는 적절한 수력학 힘들을 선정하 뒤, 이들 간 상대 비교를 통해 기포 거동 메커니즘을 설명하였다. 한편, 실린더 후류 내 기포 거동에 따라 서로 상이한 액체 유동이 발달되는데, 예를 들어 기포류유동에서도 기존 단상유동과 유사한 평균 액체 속도 분포 및 원점대칭인 레이놀즈 전단 응력이 발달되지만, 이러한 실린더에 의한 교란은 하류에서 더 빨리 회복된다는 특징이 있다(하류를 따라 실린더 직경의 5배 길이 이내). 그러나, 실린더 직경을 키우게 되면(또는 기포크기가 줄어들면) 각 상의 통계량들이 상류 값들로 회복되기까지 더 오랜 시간이 걸릴 뿐만 아니라, 액상 난류 강도 또한 줄어든다. 또한 우리는 이러한 원인을 설명한다. 이렇게 실험적으로 관찰된 물리 현상들이, 기존 단상유동 내 와점성(eddy-viscosity) 가설을 확장하고, 기포 후류 효과까지 추가적으로 반영한 난류응력 모델들로 잘 예측되는지 검증하였다. 그 결과, 기포 유도 난류응력의 크기 및 공간 상 분포가 실린더 안팎에서 모두 잘 예측되었다, 또한 하류를 따라 각 모델 내 포함된 계수(prefactor)들의 변화에 대한 정석, 정량적 토의도 진행하였다. 나아가 우리는 개발된 모델들을 보다 일반적인 기포류유동(관 내 층류 및 난류

기포류유동)에 대해 확장 검토하기 위해, 가용 가능한 선행 실험 연구들을 모두 찾아 일괄적으로 적용해 보았다. 그 결과, 시스템 내 기포 유도 난류뿐만 아니라 추가적인 외부 난류 소스가 공존하는 상황에서도 관 내 중심 및 벽면 근처에서 모두 난류 통계량의 절대값, 국소 최대 (최소)값 위치, 그리고 공간상 분포들이 모두 합리적으로 예측되었다. 한편 개발된 모델 예측 값과 실험데이터 간 큰 차이를 보이는 실험결과에 대해 합리적 원인을 추론하였고, 본 연구에서 개발된 모델들이 갖는 강점과 약점을 객관적으로 평가하였다. 본 연구에서는 기체-액체 2상유동 내 새로운 혼합길이 체계 및 액체 속도에 대한 스케일링 법칙들을 바탕으로, 한번에 두 가지 이상 성분의 레이놀즈 응력 모델들을 최초로 제시하였고, 개발된 모델들은 넓은 체적기포분율 및 배경 액상 레이놀즈 범위에서, 관 내 중심 및 벽면 근처 영역에서 모두 정확한 예측 성능을 보였다. 또한 기포 유도 레이놀즈 응력을 예측하기 위해서는 기존 액체 속도 구배뿐만 아니라, 기포의 상대 속도 및 국소 기포분율 구배 또한 중요한 인자임을 밝혀냈다. 그 결과, 순수 기포 유도 난류가 잠긴 물체 또는 벽면 경계조건에 의해 추가적으로 변화되는 난류도 증가 (또는 감소) 경향을 동시에 예측 할 수 있었는데, 이는 유관 분야에서 가장 우수한 성능을 보였다.

주요어 : 기포류유동, 원형 실린더, 단힘문제, 기포유도 난류, 난류 모델링, 실험 검증

학번 : 2014-22500